LAWRENCE
LIVERMORE
NATIONAL
LABORATORY

UCRL-PROC-227349

Collaborations in Nuclear Reactors

E. Bringa, A. Caro, N. Barton, J. Marian, V. Bulatov, T. Arsenlis

January 1, 2007

Collaborations in Nuclear Reactors
Livermore, CA United States
December 5, 2006 through December 5, 2006

This work was performed under the auspices of the U.S. Department of Energy by University of California, Lawrence Livermore National Laboratory under Contract W-7405-Eng-48.

Atomistic simulations of radiation damage: from eV to GeV

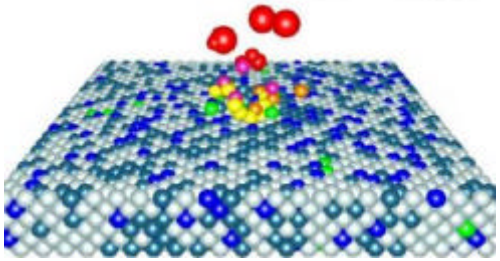

E.M. Bringa
(ebringa@llnl.gov)

December 2006

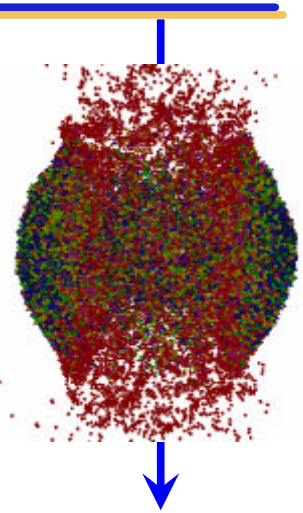

Outline:

1- eV ion bombardment: tokamak erosion

2- keV ion bombardment: bombardment of nanocrystals

3- MeV-GeV ion bombardment: track models & amorphization of complex materials.

Collaborators:

S. Bajt, J. Bradley, A. Caro, Z. Dai, G. Gilmer, G. Graham, S. Kucheyev, T. Felter, J. Marian, W. van Breugel, M. Victoria, L. Zepeda-Ruiz (LLNL), C. Dukes, R.E. Johnson, M. Loeffler, R. Baragiola (UVA), P. Durham (Cincinnati), L. Davila (UC Davis), R. Devanathan, R. Corrales (PNNL), A. Tielens (NASA Ames), D. Schwen, H. Hofsass (Göttingen)

This work was performed under the auspices of the U.S. Department of Energy and Lawrence Livermore National Laboratory under contract No. W-7405-Eng-48, with support from the laboratory directed research and development program and CMS/MSTD

Sputtering of hydrocarbons (eV)
Motivation: need to understand ITER divertor erosion

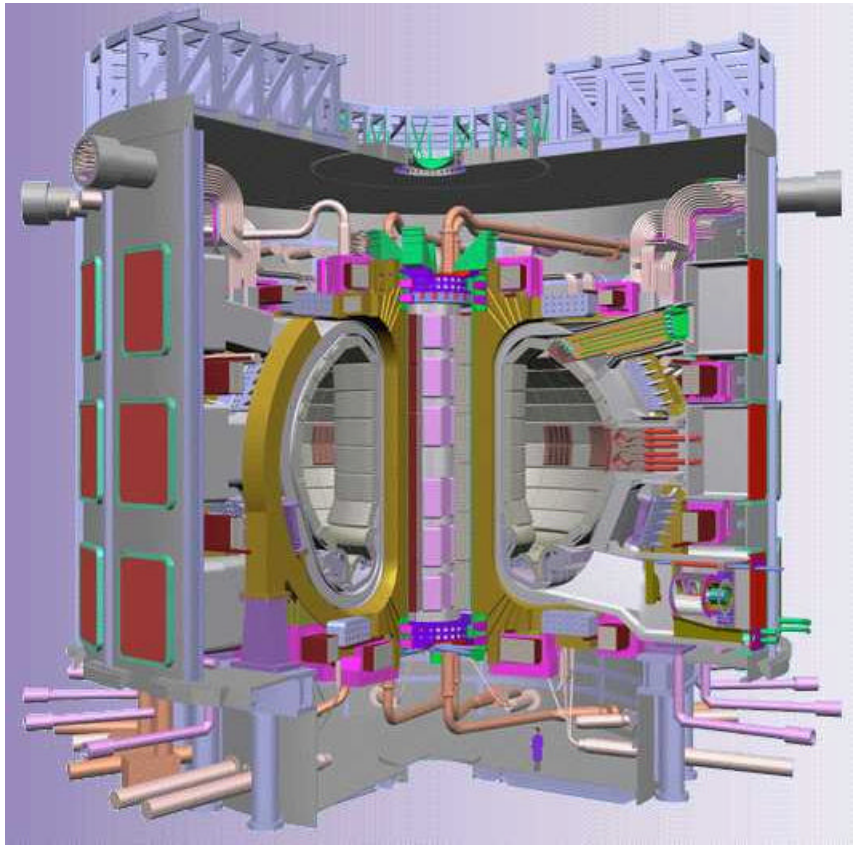

Radiation damage in wall material also important (charla de Max Victoria)

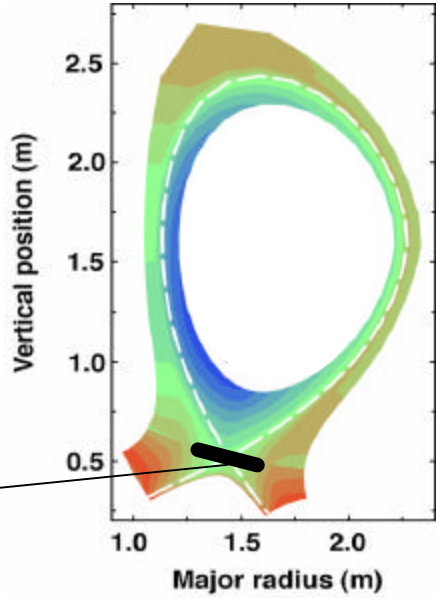

Divertor plate

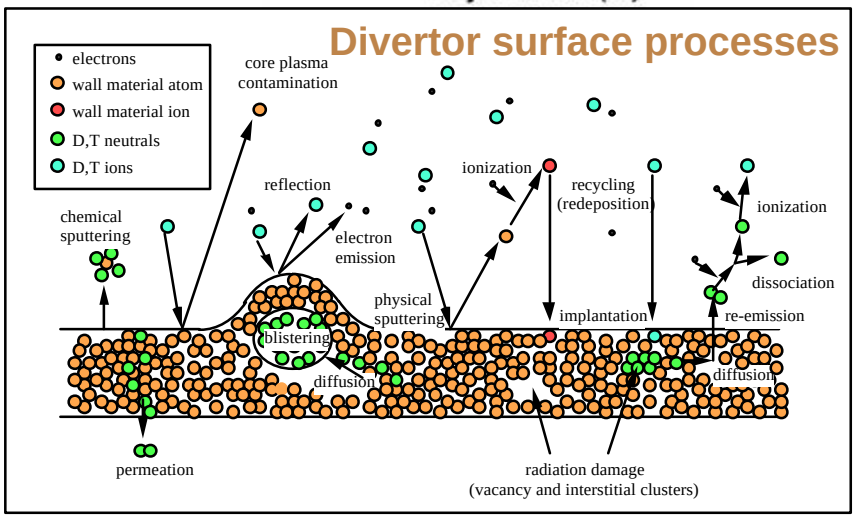

Sputtering MD simulations
AIREBO & REBO (Brenner) inter-atomic reactive potentials

AIREBO (Adaptive Intermolecular Reactive Empirical Bond Order) potential is an extension of REBO that includes:

- Short-range, bonding interactions from Brenner (<3 Å)
- Long-range, non-bonding interactions (<6 Å)
- Torsional interactions (4-body) 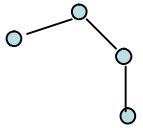

Sputtered-particle trajectories (solid colors) just above the surface

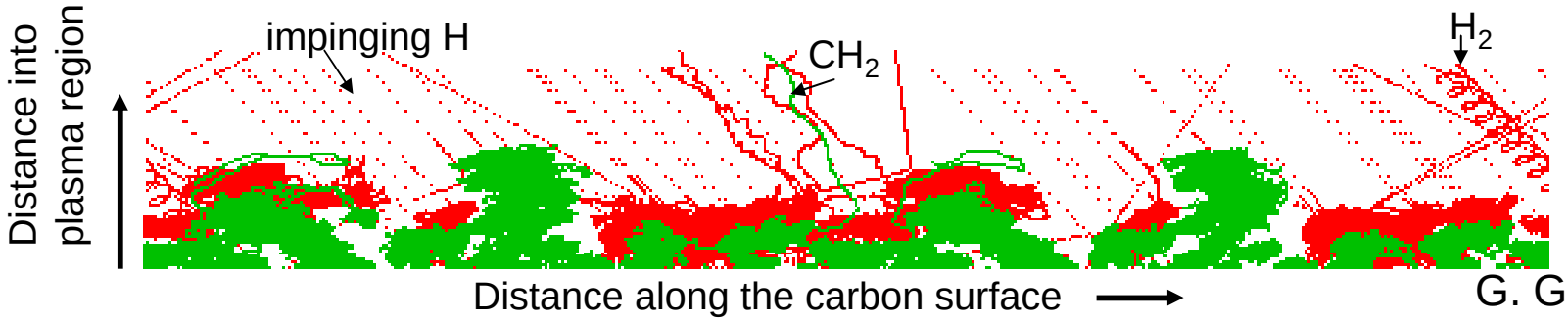

G. Gilmer

Conditions: T_{surf} = 300-600K, E_i = 2-200 eV, ?$_i$ =0-65^o

Need 1000-3000 events

Carbon sputtering yield as a function of energy
First sputtering rates using the AIREBO potential

Marian *et al*, Physica Scripta (2006)

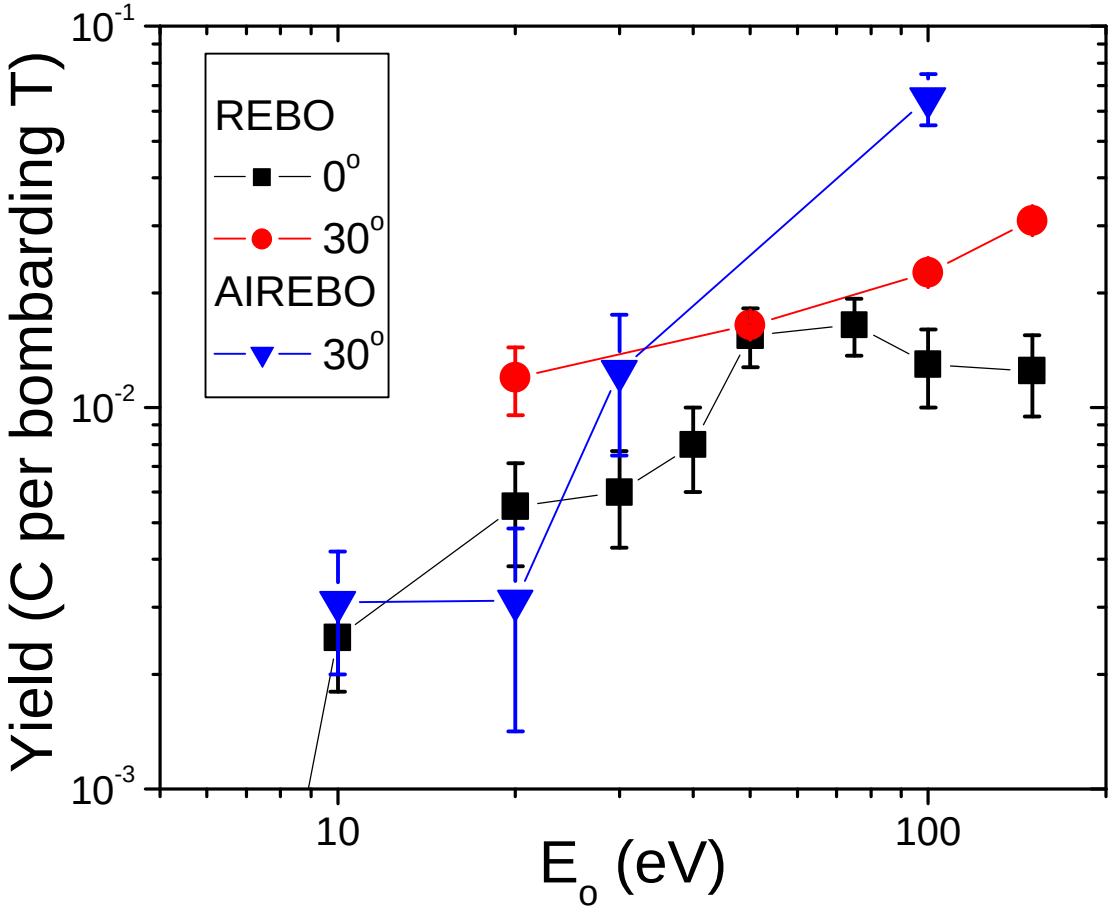

REBO and AIREBO yields are the same within a factor of 2-4.

Runs with bigger/different samples in progress

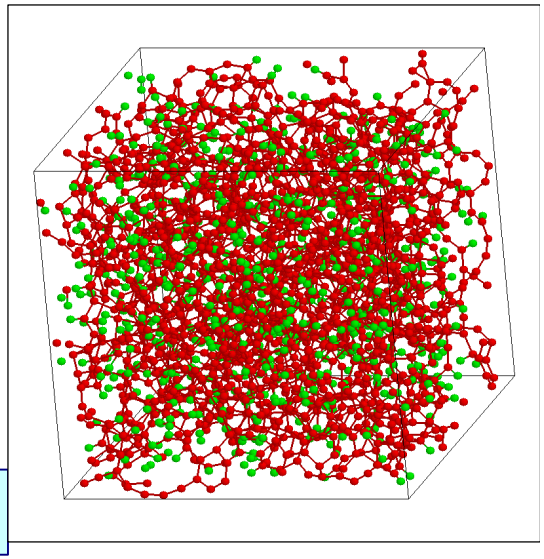

In progress: Calculations including ReaxFF (CalTech)

keV bombardment of nanocrystals
Can we design of improved radiation-resistant materials?

Nanocrystalline materials have useful mechanical properties: super-plasticity, increased hardness, etc.

BUT

Can we use nanocrystalline materials in environments with "extreme" radiation doses (fusion reactors, space applications)?

20 keV,
12 nm grains

Ion bombardment ➔ localized "shocks" ➔ behavior of materials under extreme pressure/temperature conditions.
Can we create new, better materials (new phases, metastable states, etc.) using high-pressure loading?

BULK: ZM. Samaras *et al.* [PRL **88** (2002) 125505] and W. Voegeli *et al.* [NIMB **202** (2003) 230], found that irradiation can lead to grain size changes and that grain boundaries absorb most point defects.
SURFACE: No radiation damage studies to the best of our knowledge.

keV ion bombardment simulations

MDCASK (LLNL): parallel, variable step
Runs at NERSC and MCR.
Potential: EAM (Mishin et al.)+ ZBL.
Targets: ~500,000 Cu atoms, 300 K.
Cu projectile: 5-30 keV, normal incidence, hitting at different points on the surface (including different grains)

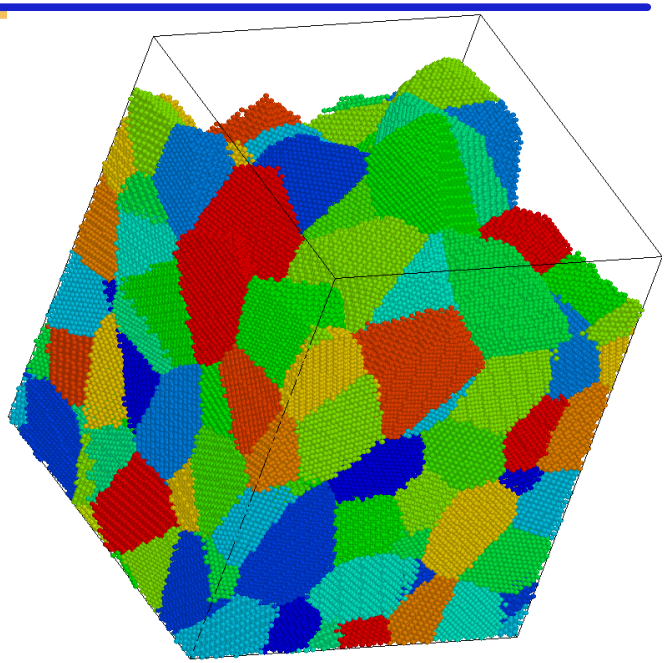

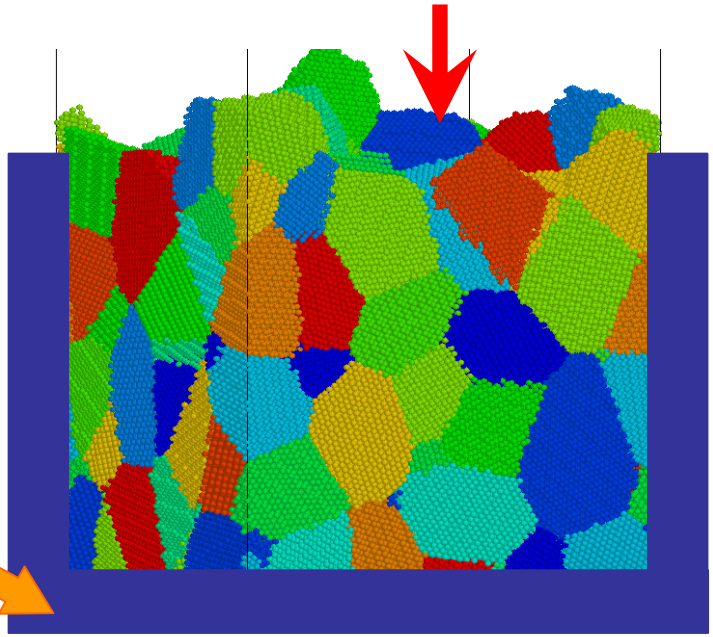

Thermostat at sides and bottom to minimize boundary effects

A. Caro, M. Victoria

3D nanocrystal, 5 nm grain size: use Voronoi construction [H. Van Swygenhoven *et al*. PRB 60, 22 (1999)]➔ remove grains with center-of-mass above desired surface ➔ rough surface ➔ relax during 70 ps with temperature ramp (1200-300 K) ➔ 3 ps additional relaxation at 300 K ➔ bombard

Single crystal vs. nanocrystal bombardment

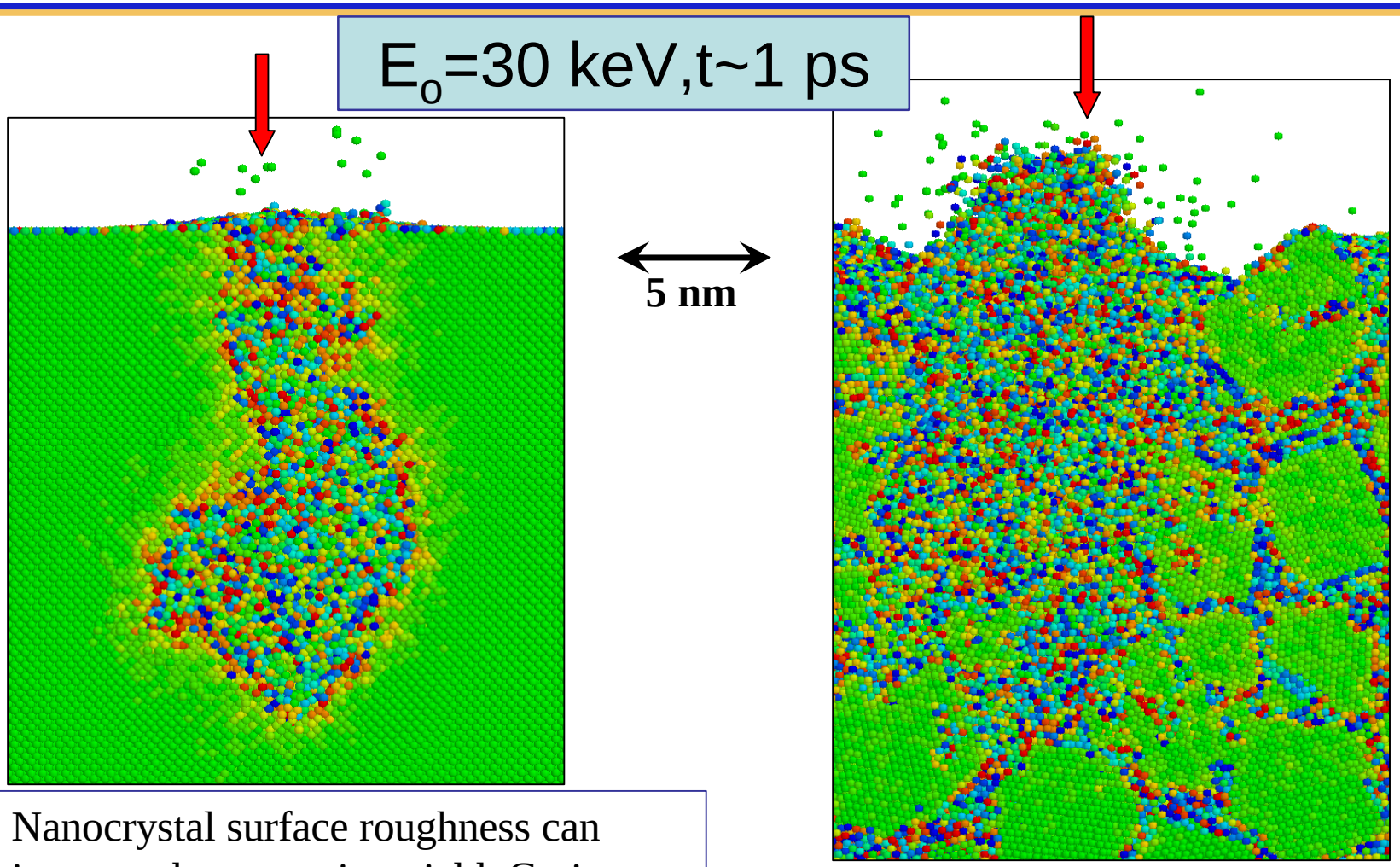

Nanocrystal surface roughness can increase the sputtering yield. Grains and grain boundaries can melt during the ballistic phase of the cascade.

cascade in nc is a “high-yield” case

10 keV bombardment

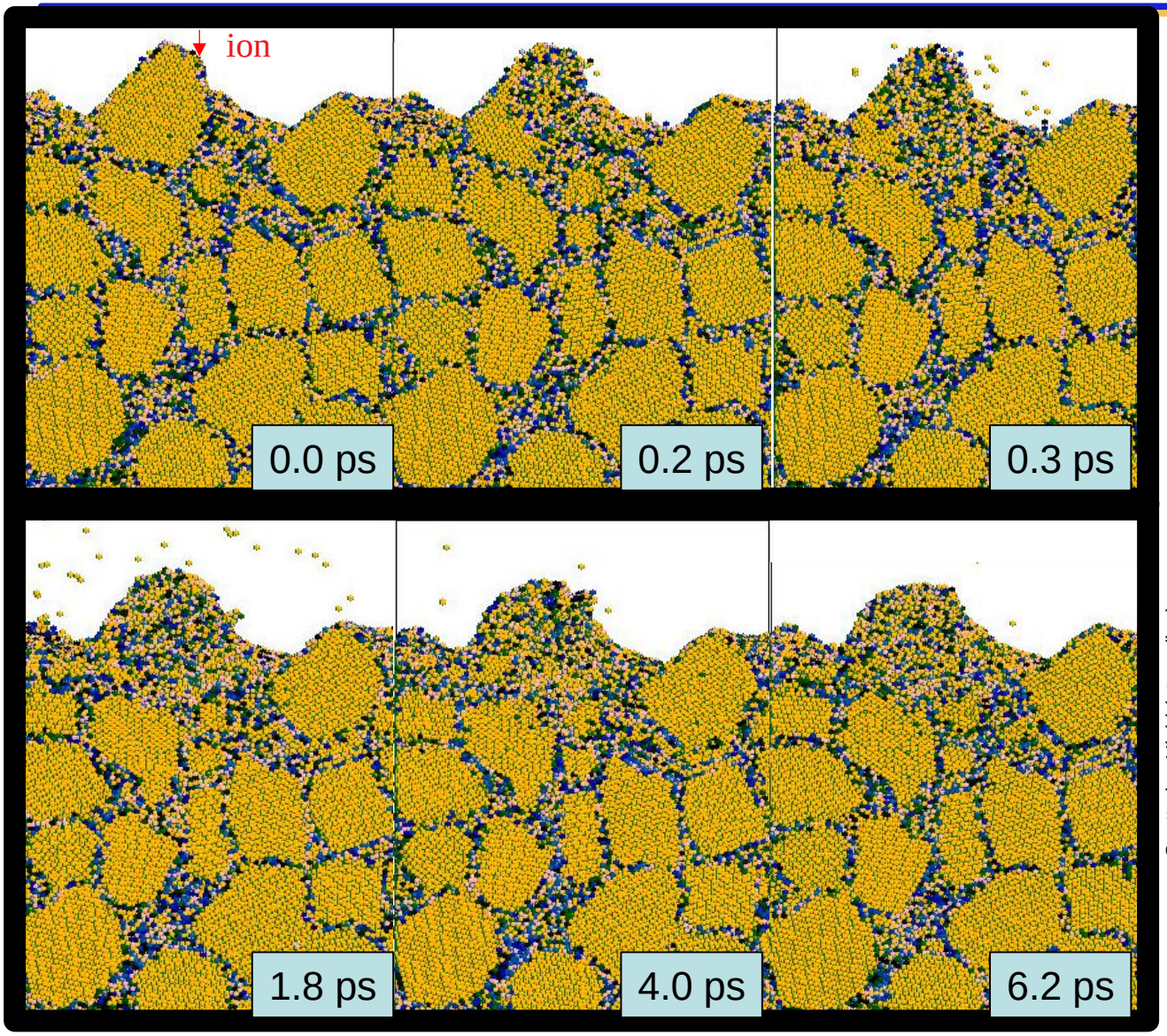

High yield case (Y~4 <Y>)

Cascade mostly confined to a "hillock" grain.

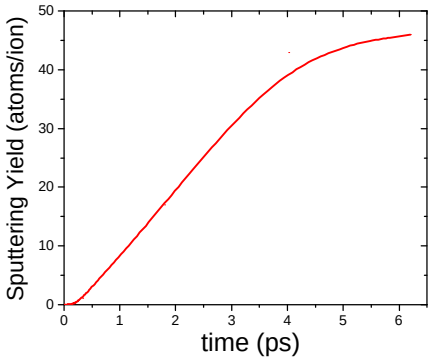

Radiation-induced micro-structural changes

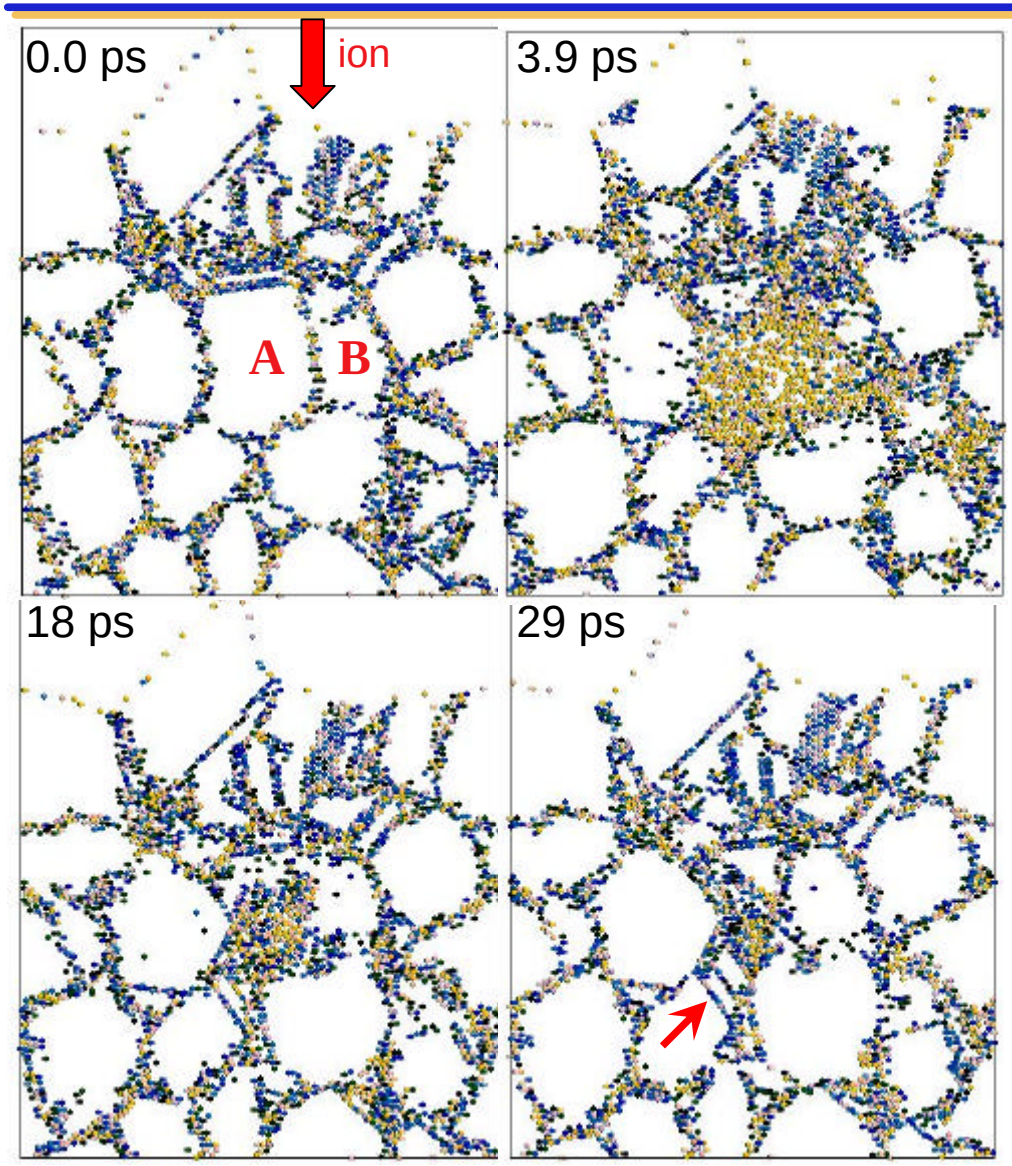

30 keV bombardment
(slices are a_o thick)

Grain re-construction

Similar to previous bulk studies, since cascade center is ~10 nm below the surface. Grains A and B are molten during the thermal-spike phase, and they form new grains, together with stacking faults (red arrow, 30 ps). Lesser degree of reconstruction is seen at lower bombardment energies.

Summary of nc bombardment by keV ions

- **Bombardment of nanocrystalline Cu at normal incidence, in the energy range 5-30 keV leads to the same sputtering yield than bombardment of single crystals/large polycrystals.**
- **Bombardment does lead to large structural changes, due to melting and re-crystallization of entire grains, as previously observed by others in bulk simulations.**
- **Modeling work in progress: improving statistics on current calculations, incidence at an angle, electronic sputtering.**
- **Experimental work in progress: irradiation of nc (keV-MeV). High strain rate, high pressure loading of nc [20-80 GPa, *Science* (2005)].**

MeV-GeV ions: (fission) track evolution

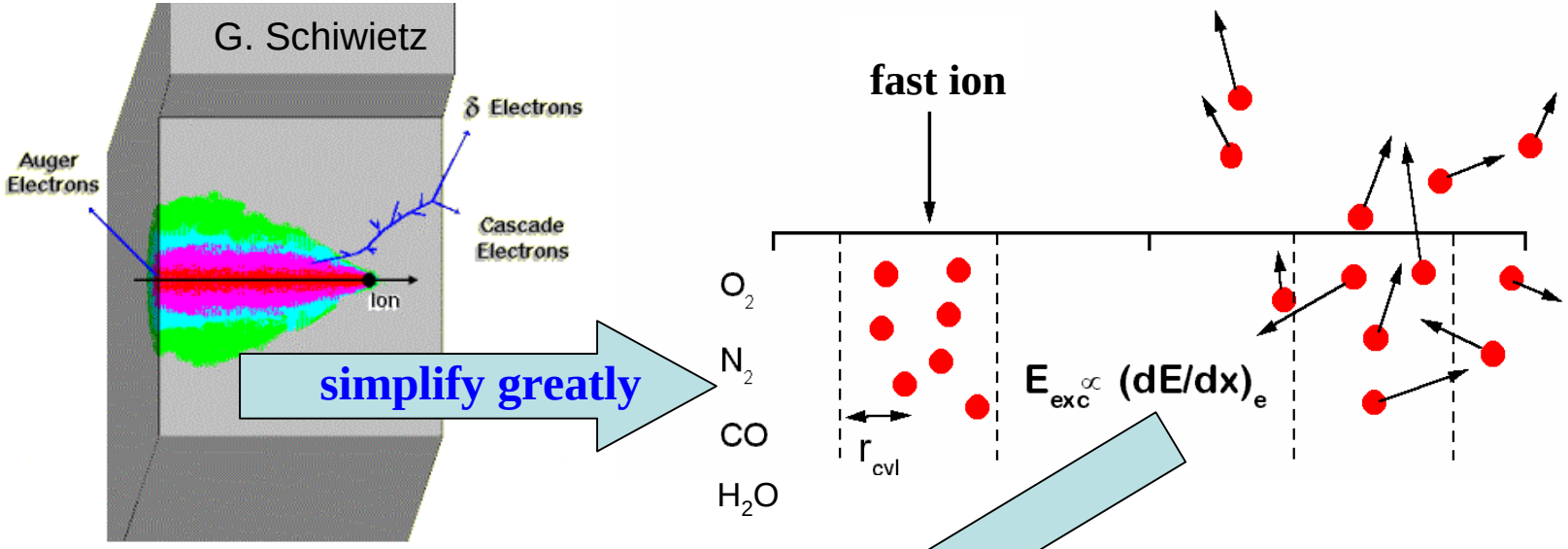

Two main "competing" models

Coulomb Explosion

Thermal Spikes

Fleisher, Price and Walker,

J. App. Phys. 36**, 3645 (1965)**

Trautmann, Klaumunzer and Trinkaus,

Phys. Rev. Lett. 85**, 3648 (2000)**

MORE ….

But …

Coulomb Explosion and Thermal Spikes are early and late aspects of the same repulsive decay process

Bringa and Johnson, PRL **88**, 165501 (2002)

MD simulation of tracks (MeV-GeV)

- **Atomic and Molecular Solids** Lennard-Jones, Morse, EAM, oxides, etc. U~0.08 eV-7 eV
- Atoms /molecules within r_{cyl} can receive extra $KE = E_{exc}$, extra charge Z, or antibonding potential

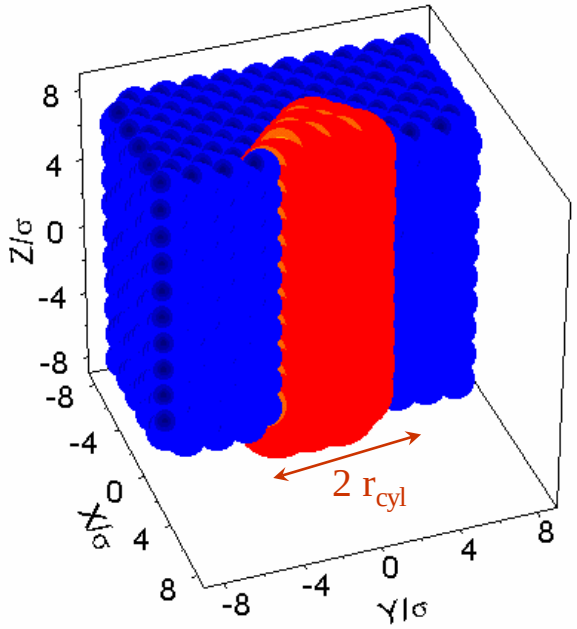

- U=binding energy, ~few eV's (metals, insulators), ~0.1 eV ("ices").
- $(dE/dx)_{eff}$=amount of energy contributing to the track formation

  $(dE/dx)_{eff}$ μ (dE/dx), $(dE/dx)^2$, $(dJ/dx)^2$
- r_{cyl}= "track" radius

  $r_{cyl} \sim r_{Bohr}$, $r_{ultra\text{-}track}$, $r_{cyl}[(dE/dx)_{eff}]$
- Can also use MD+TTM (two temperature model) to include e-phonon

Bringa and Johnson, PRB & NIMB, several papers

Combined Two Temperature Model (TTM) – MD

D. Ivanov, L. Zhigilei (UVa), B. Sadigh, E. Bringa (LLNL)

$$\begin{cases} C_e(T_e)\dfrac{\partial T_e}{\partial t} = \dfrac{\partial}{\partial z}\left(K_e(T_e)\dfrac{\partial}{\partial z}T_e \right) - G(T_e - T_l) + S(z,\ t) \\ C_l\dfrac{\partial T_l}{\partial t} = \dfrac{\partial}{\partial z}\left(K_l\dfrac{\partial}{\partial z}T_l \right) + G(T_e - T_l) \end{cases} \Longrightarrow \textbf{MD}$$

$$\text{TTM} \quad : \quad C_e(T_e)\frac{\partial T_e}{\partial t} = \frac{\partial}{\partial z}\left(K_e(T_e)\frac{\partial}{\partial z}T_e \right) - G(T_e - T_l) + S(z,\ t)$$

$$\text{MD} \quad : \quad m_i\frac{d^2\vec{r}_i}{dt^2} = \vec{F}_i + ?m_i\frac{d\vec{r}_i}{dt} \quad \text{with} \quad ? = G\,(T_e - T_l)\Big/\sum_i \frac{\left|\vec{p}_i^{\,T}\right|^2}{m_i}$$

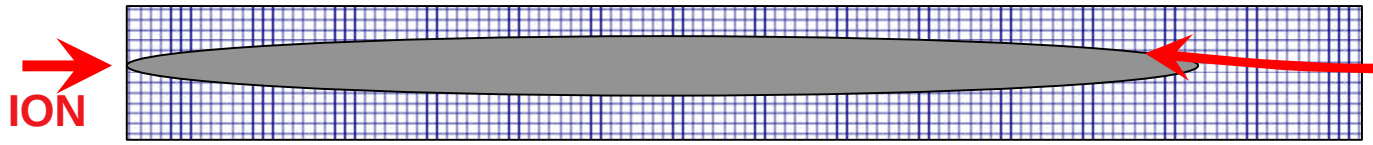

Electronic energy deposition

Toulemonde *et al.*: “Thermal spike” where heating is provided by secondary electrons → spike radius large and E/atom low ➔ neglecting pressure effects is OK.
TTM (no MD ➔ no pressure/surface) ➔ successful to understand track size data
Problems with sputtering data ➔ use more accurate MD+TTM

Coulomb explosion simulations

N_{ch}=2, a~l, r_{track}~l, τ=1 ps~2 τ_D

charged atoms have twice the radius of neutral atoms

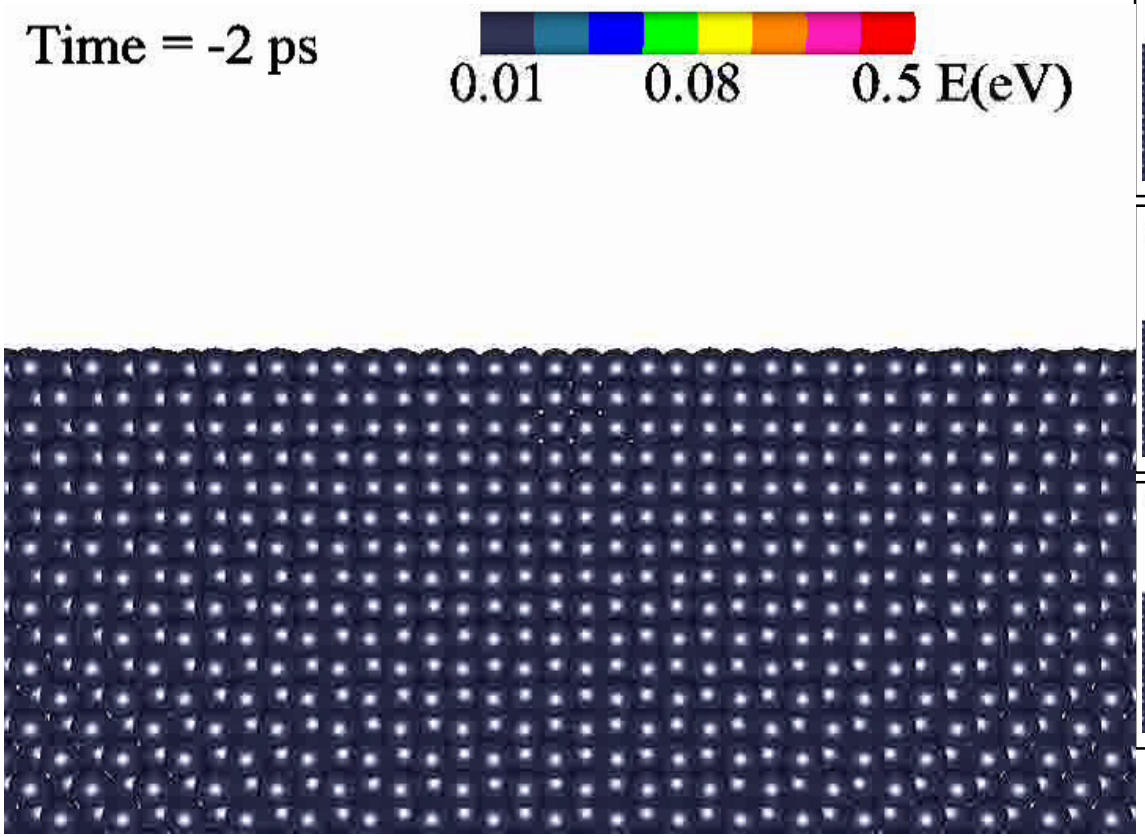

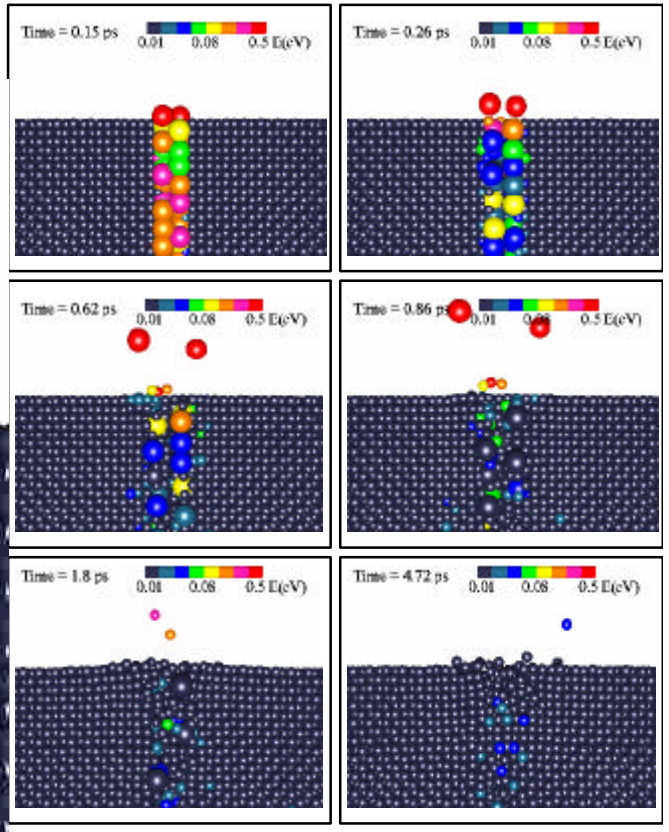

Bringa and Johnson, PRL **88**, 165501 (2002)

MD simulations of amorphization in oxides

P. Durham *et al*. (Astrophys. J. Lett., accepted) & Devanatham *et al*. (NIMB, in press)

- DL_POLY with parallel domain decomposition,
- 32-128 CPUs, 10^4-1.25 10^6 atoms.
- Buckingham potential + SPME
- Thermal spike model
- Excellent agreement with experimental results (Bringa et al, submitted).

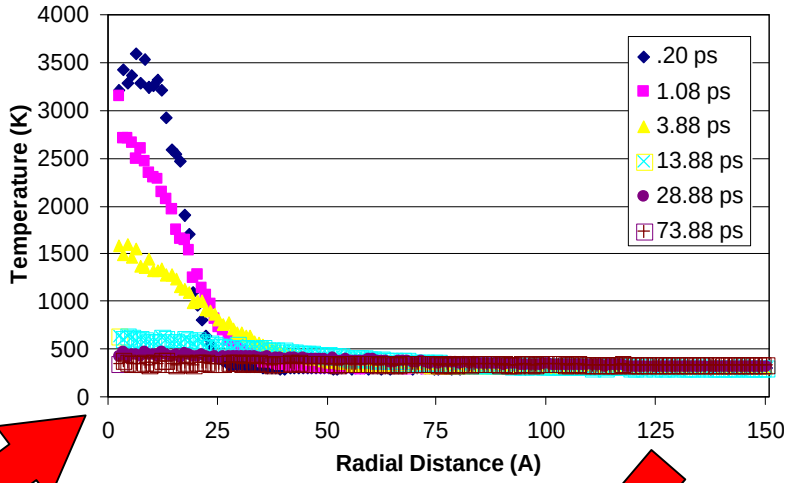

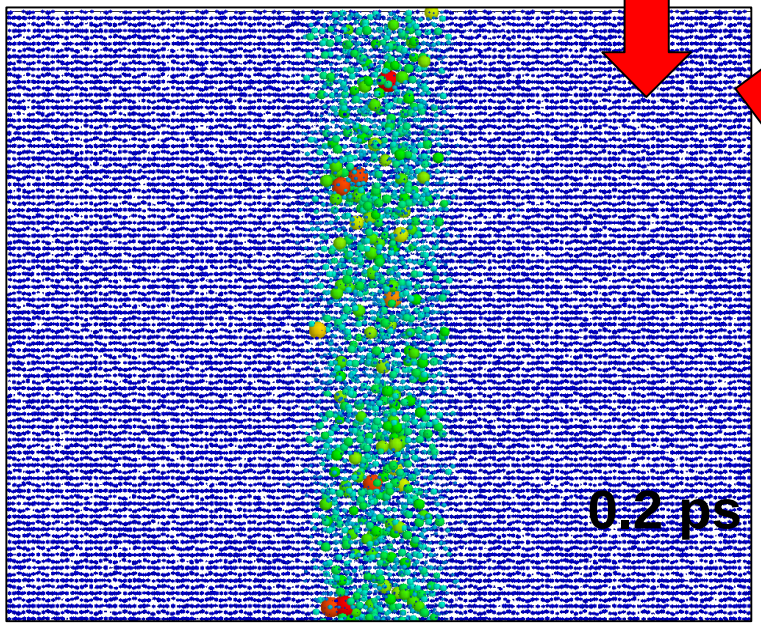

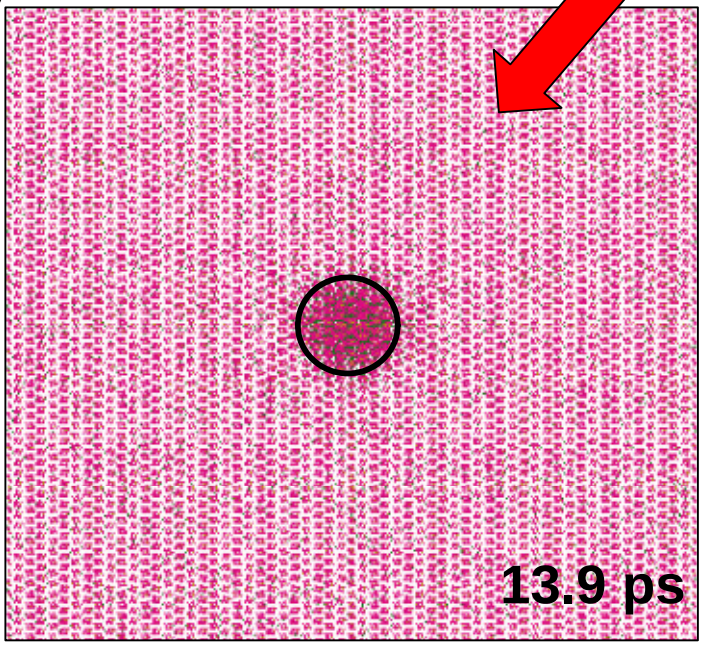

Simulation of tracks in carbon materials

Schwen & Bringa, NIMB 2007 (in press).

Samples with 21x21x7 nm, using REBO potential, $R_{track}(0)$= 3 nm, E_{exc}/atom=3 eV.
Change efficiency η of electron-phonon coupling ➔ comparison with experiments
(no amorphization for diamond) leads to bounds for the experimental efficiency.

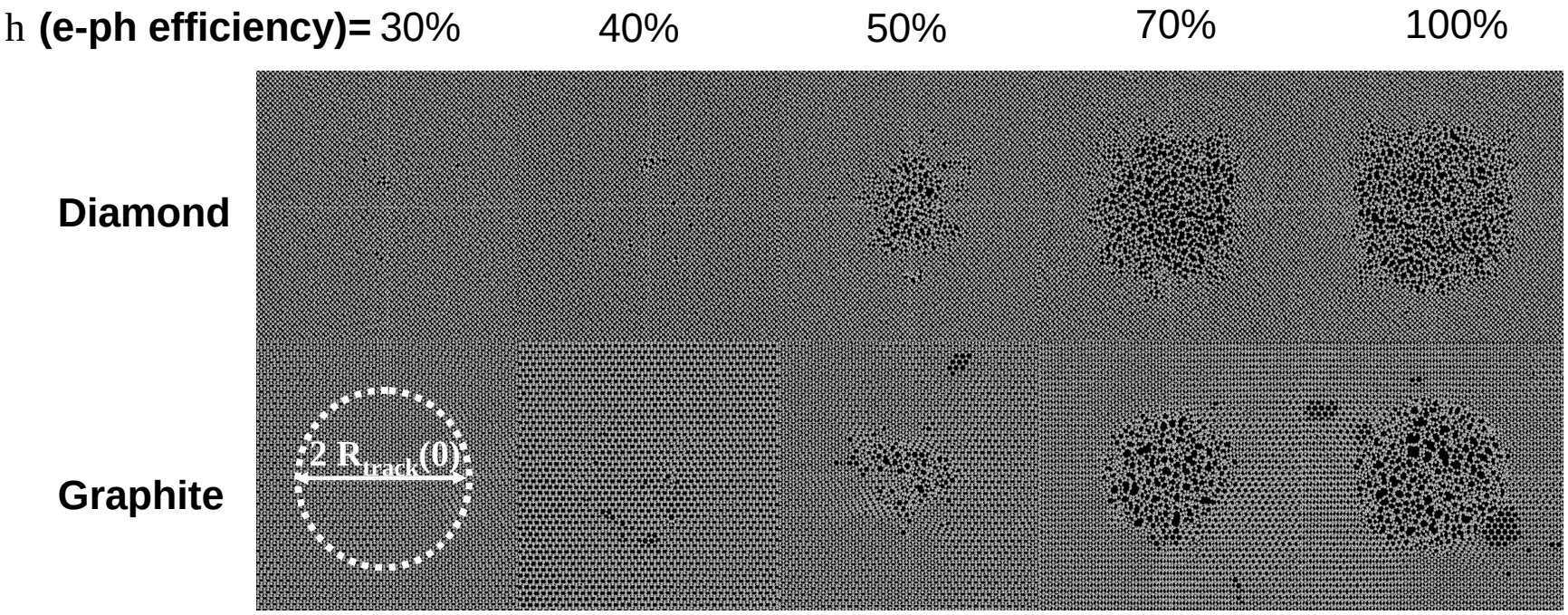

Efficiency can shift with pressure (Glasmacher et al., PRL 2006),
compositional changes (Arnoldbik et al., PRL 2005),
or by cluster bombardment (Dunlop et al., several).

Simulation of tracks in carbon materials

MD reproduces density decrease and graphitization of diamond-like targets

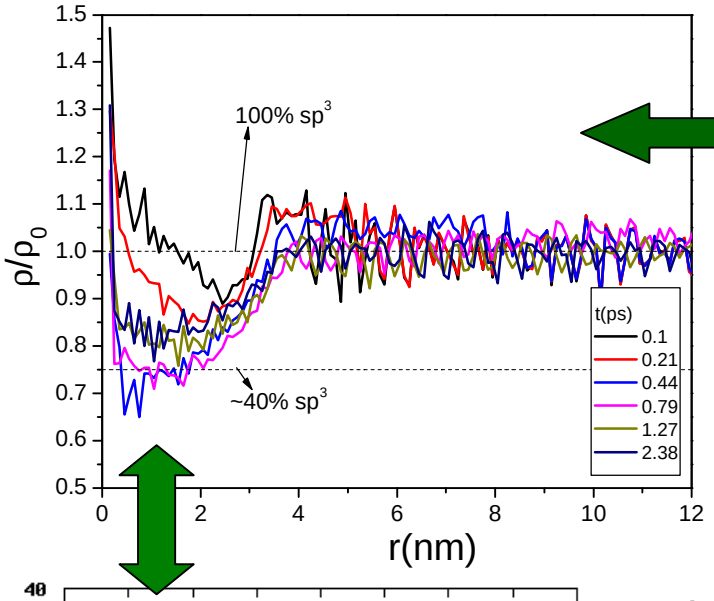

From XPS experiments
[Haerle et al., PRB 2001]
$sp^3[\%]=[\rho(g/cm^3)-1.92]/0.0137$

Good agreement with hybridization based on bond counting

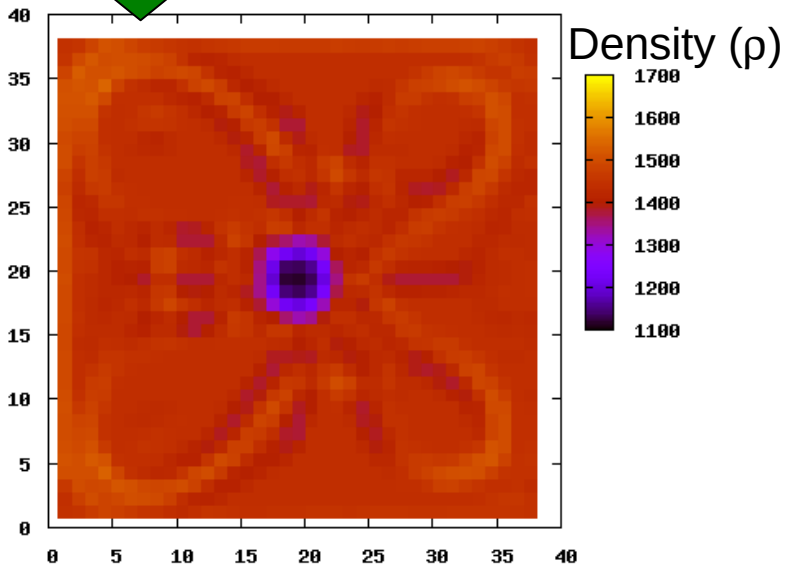

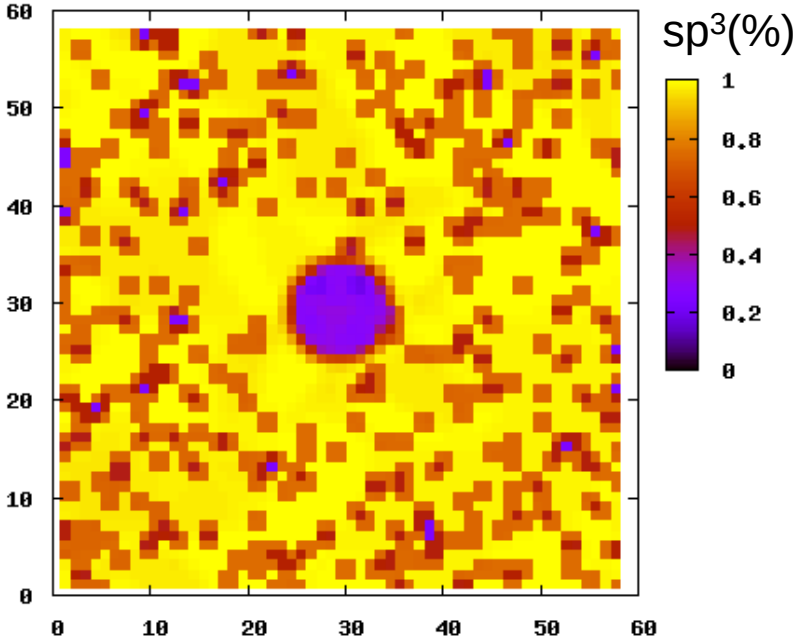

Future outlook

•MD ➔ new behavior and improved models at higher scales; sheds light on current experiments and suggest new experiments.

• We can simulate bcc/hcp metals, He bubbles, many different oxides, etc. Reactive potentials available for many materials.

•Large computational power ➔nearly direct comparison between simulations and experiments.

On going simulations at Thunder/BGL (LLNL, up to 128,000 CPUs), comparing MD with hydro-code modeling and experiments: cluster bombardment of nano-foams (with F. Abraham), etc.

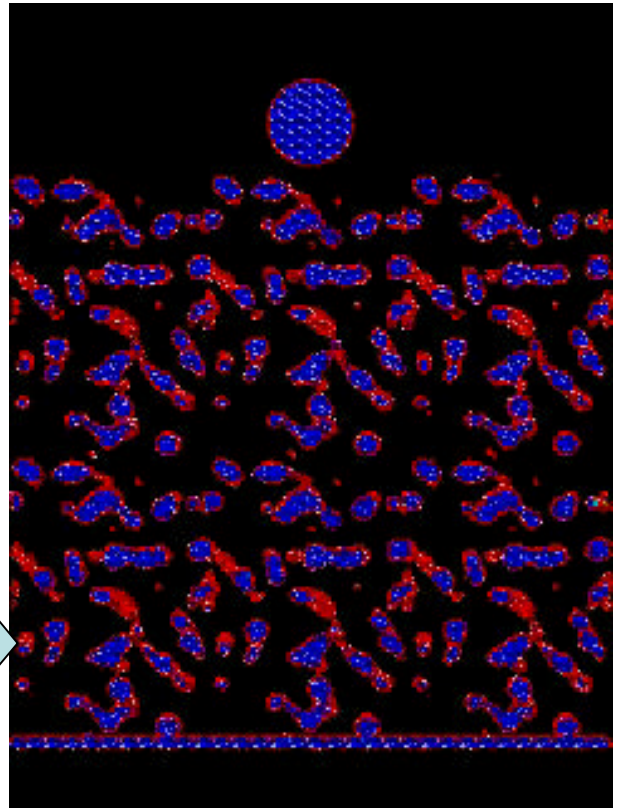

chemistry & materials science
CMS

Computational Thermodynamics
The Challenge of Fe-Cr

MRS Fall Meeting

Boston

Nov 27- Dec 1

2006

Alfredo Caro

Chemistry and Materials Science
Lawrence Livermore National Laboratory

Thermodynamic package:	**E. M. Lopasso (Argentina), M. Caro (LLNL)**
Monte Carlo code:	**B. Sadigh (LLNL)**
CALPHAD interface:	**M. Caro (LLNL), P. Turchi (LLNL)**
Model for alloy potentials:	**D. Crowson (Virginia Tech)**
***Ab initio* data:**	**P. Klaver (Belfast-UK)**
Behavior under irradiation:	**S. Srivilliputhur (LANL)**
Dislocation mobility:	**J. Marian (LLNL)**
GB mobility:	**D. Farkas (Virginia Tech)**

This work was performed under the auspices of the U.S. Department of Energy by the University of California Lawrence Livermore National Laboratory under Contract No. W-7405-Eng-48.

Objective

High thermal efficiency and long lifetime operation of advanced nuclear systems demand structural materials for the following critical performance:

1- High strength at T up to 700 C

2- High resistance to neutron irradiation up to 100 dpa or more (swelling and embrittlement)

3- High resistance to corrosion in coolants such as SCPW, LBE, Na

Several avenues are explored in different countries:

F/M – ODS, High Cr-ODS are considered the most promising

As an introduction to present day knowledge about high performance nuclear materials, a few transparencies on the Japanese R&D in the area:

chemistry & materials science CMS

High Burnup Fuel Cladding Materials R&D for Water-cooling Nuclear Power Plants -- Nano-sized ODS Steels--

A. Kimura[1], H.S. Cho[2], N. Toda[2], R. Kasada[1], H. Kishimoto[1], N. Iwata[1], S. Ukai[3] and M. Fujiwara[4]

[1]Institute of Advanced Energy, Kyoto University, Kyoto, Japan
[2]Graduate School of Energy Science, Kyoto University, Kyoto, Japan
[3]Japan Atomic Energy Agency, Ibaraki, Japan
[4]KOBELCO Research Institute, Kobe, Japan
kimura@iae.kyoto-u.ac.jp

Nano-scaled Oxide Dispersion

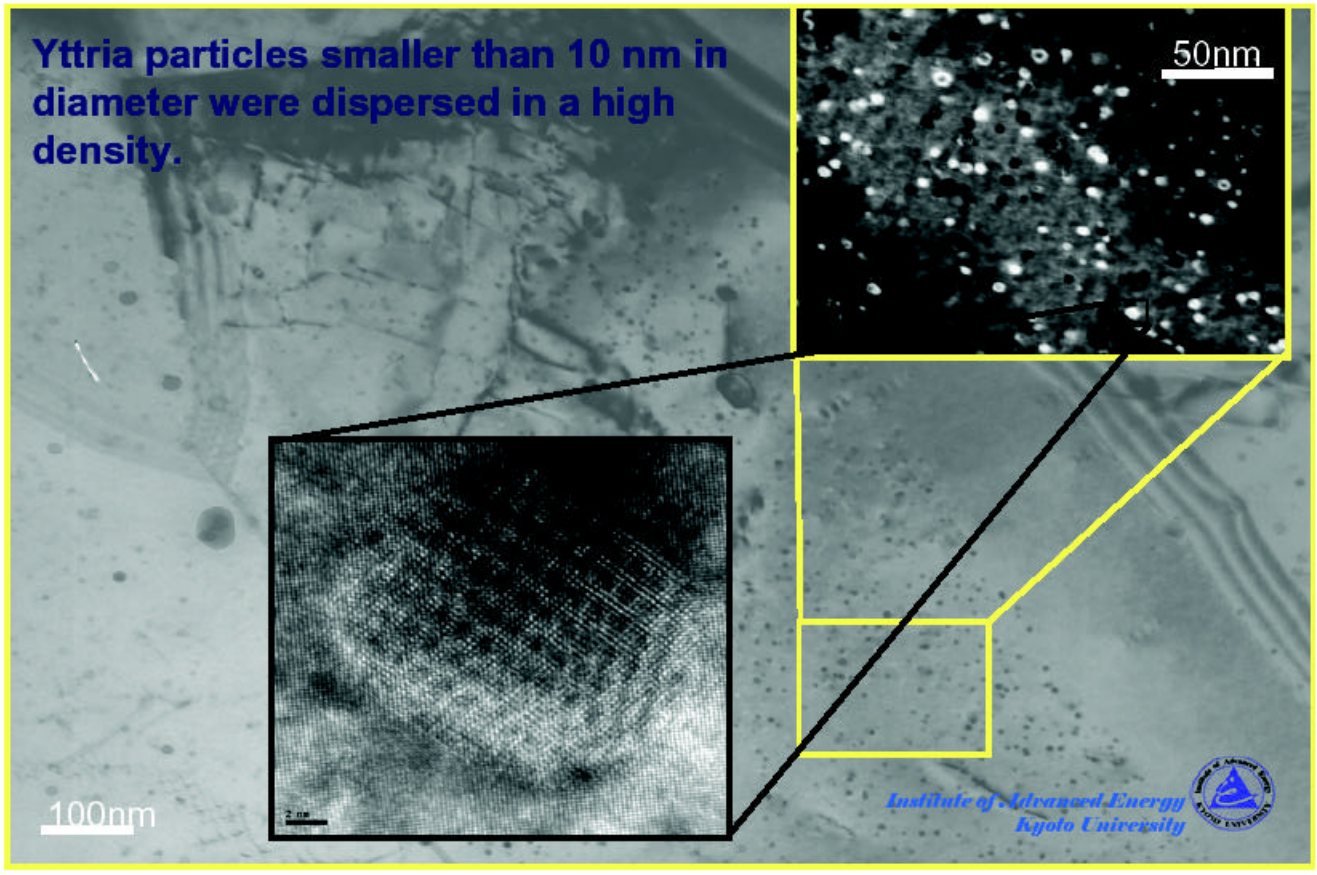

Materials - High Cr ODS Steels

The 9Cr-ODS steel developed for the cladding of sodium cooled fast reactor is inadequate for the application to SCWFR and LBEFR because of corrosion issues.

⇨ ***High Cr ODS steels added with Al were produced.***

	Materials	Compositions	Alloys
K1	19Cr-ODS	19Cr+0.37Y_2O_3	Ferritic ODS steel
K2	14Cr-ODS	14Cr+4.5Al+0.38Y_2O_3	Ferritic ODS steel
K3	16Cr-ODS(2)	16Cr+4.5Al+0.37Y_2O_3	Ferritic ODS steel
K4	19Cr-ODS(3)	19Cr+4.5Al+0.37Y_2O_3	Ferritic ODS steel
K5	22Cr-ODS(3	22Cr+4.5Al+0.37Y_2O_3	Ferritic ODS steel

- **Increase Cr concentration**
- **Add 4.5wt.%Al**

High-temperature Strength

Drastic improvement has been achieved.

Tensile Stress:
415MPa at 700°C
300MPa at 800°C

Creep Strength (9Cr):
120MPa at 700°C
for 10^4 hr

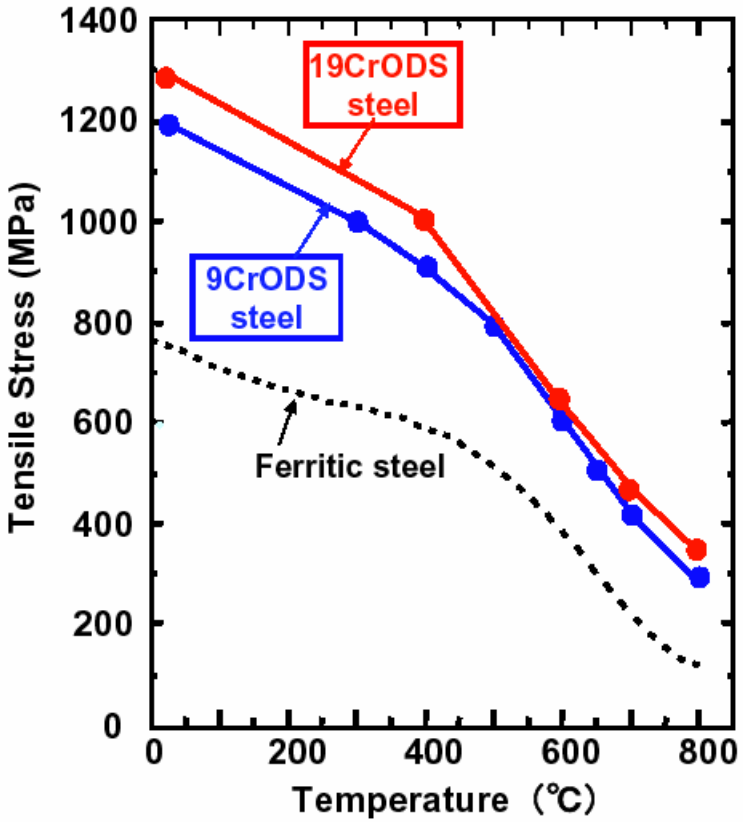

LBE Corrosion Resistance

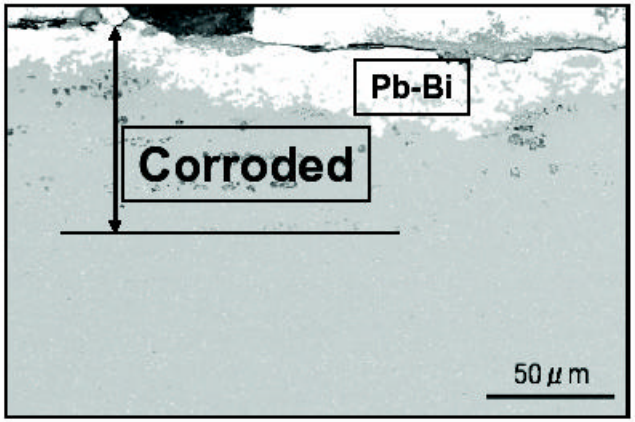

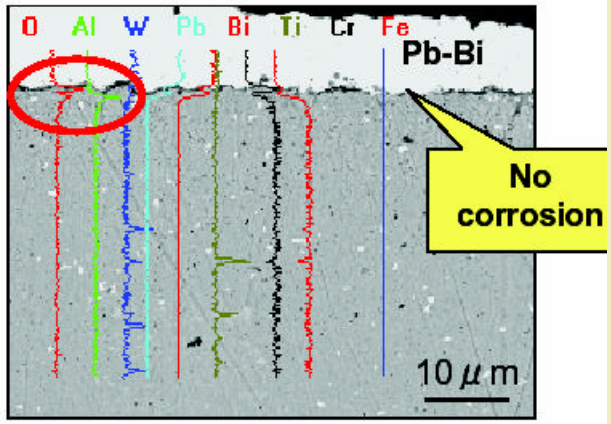

9Cr-ODS steel
Temperature: 650 °C
$C(O_2)$: 10^{-6}wt%O_2
Period: 10,000h
Closed loop

19Cr-4Al-ODS steel
Temperature: 650 °C
C(O2): 10-6wt%O_2
Period: 10,000h
Closed loop

Formation of Al_2O_3 → Resistance to LBE corrosion

ISSUE! Reduction of strength by Al addition

A Trade Off Issue

An increase in Cr content is:

1) an advantage for "Corrosion Resistance", but
2) a disadvantage for "Aging Embrittlement".

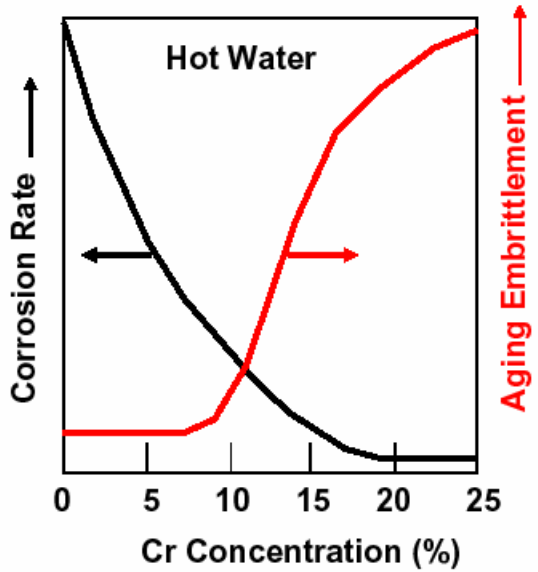

Goal:

Development of a corrosion resistant "Super ODS steel" with maintaining high resistance to aging and irradiation embrittlement.

Aging Effects (K3: 16Cr-4Al)

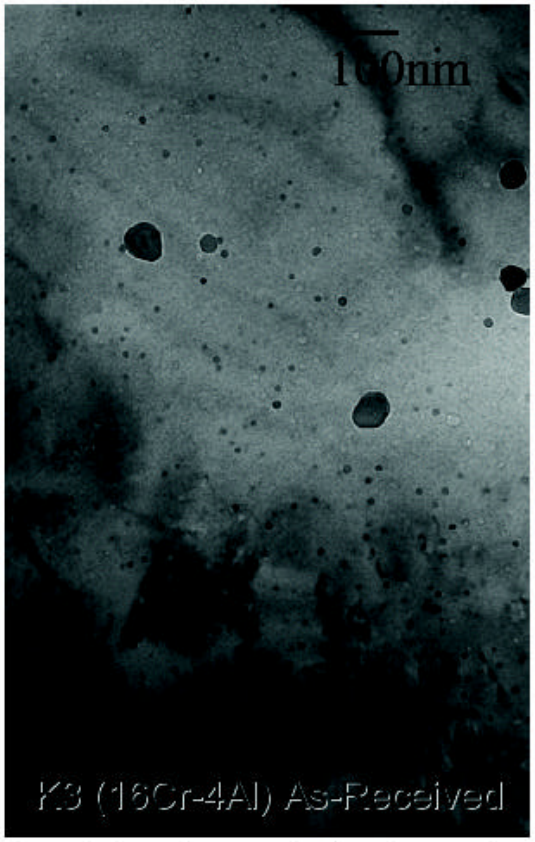

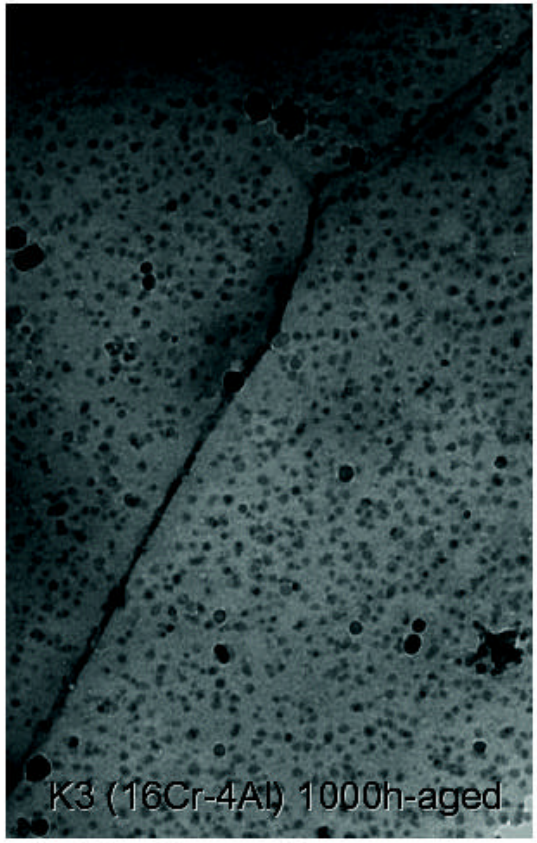

Cr-rich phase (α'-phase) appeared after the aging

Aging Embrittlement

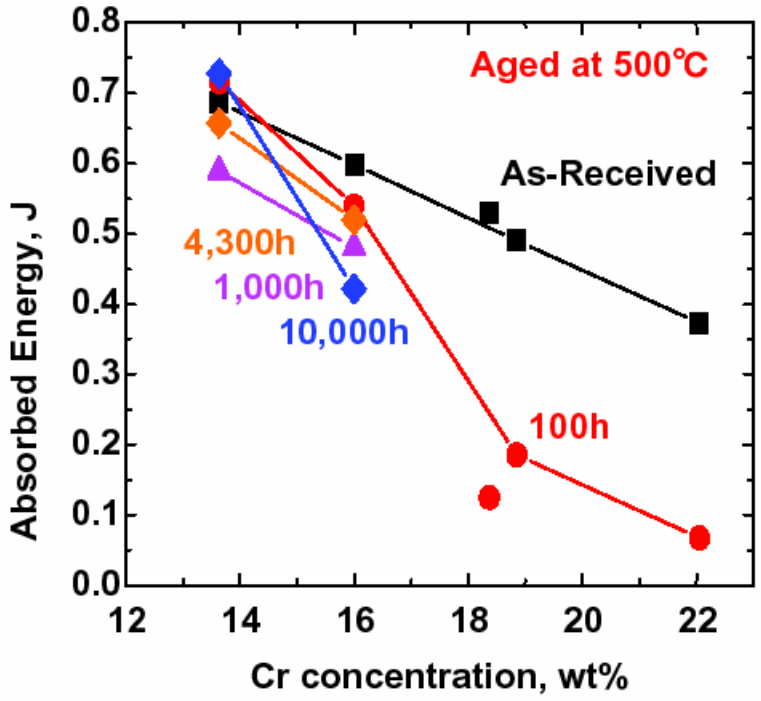

Cr content > 18 w.%
Remarkable degradation

Cr content = 16 w.%
Not large up to 10,000 hr

Cr content = 14 w.%
No effect

Roles of Nano-oxide Particles

1. Corrosion resistance
   > Homogeneous Cr_2O_3 or Al_2O_3 formation

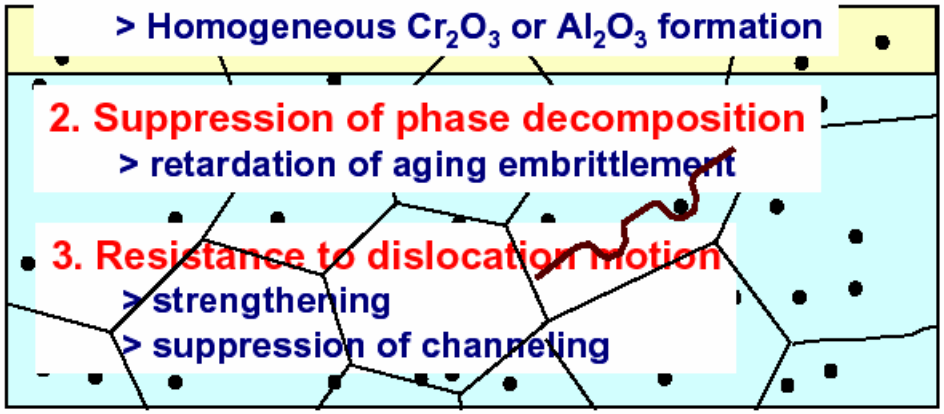

● KEY TECHNOLOGIES

1) Nano-scaled (5nm) oxide dispersion
2) Meso-sized (<1μm) grain size/shape control

Achievement of
High-resistance to corrosion
High-temperature strength
High-resistance to irradiation

We work on:

1. an approach to potentials for alloys
2. a thermodynamic package: entropy - meter
3. a parallel Monte Carlo code w/displacements

chemistry & materials science CMS

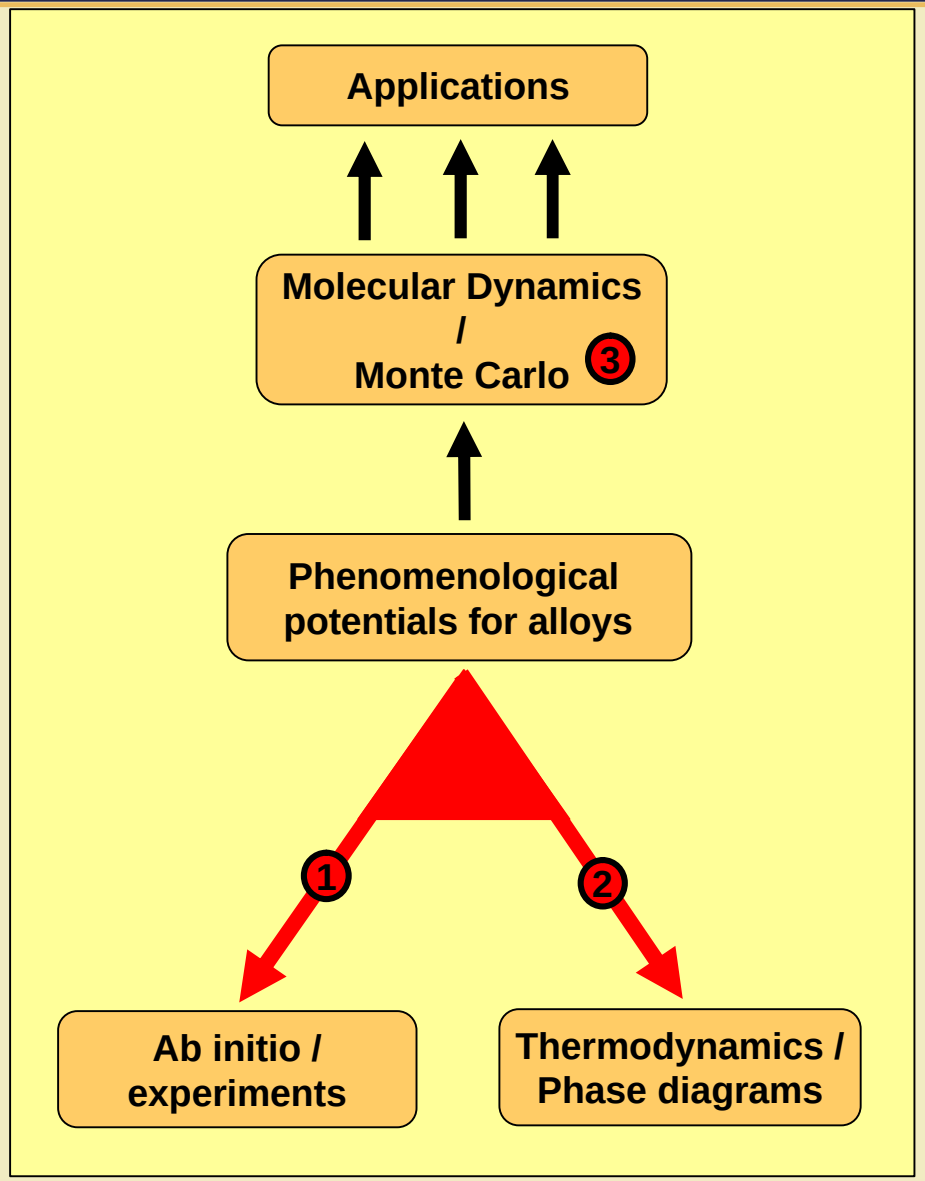

Fe-Cr is not fully understood: Radiation induced precipitation is at odds with assessed phase diagram

chemistry & materials science CMS

Experimental Phase Diagram of Fe-Cr

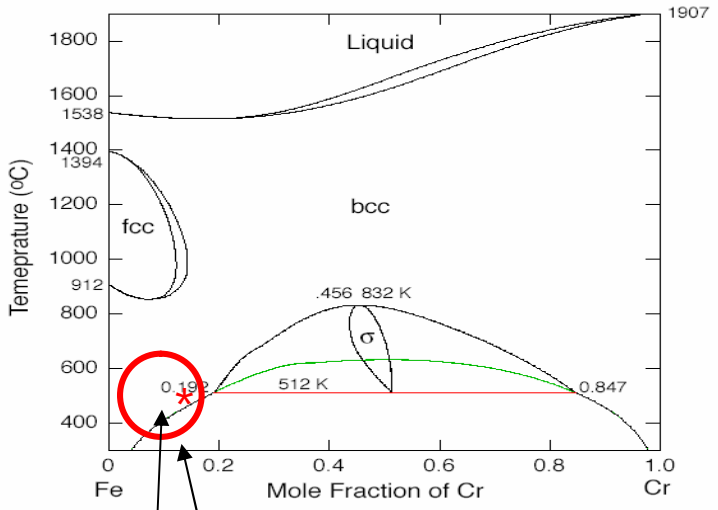

nuclear applications

Source: CALPHAD

Experimentally observed precipitation

et al. 2001, Sagaradze et al. 2003

Recent significant *ab initio* findings: magnetic effects determine the formation energy

The heat of solution of Fe-Cr shows a change in sign at low Cr content.

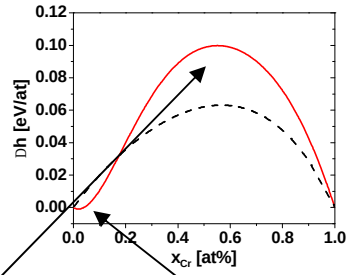

Olsson et al. 2003 - et al. 2006

- **Positive** heat of solution
- Magnetic frustration when Cr are nearest neighbors

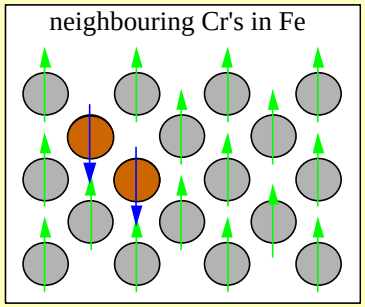

Concentrated solution

- **Negative** heat of solution
- Dilute Cr aligns anti-ferromagnetically in Fe

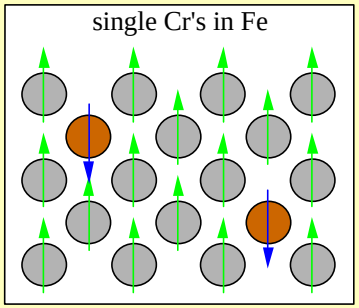

From P. Klaver

Dilute solution

Experimental phase diagram of Fe-Cr

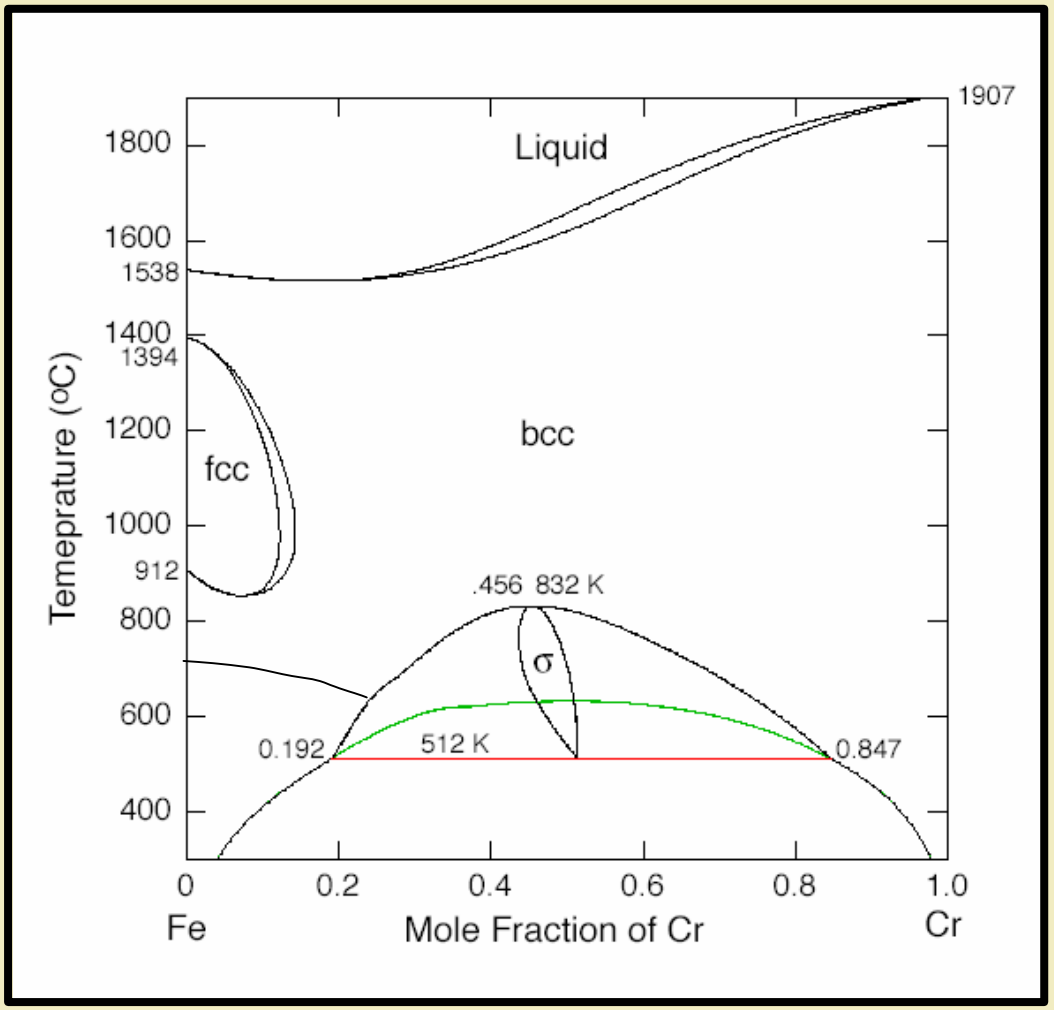

The goal was to develop an empirical potential that captures this unusual behavior

chemistry & materials science CMS

- Our empirical many body potential for concentrated alloys

$$E = \sum_{i}^{N}[F_{ai}(\sum_{j\neq i} r_{ai,bj}(r_{ij})) + 1/2\sum_{j\neq i} V_{ai,bj}(x, r_{ij})]$$

$$V_{ai,bj}(x,r) = h(x)\, v_{AB}(r)$$

h(x) **is obtained using a Redlich-Kister expansion of the heat of solution (CALPHAD methodology)**

Energy depends on composition

Phys. Rev. Lett. 95 075702 (2005)

- Our model reproduces exactly the target heat of solution for arbitrarily complex alloys

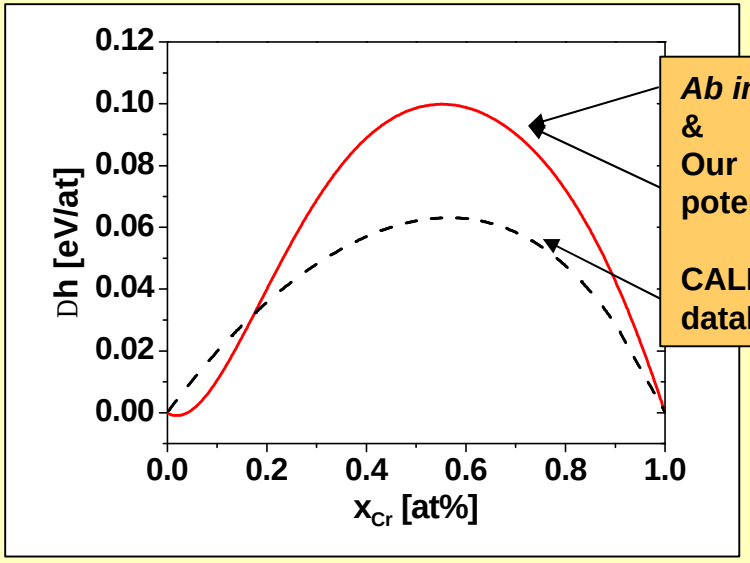

Fe Cr heat of formation

Repulsion between two Cr atoms reflects the nature of the magnetic frustration

Strength (~ 300 meV) and range (~2.2 a_0) are captured by the classical potential

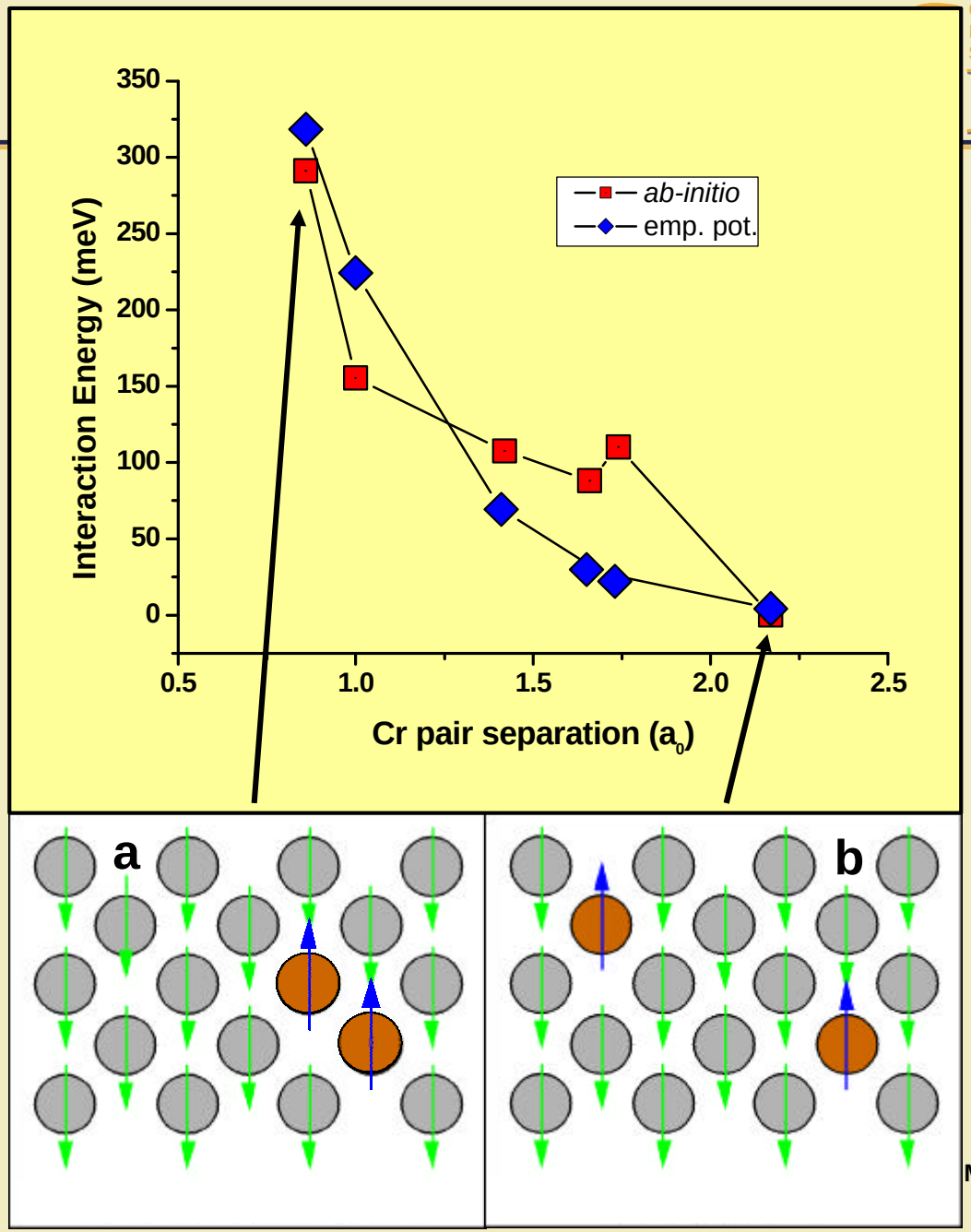

Computational Thermodynamics: We developed a suite of codes to evaluate free energies

chemistry & materials science CMS

The basic assumption that links thermodynamics to MD is ergodicity:

$$\overline{A_t} = \langle A \rangle$$

Where the l.h.s. is a time average:

$$\overline{A_t} = \frac{1}{t - t_0} \int_{t_0}^{t} A(x(t))dt$$

And the r.h.s. is an ensemble average:

$$\langle A \rangle = \frac{\int_{\Omega} A(x)\exp(-H(x)/kT)dx}{\int_{\Omega} \exp(-H(x)/kT)dx}$$

How to obtain phase diagrams from total energy recipes

But free energy F is not an ensemble average:

$$F = -kT \ln\left(\int_{\Omega} \exp(-H(x))dx\right)$$

We have developed a series of codes to calculate free energies by doing:

- **Switching Hamiltonians**
- **Gibbs – Duhem integration**
- **Gas expansion**
- **…**

Phys. Rev. **B 66**, 054201, (2002)
Phys. Rev. **B. 68**, 214205 (2003)
J. Nuc. Mat. **336**, 233 (2005)
J. Nuc. Mat. **349**, 317 (2006)

An entropy-meter

Our results for bulk phases: Free energy of the FM bcc phase of Fe-Cr

chemistry & materials science CMS

Free energy F(x,T) is the main input in equilibrium calculations, and one of the two components in non equilibrium calculations.

There is one such surface for every phase of interest, ideally: ferromagnetic, paramagnetic, sigma, gamma, martensite, perlite, etc

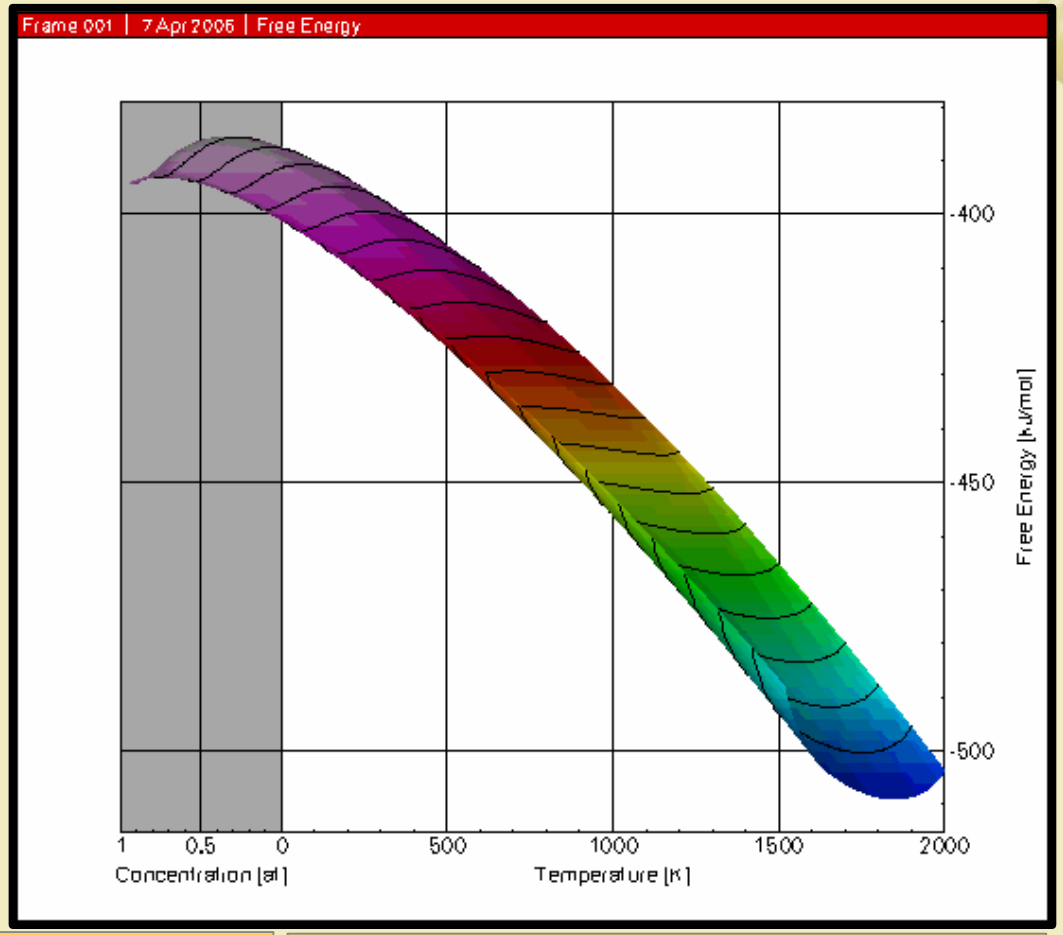

Free energy of ferromagnetic bcc Fe-Cr → Phase diagrams from total energy recipes

APPLIED PHYSICS LETTERS **89**, 121902 (2006)

Implications of *ab initio* energetics on the thermodynamics of Fe–Cr alloys

A. Caro[a] and M. Caro
Chemistry and Materials Science Directorate, Lawrence Livermore National Laboratory, Livermore, California 94550

E. M. Lopasso
Centro Atmico Bariloche—Instituto Balseiro, 8400 Bariloche, Argentina

D. A. Crowson
Virginia Polytechnic Institute and State University, Blacksburg, Virginia 24061

chemistry & materials science
CMS

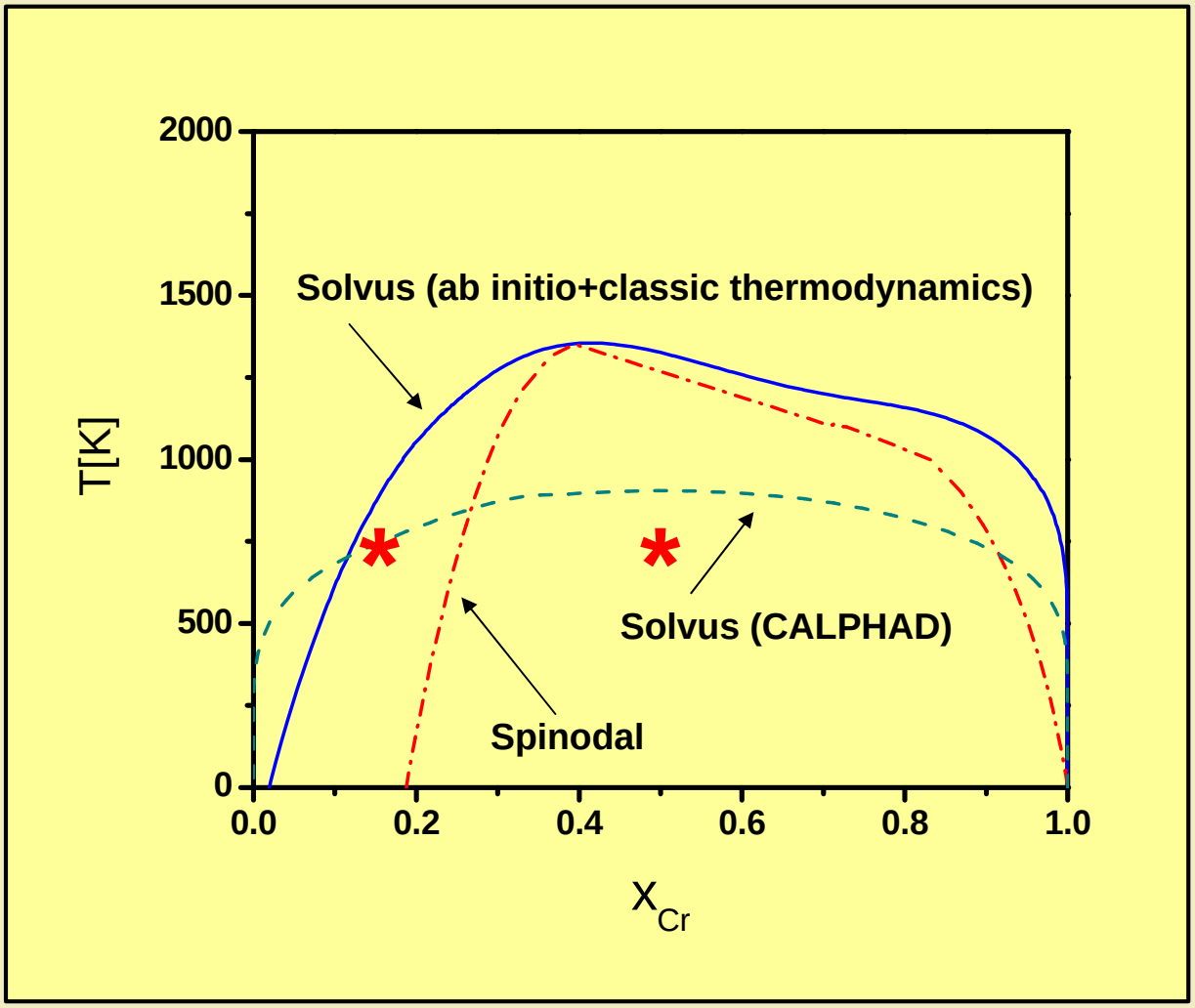

Only the ferromagnetic phase is shown

Lattice vs displacement MC

chemistry & materials science CMS

Lattice Monte Carlo	3	Monte Carlo with displacements

Solid solution → Precipitate

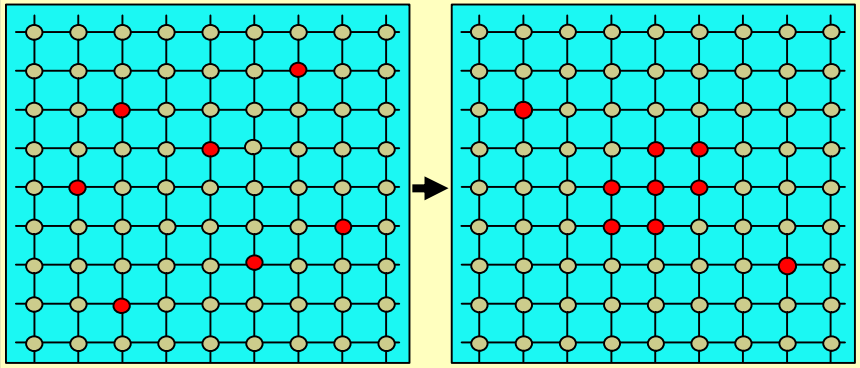

$$\Delta G = -V\,\Delta E + \gamma'$$

Solid solution → Precipitate

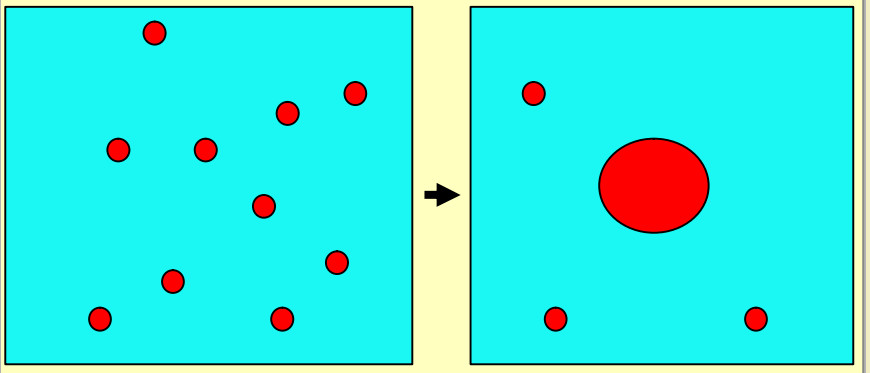

$$\Delta G = -V\,(G_\beta - G_\alpha) + A\,\gamma + V\,\Delta G_{el} + V_{Ext}$$

Lattice MC could give time evolution (k-MC), at the price of neglecting several terms in the driving force. Displacement MC accounts for all terms in the driving force, but does not give time evolution

Homogeneous precipitation in Fe Cr
T = 750K ; x = 0.15

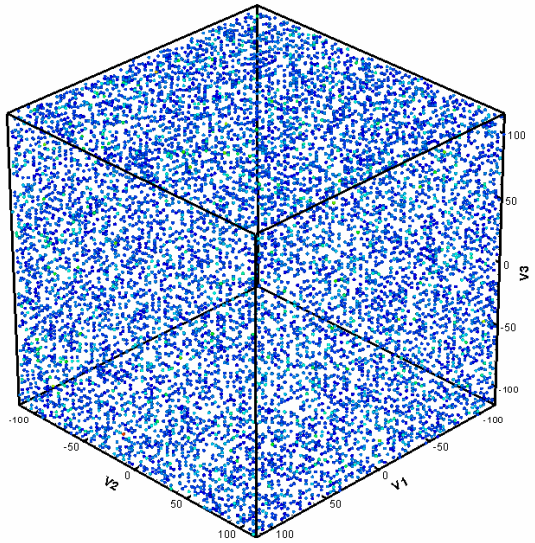

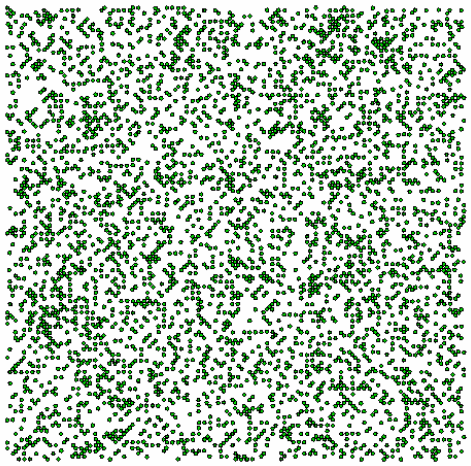

- Cr precipitates when fluctuations become larger than a critical size
- Precipitates are spherical

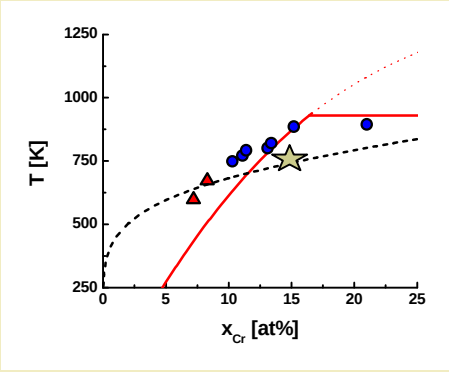

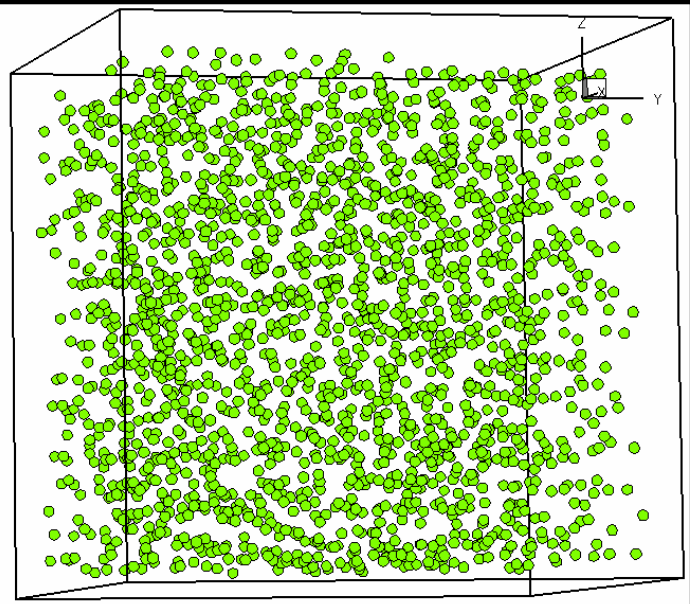

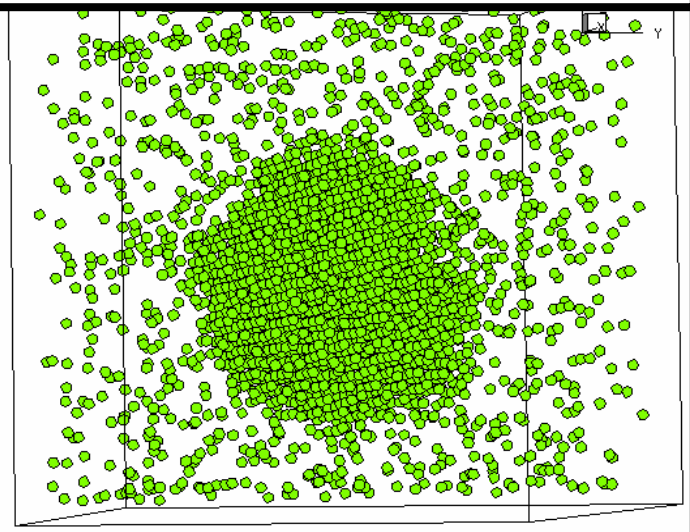

Spinodal decomposition
Homogeneous precipitation within the spinodal, at x~0.5

chemistry & materials science CMS

Spinodal decomposition happens by growth of small composition fluctuations (diffusion against the gradient of x), in regions of the phase diagram where $d^2G/dx^2 < 0$

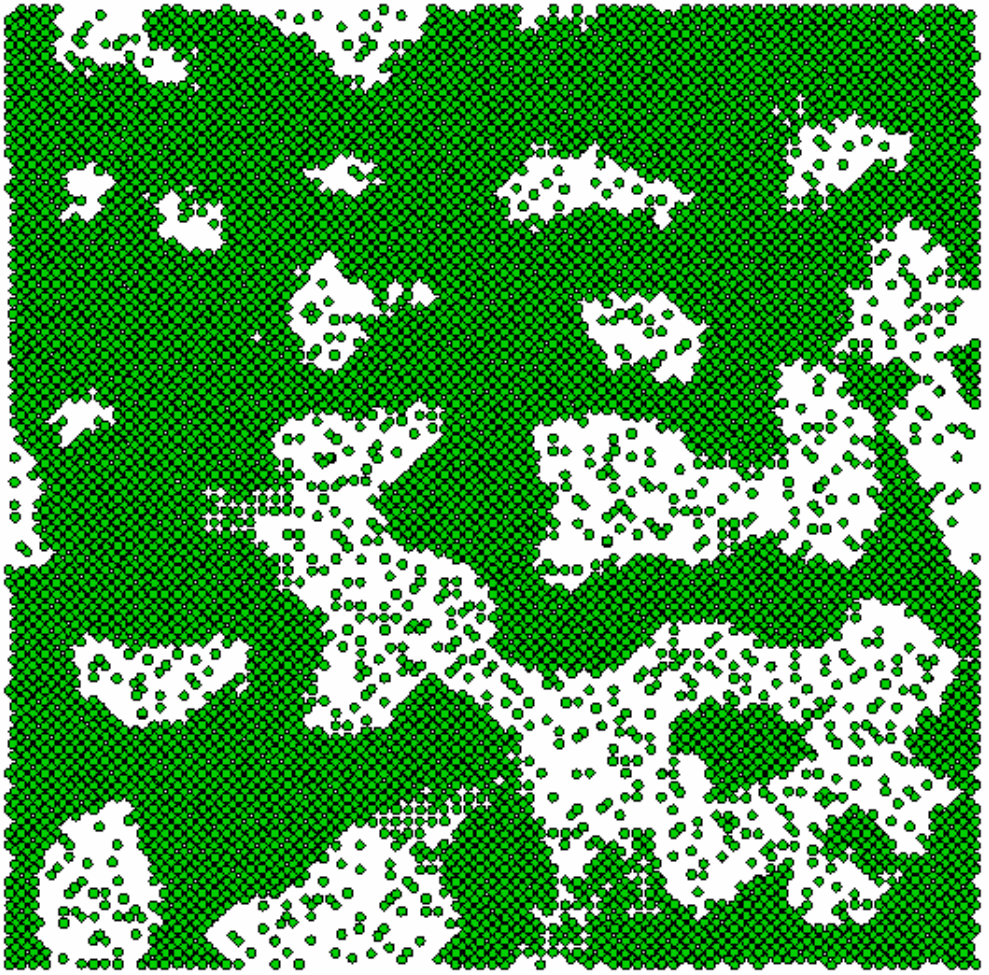

Cr precipitation in $Fe._5Cr._5$ at 750K

2-D slice of a 3D sample

Strategy to show you several HETEROGENEOUS precipitation examples: a nanophase Fe sample

chemistry & materials science CMS

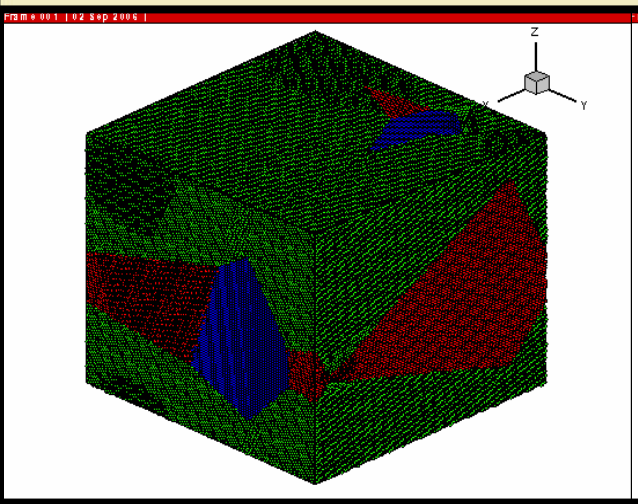

Nanophase sample
2 M atom, 15 grains

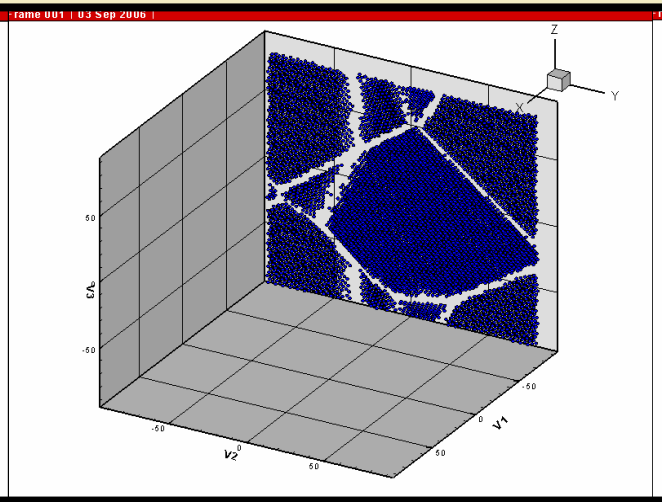

Slices showing perfect crystal bcc atoms

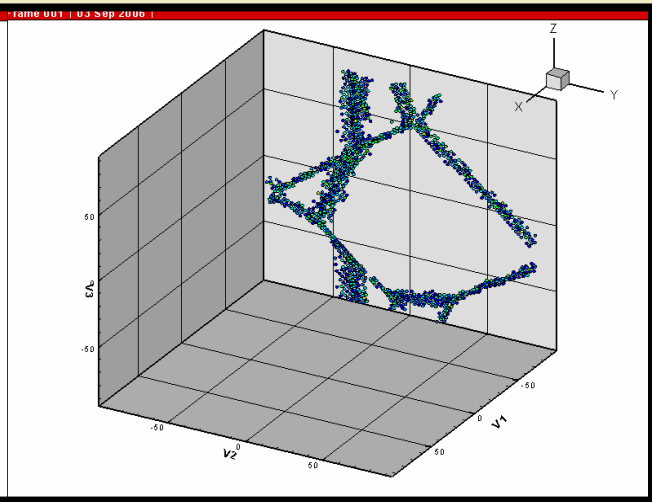

Slices showing brain boundary atoms

Heterogeneous precipitation in a bulk nanophase material

chemistry & materials science CMS

Excess Cr avoids precipitation at grain boundaries and triple junction

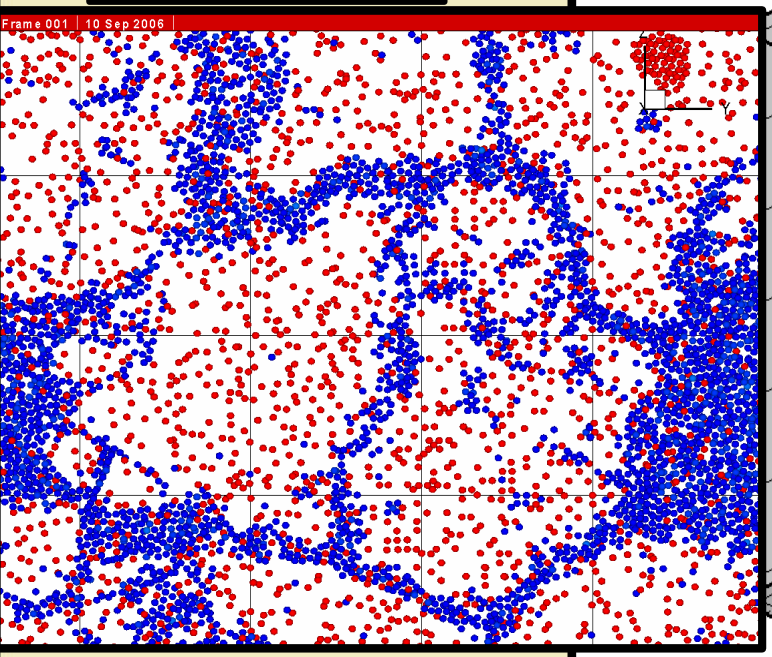

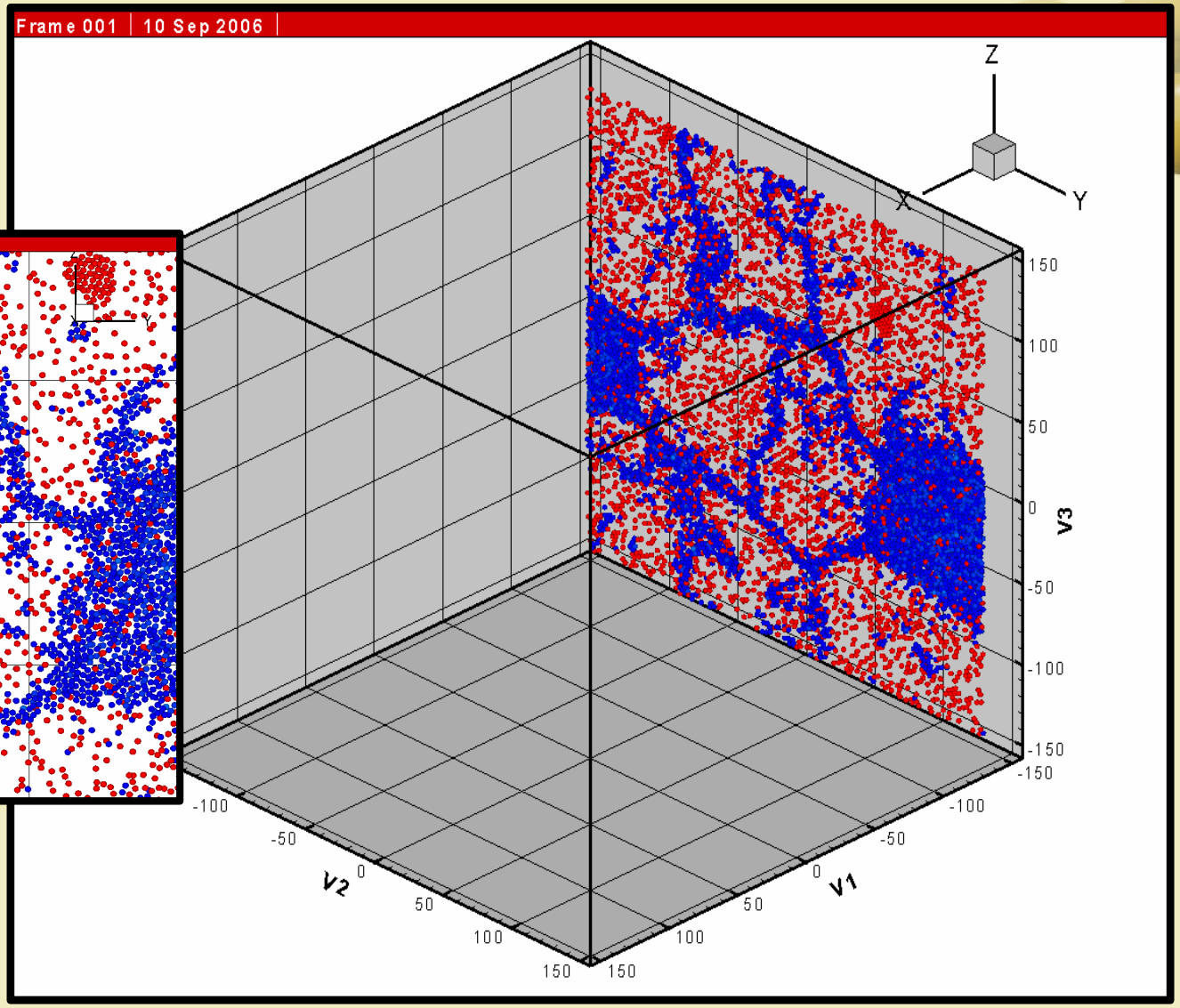

Cr precipitation in $Fe._{85}Cr._{15}$ at 750K

Heterogeneous precipitation in Fe-CR: Free surfaces, GB, TJ, cavities.

chemistry & materials science CMS

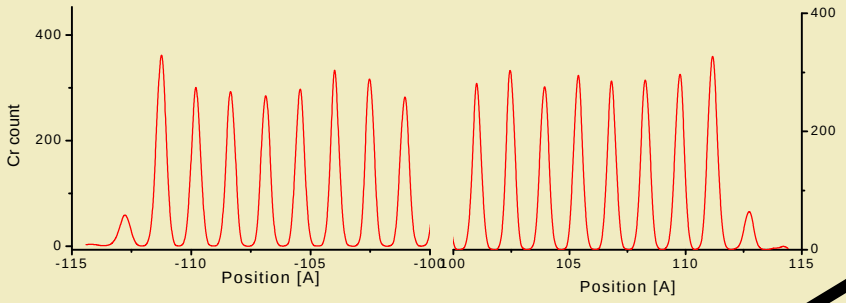

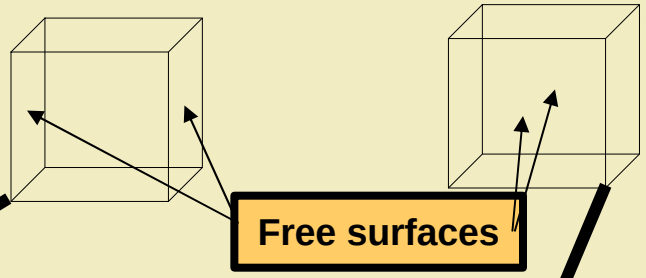

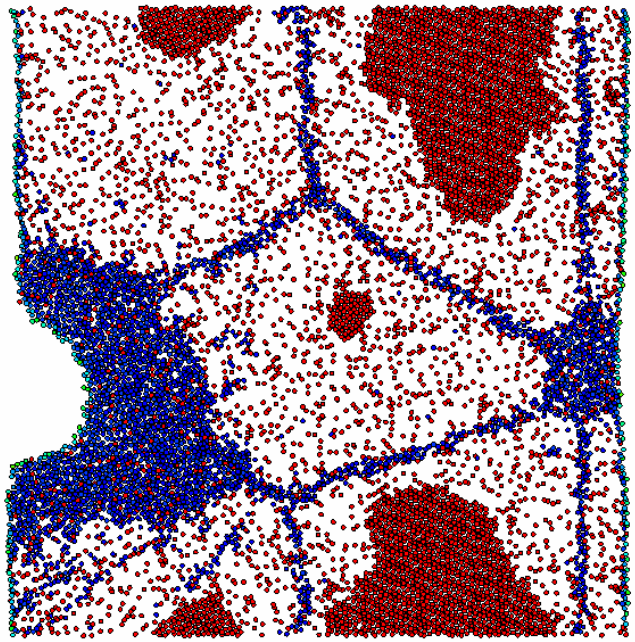

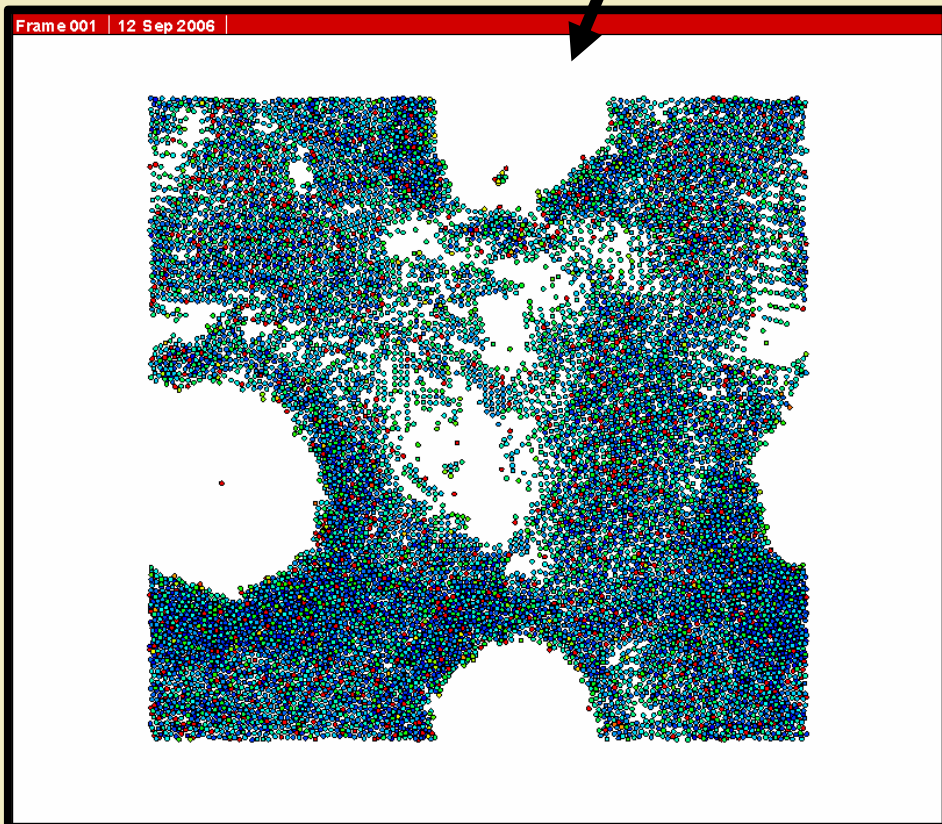

Heterogeneous precipitation in Fe-CR

High energy grain boundary

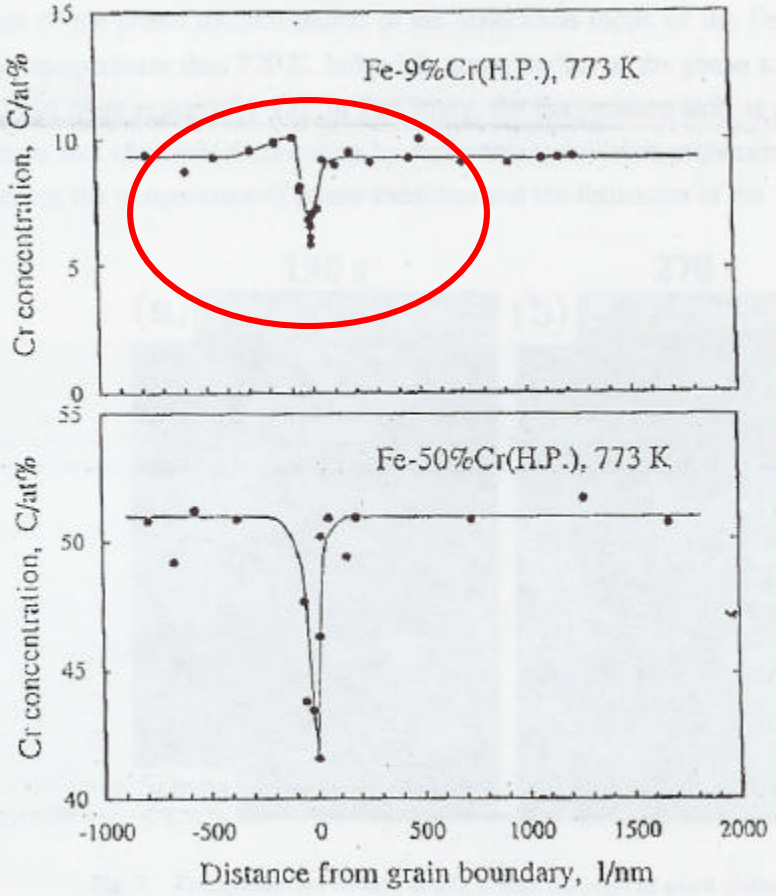

Fig. 6 Cr concentration as a function of the distance from grain boundary in (a) Fe-9Cr and (b) Fe-50Cr alloys irradiated at 773 K to 3 dpa.

E. Wakay et al. Jr. de Physique 5, C7-277 (1995)

Lath interface

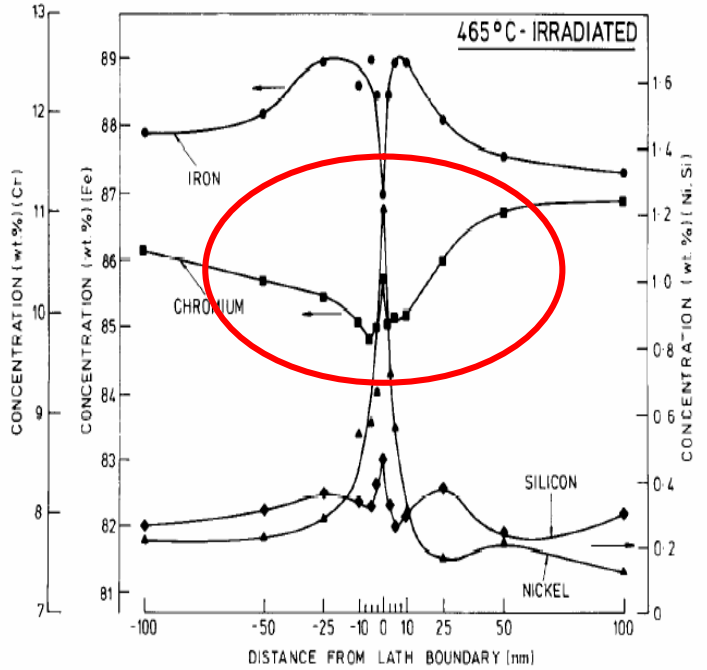

Fig. 6. Typical concentration gradients for Cr, Ni, Si an Fe on either side of a lath boundary after 465°C irradiation to 46 dpa.

Microstructural evolution in irradiated ferritic-martensitic steels: transitions to high dose behaviour

E.A. Little

Materials and Chemistry Division, Harwell Laboratory, Oxfordshire OX11 ORA, UK

ELSEVIER

Applied Surface Science 103 (1996) 495–502

applied surface science

Effect of the surface segregation of chromium on oxidation of high-purity Fe–Cr alloys at room temperature

S. Suzuki *, T. Kosaka, H. Inoue, M. Isshiki, Y. Waseda

Institute for Advanced Materials Processing, Tohoku University, Katahira, Sendai 980-77, Japan

Received 25 March 1996; accepted 22 May 1996

Abstract

Angle-resolved X-ray photoelectron spectroscopy (AR-XPS) has been used for investigating the effect of the surface segregation of chromium on oxide films formed on the surface of high-purity iron–13% and 25% chromium alloys at room temperature (298 K). The chromium segregation in the surface was confirmed by in-situ heating at 973 K under ultra high vacuum. The effective thickness of its segregated zone was evaluated to be less than 1 nm, from the relationship between the concentration of iron and chromium and the take-off angle in AR-XPS. The effective concentration of segregated chromium was estimated a few times as much as the bulk concentration. The surface with the chromium segregation was subsequently exposed to air, and an oxide film formed on the surface was also characterized. The oxide film formed on the surface with the chromium segregation was found to be thinner than the case without segregation. These results on the surface layer were consistent with spectral information of the chemical state denoted by Fe 2p and Cr 2p.

Keywords: High-purity; Iron–chromium alloys; Surface segregation; Oxidation; Angle-resolved X-ray photoelectron spectroscopy

PHYSICAL REVIEW B **68**, 233402 (2003)

Cr segregation at the Fe-Cr surface: A first-principles GGA investigation

W. T. Geng
Department of Chemistry, Pohang University of Science and Technology, Pohang 790-784, Korea
(Received 14 July 2003; published 9 December 2003)

The segregation of Cr at the Fe-Cr alloy surface is essential in the formation of a thin, corrosion-resistant oxide film. Recent angle-resolved x-ray photoelectron spectroscopy measurements indicated Cr segregation at a high temperature in vacuum. However, two independent *ab initio* density functional theory calculations within the local density approximation (LDA) suggested no segregation. We have calculated the segregation energy for Cr at the Fe-Cr(001) surface using the all-electron full-potential linearized augmented plane wave method within the generalized gradient approximation (GGA). Our GGA results support the previous LDA investigations. The disagreement between experiment and theory remains unresolved.

DOI: 10.1103/PhysRevB.68.233402 PACS number(s): 68.35.Dv, 81.05.Bx

Conclusions

- Experiments and computational modeling are helping in the design of new materials with enhanced performance in extreme environments
- National/Regional R&D efforts are converging into materials with nanoscale features that address the 3 main concerns:
  - Radiation resistance
  - Corrosion resistance
  - High strength at high T
- Research effort is supported by Fusion, Gen IV,

Connection between the Micro and Meso-scales

Jaime Marian[*], Brian D. Wirth[*], G. R. Odette[†], Robin Schäublin[‡], E. Martinez[*], Tom Arsenlis[*] and J. M. Perlado[§]

[*] *Lawrence Livermore National Laboratory, USA*

[†] *University of California Santa Barbara, USA*

[‡] *CRPP-EPFL, Switzerland*

[§] *Universidad Politécnica de Madrid, Spain*

Formation and Growth of ⟨100⟩ Dislocation Loops in Ferritic Materials

BACKGROUND

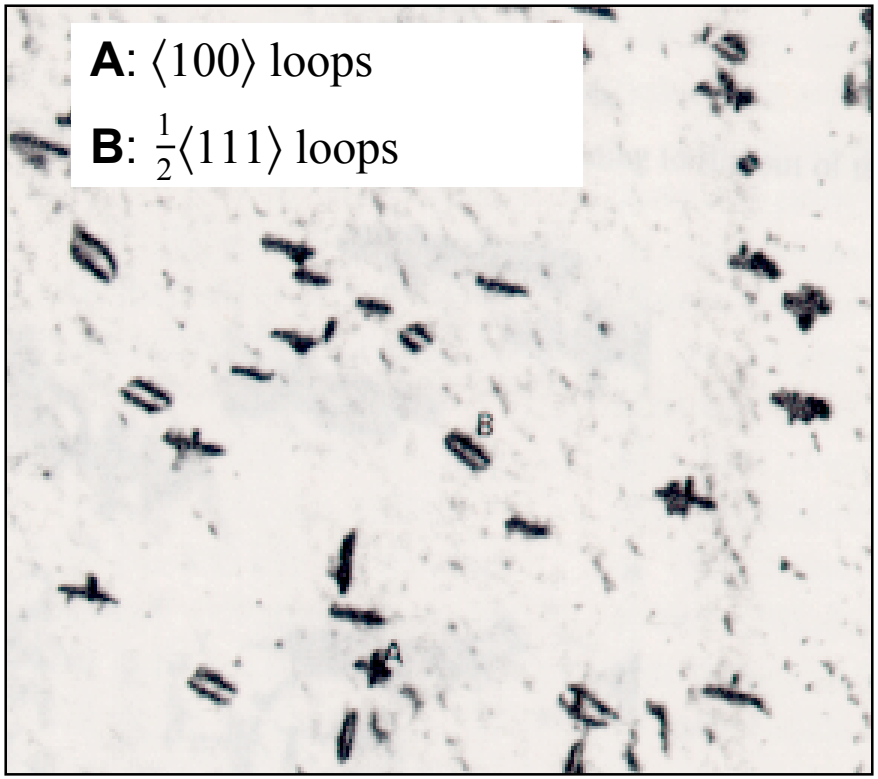

Dislocation loops in Fe irradiated at 465˚C and ~10^{-4} dpa/s to 0.5 dpa

1. Experimental studies indicate that large, interstitial-type, $\frac{1}{2}\langle 111\rangle$ and $\langle 100\rangle$ dislocation loops form in irradiated Fe-based model alloys.

2. To date, atomistic simulations only show the formation of $\frac{1}{2}\langle 111\rangle$ clusters during displacement cascades.

3. A mechanism consistent with **atomistic simulations**, **continuum elasticity**, **dislocation theory** and **experimental observations** has been lacking for the last three decades

Investigate mechanisms of formation of $\langle 100\rangle$ loops from $\frac{1}{2}\langle 111\rangle$ clusters and ensure that simulated loops reproduce the experimental observations

Objectives and method

- Use atomistic simulations to:
  - Identify the underlying mechanisms that give rise to ⟨100⟩ loops in ferritic systems
  - Study the mobility and thermal stability of large ⟨100⟩ loops for a variety of sizes and shapes
  - Investigate the growth of nucleated-⟨100⟩ loops to observable sizes
- Compare MD-simulated self-interstitial dislocation loops with experimental TEM observations using TEM image simulations

Self-interstitial clusters: $\frac{1}{2}\langle 111\rangle$ loops

- **Stability of <111> self-interstitial atom (SIA) clusters revealed by recent atomistic modeling (*Finnis-Sinclair and EAM-type interatomic potentials*)**

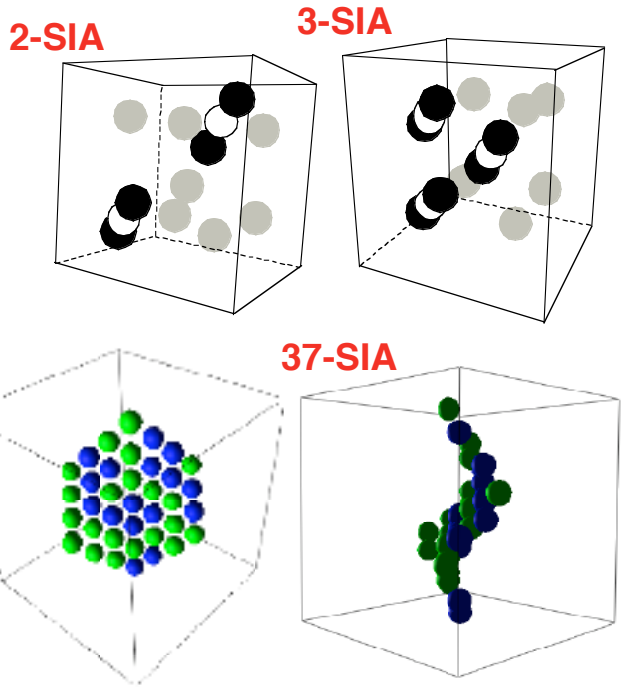

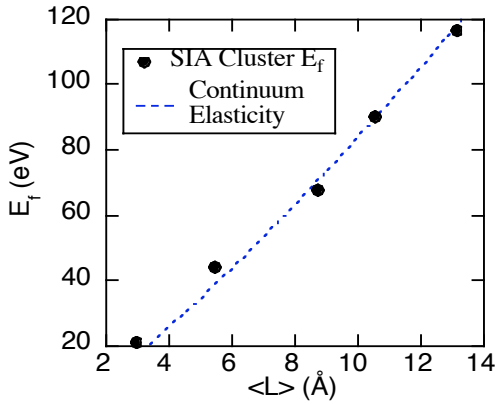

MD simulations reveal rapid (E_m < 0.1 eV) 1-D migration

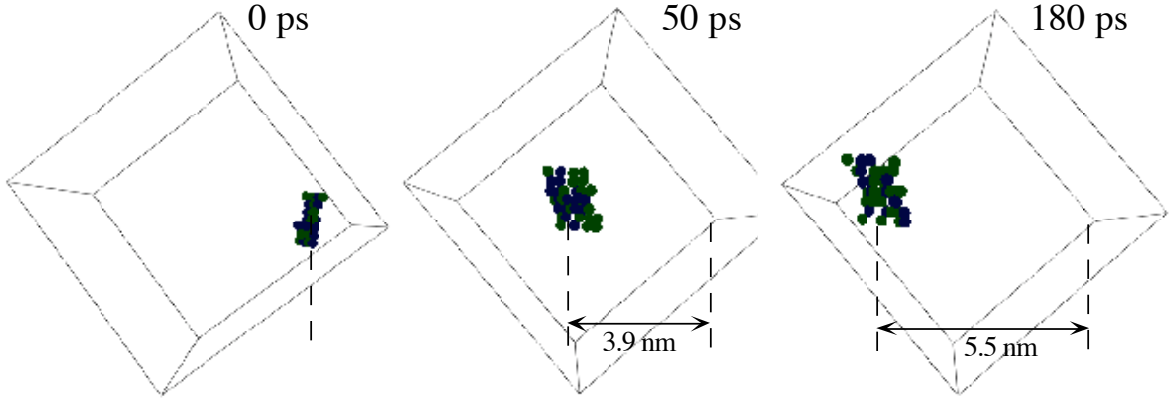

- **Form highly kinked, proto-$\frac{1}{2}\langle 111\rangle$ dislocation loops directly in cascades**
- **Migrate in 1-dimension with high mobility**

Loop formation energies

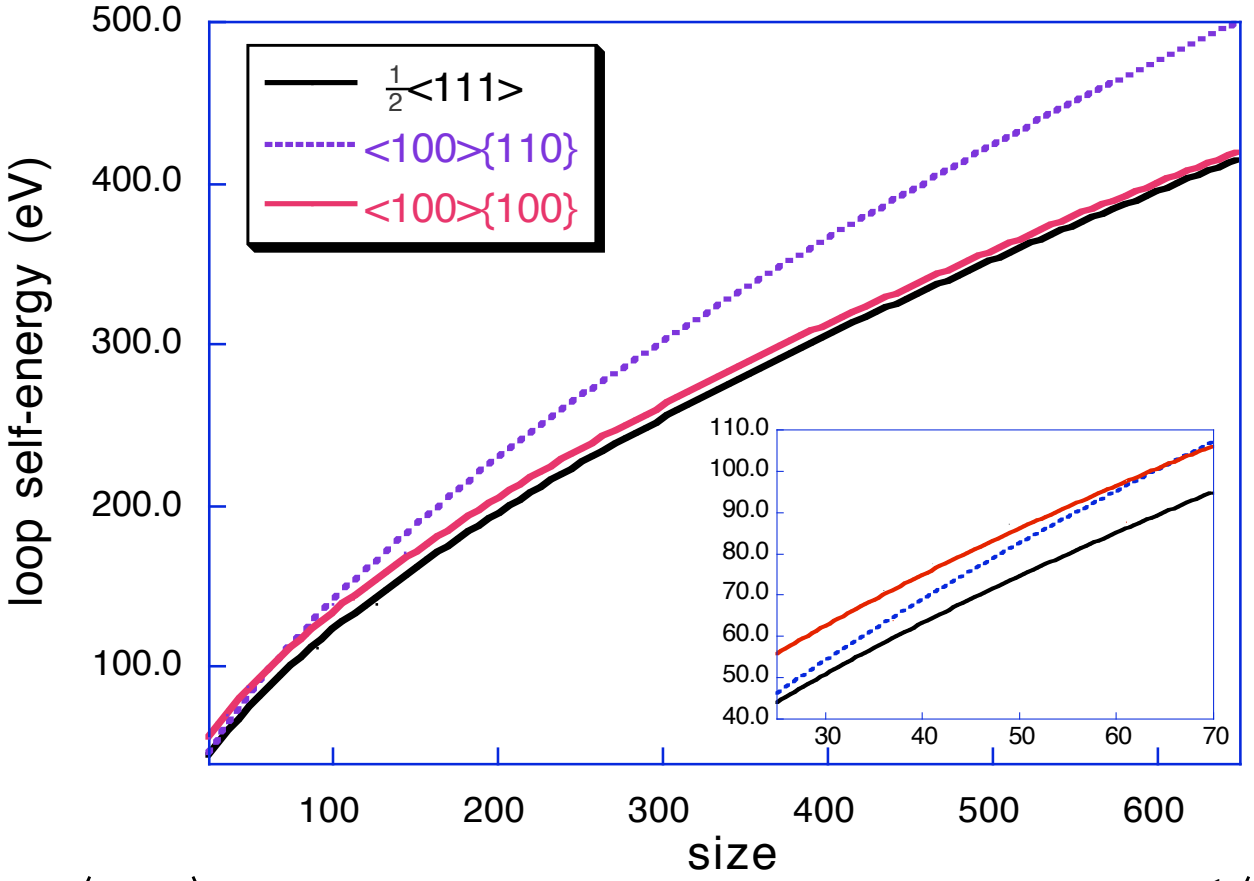

The minimum energy configuration for ⟨100⟩ loops corresponds to *magic-shape* loops in each habit plane: rhombi in {110} planes and squares in {100} planes

- ⟨100⟩ are always metastable with respect to $\frac{1}{2}\langle 111\rangle$ loops.
- Initially, ⟨100⟩ loops form in {110} planes, then rotate to {100} planes
- Computed core energies of 0.4 and 1.1 eV/Å, respectively

Nucleation of ⟨100⟩ junctions

- ⟨100⟩-type segments are seen in dislocation networks in *bcc* metals

$$\tfrac{1}{2}[111] + \tfrac{1}{2}[1\bar{1}\bar{1}] \rightarrow [100]$$

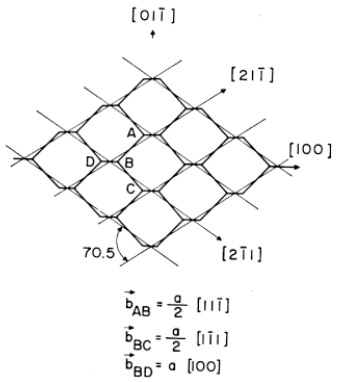

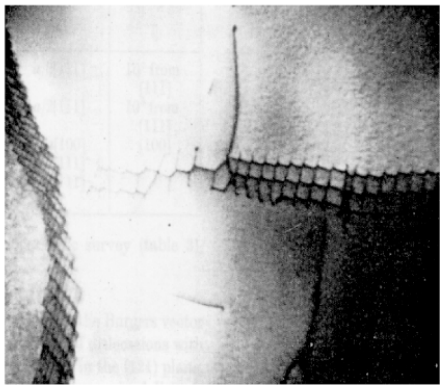

- ⟨100⟩ junctions are formed by direct interaction of cascade-created $\frac{1}{2}\langle 111\rangle$ clusters in ferritic materials:

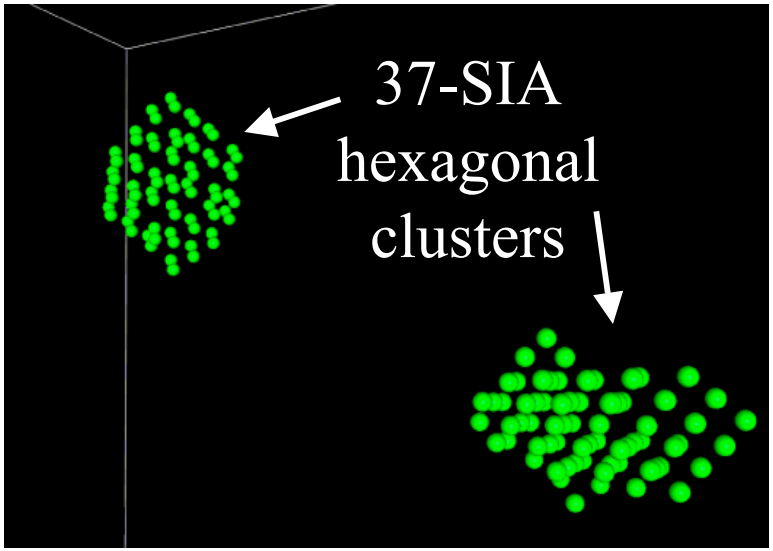

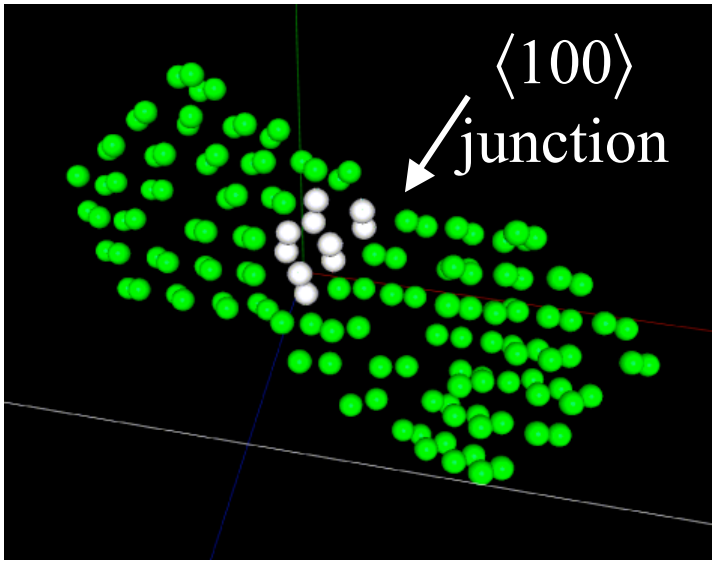

$\frac{1}{2}[111]$ $\frac{1}{2}[1\bar{1}\bar{1}] \rightarrow$ [100]

Nucleation of ⟨100⟩ junctions

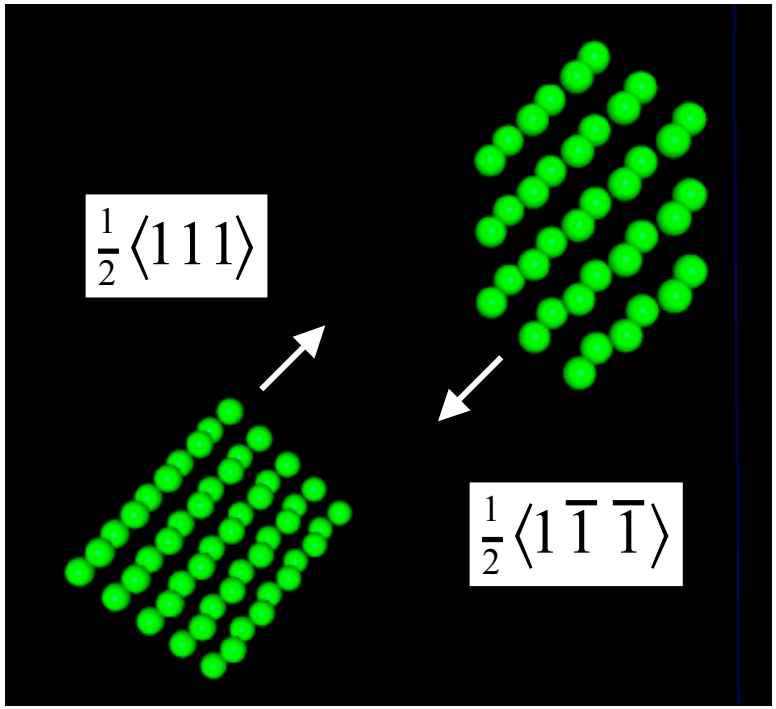

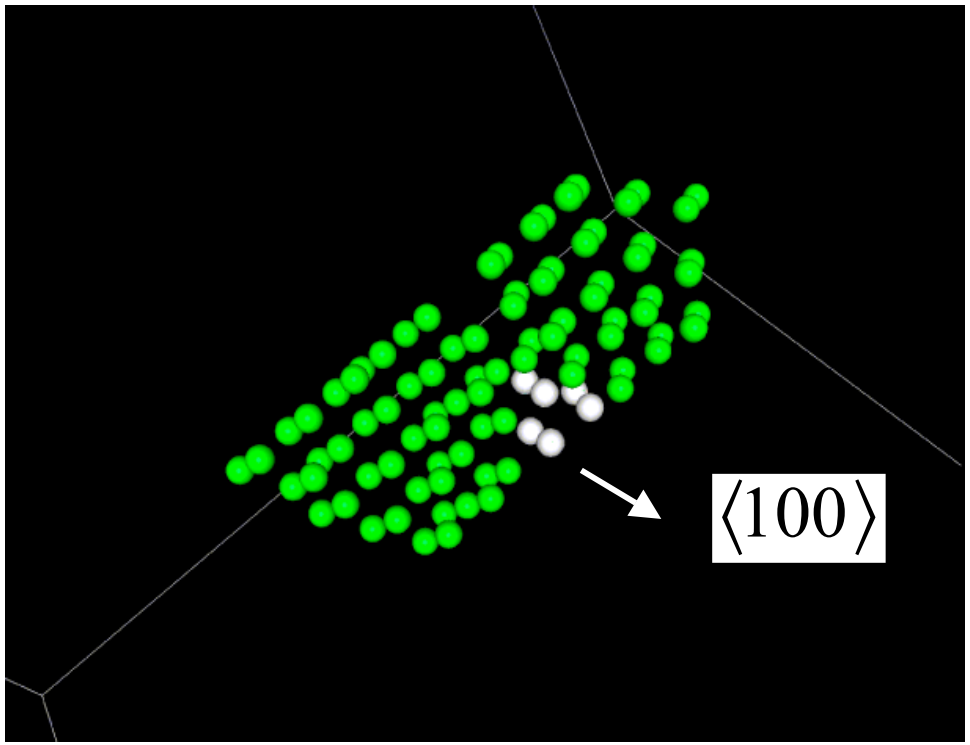

19-SIA ⟨111⟩-loop (hexagonal) interacts with 25-SIA ⟨111⟩-loop (rhombic)

➪ Critical ⟨111⟩-loop size for ⟨100⟩-junction formation ≥ ~20

Nucleation and growth of ⟨100⟩ junctions

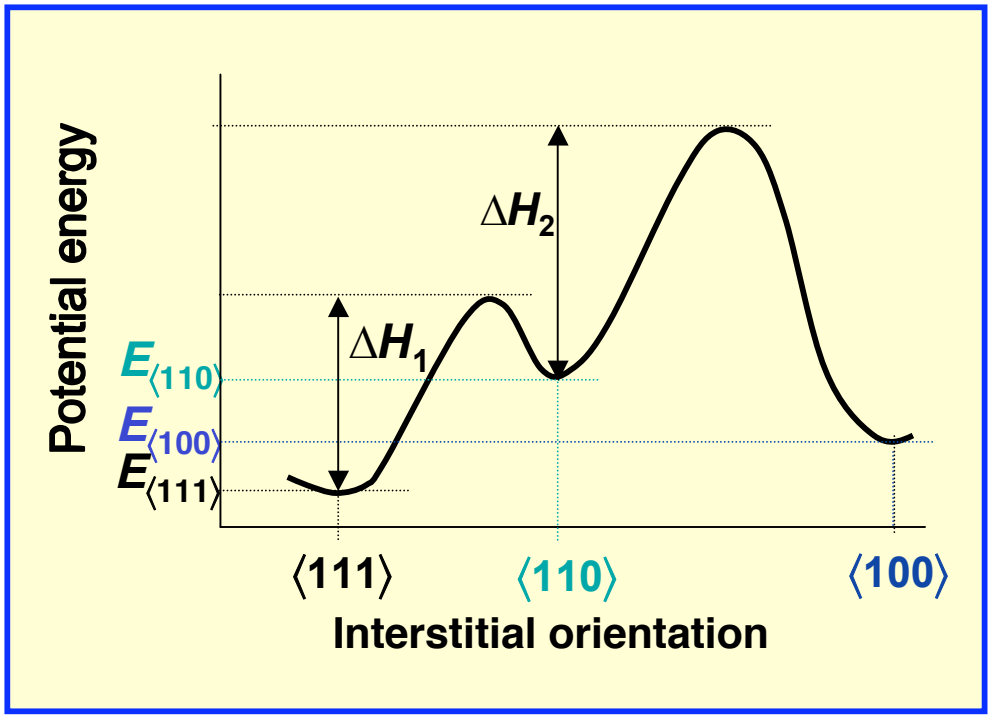

- The propagation of metastable ⟨100⟩ junctions is governed by this energy landscape
- At very high temperatures the junction dissolves into ⟨111⟩ interstitials

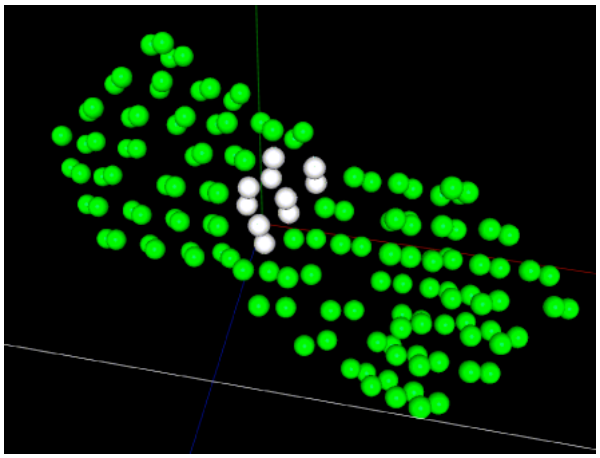

propagation

dissolution

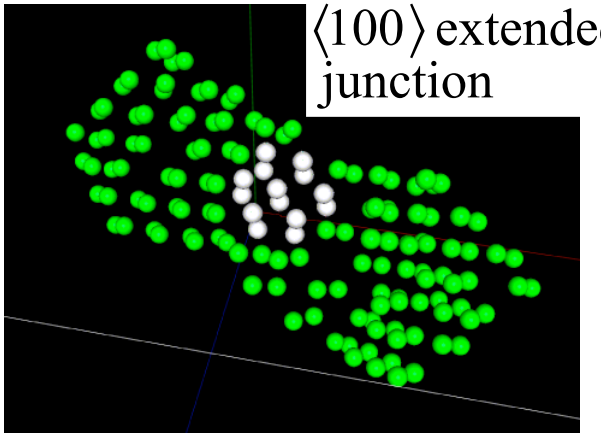

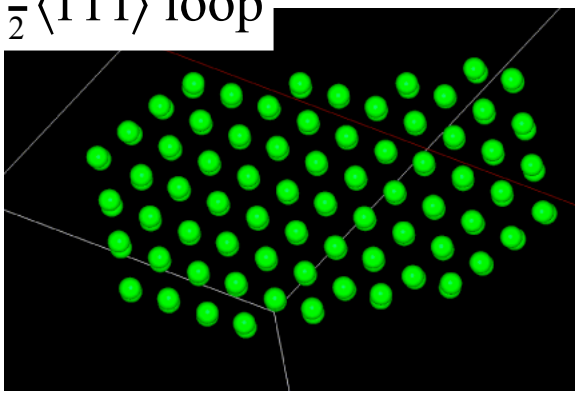

Growth mechanisms of ⟨100⟩ loops

- Despite being metastable with respect to $\frac{1}{2}\langle 111\rangle$ loops, ⟨100⟩ loops grow by absorption of smaller $\frac{1}{2}\langle 111\rangle$ loops

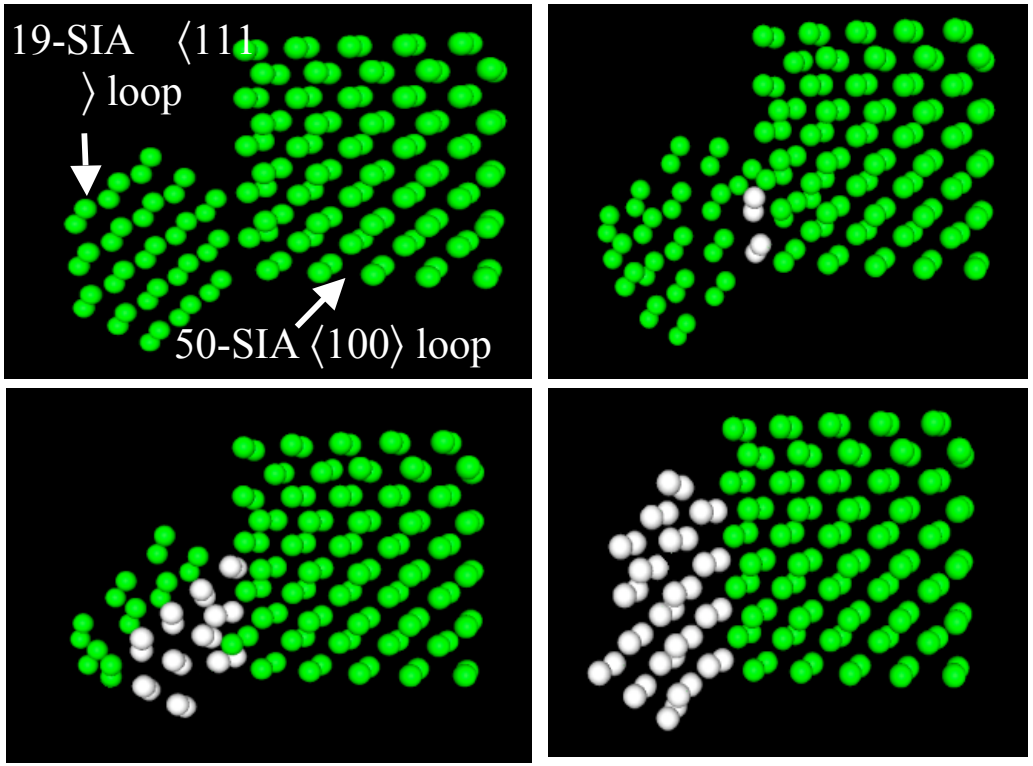

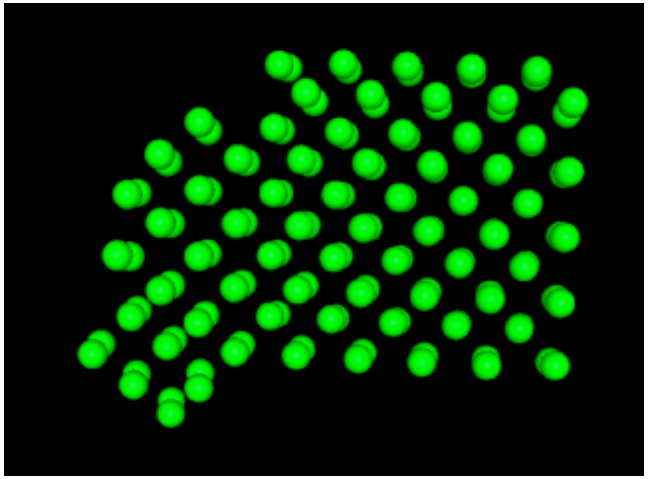

$$\langle 100\rangle + 2\,\tfrac{1}{2}\langle 111\rangle \rightarrow \rightarrow \langle 211\rangle \rightarrow \langle 100\rangle$$

- Atoms shown in white, are rotating to join the ⟨100⟩ loop according to the above reaction

TEM image calculation from atomistic computer simulation: shape effect

Weak-beam **g**=(200), **g**(4.1**g**), CTEM simulated images and [110] view of the atomistic structure

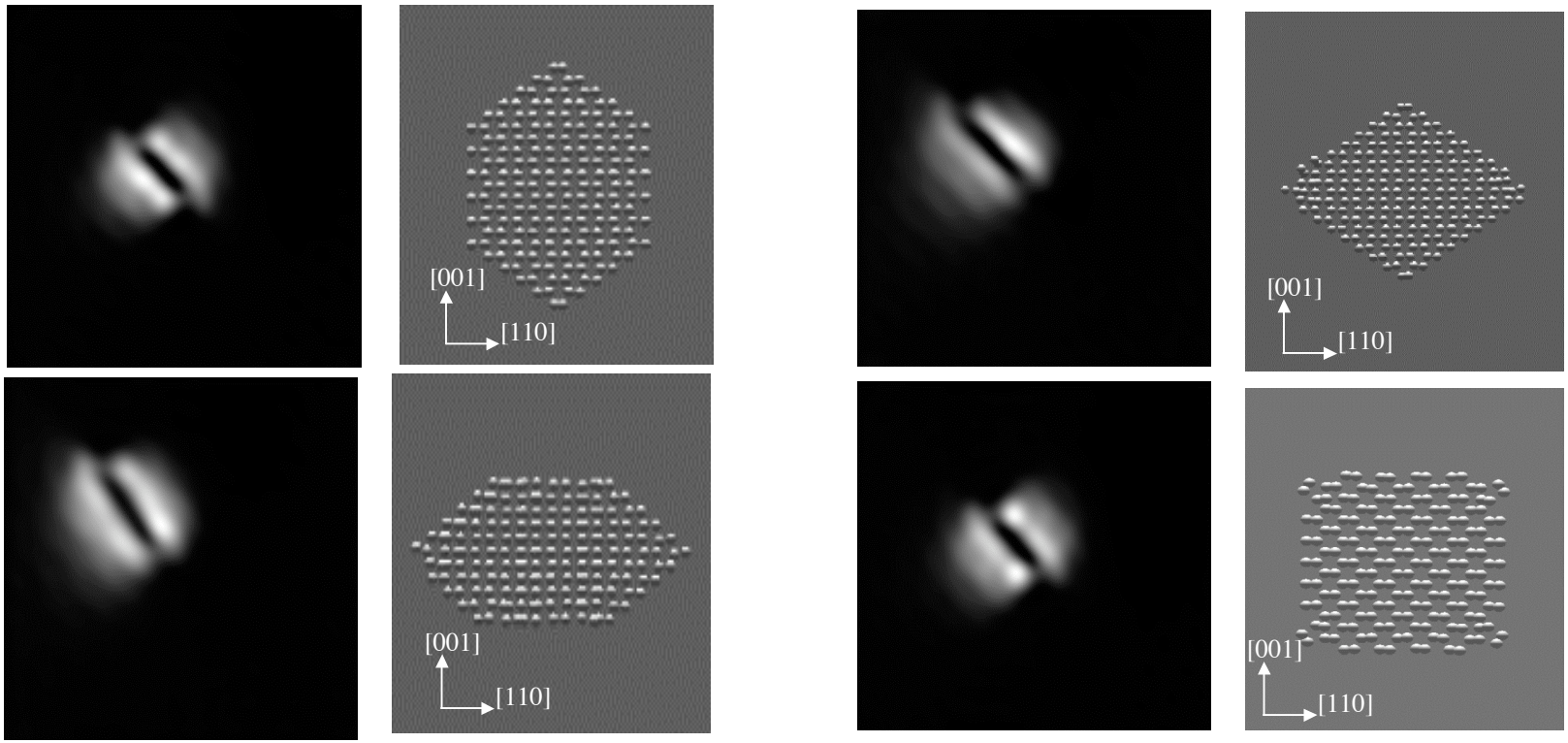

Atomistic simulation - experiment comparison of ⟨100⟩ dislocation loops

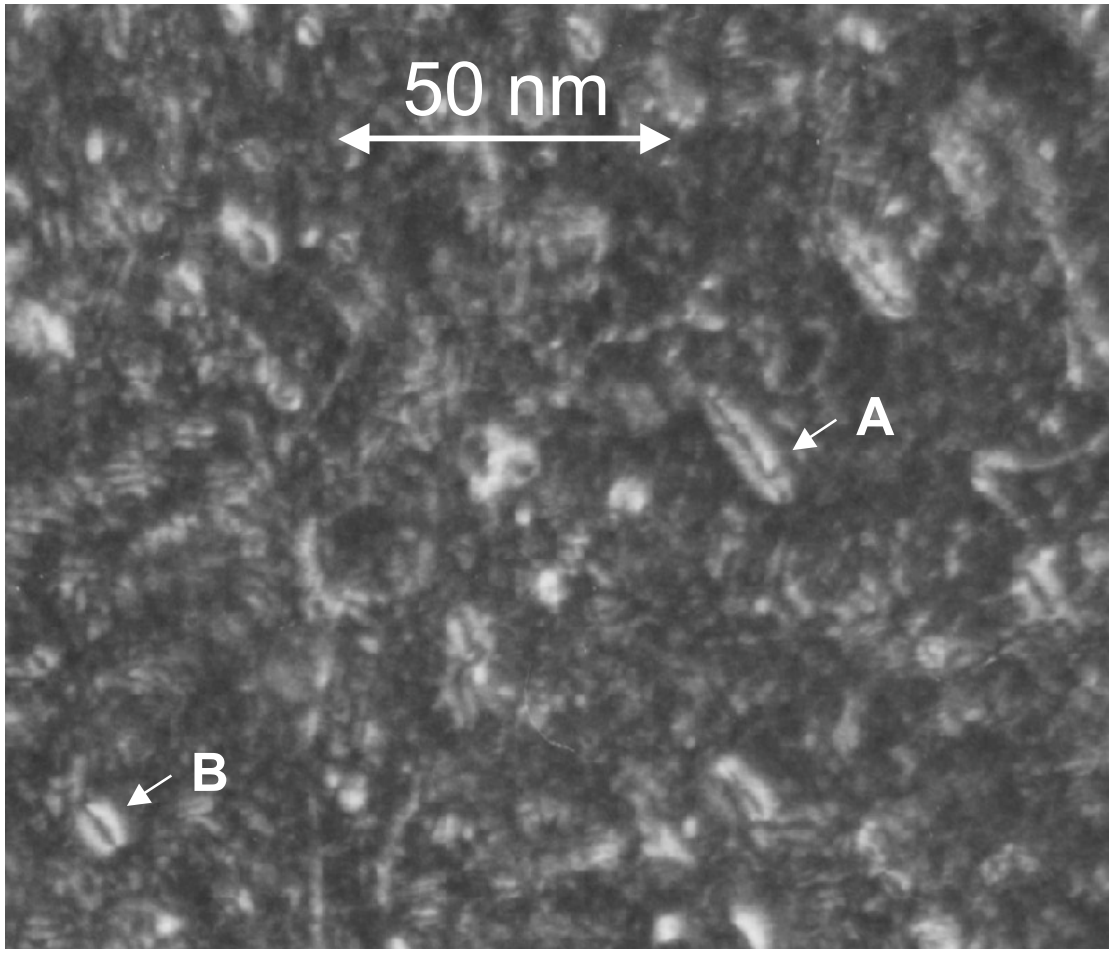

Good agreement between experimental images (irradiated tempered martensitic steel) of edge-type ⟨100⟩ loops and computer-simulated images

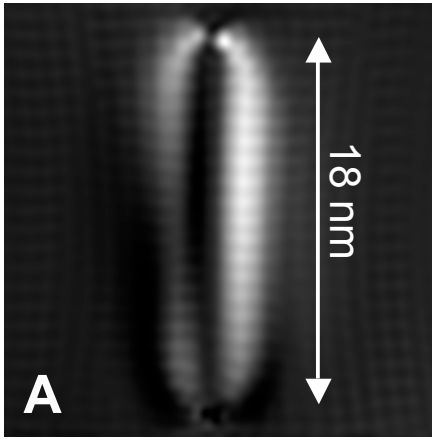

937-SIA rectangular loop, habit plane (100)

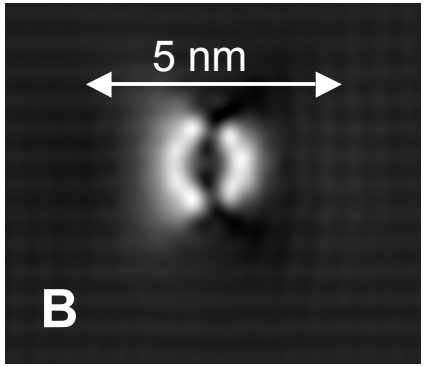

61-SIA hexagonal loop, habit plane (100)

Effect of Cu Solute Atoms on Interstitial Cluster Migration

Objectives and method

- Study the physics behind solute interactions with radiation-produced defects
- To derive simple expressions that allow us to extrapolate the value of the migration energies and pre-exponential factors of SIA clusters as a function of cluster size in pure Fe and dilute (~1.0 %) Fe-Cu alloys
- Calculation of diffusivities:

$$D_n = \frac{1}{m}\sum_{i=1}^{m}\frac{\langle R^2 \rangle}{2\, n_d\, t_i}$$

$$D_n \propto \langle v(t_0)\cdot v(t_0+t)\rangle$$

Single self-interstitial diffusion in FeCu alloys

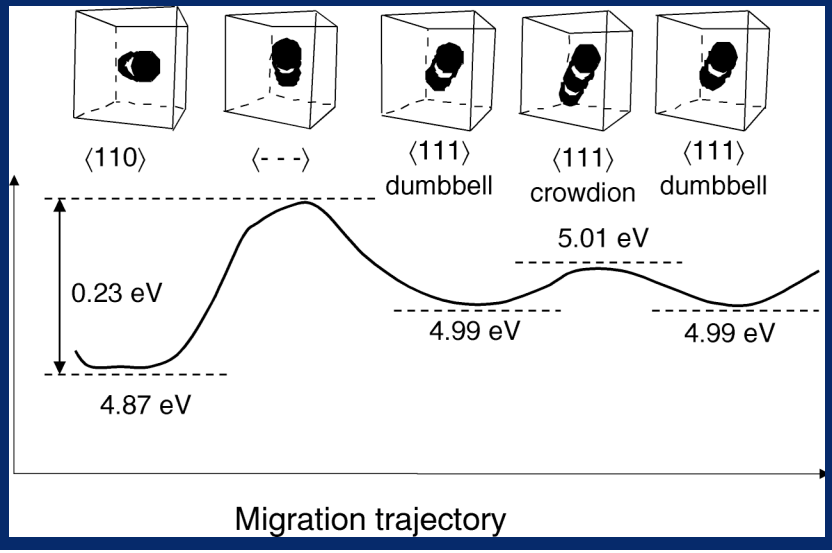

e_b= 0.02 eV

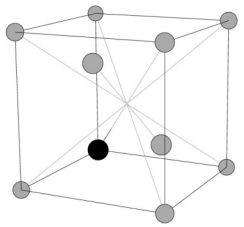

e_b= 0.01 eV

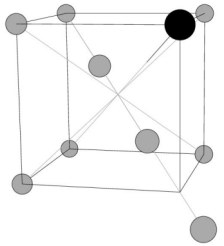

e_b= –0.04 eV

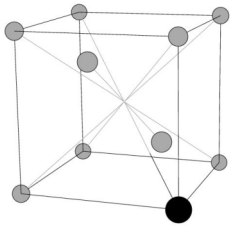

e_b= –0.08 eV

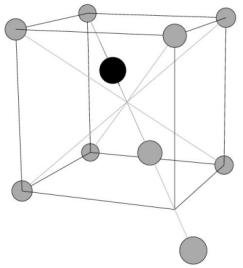

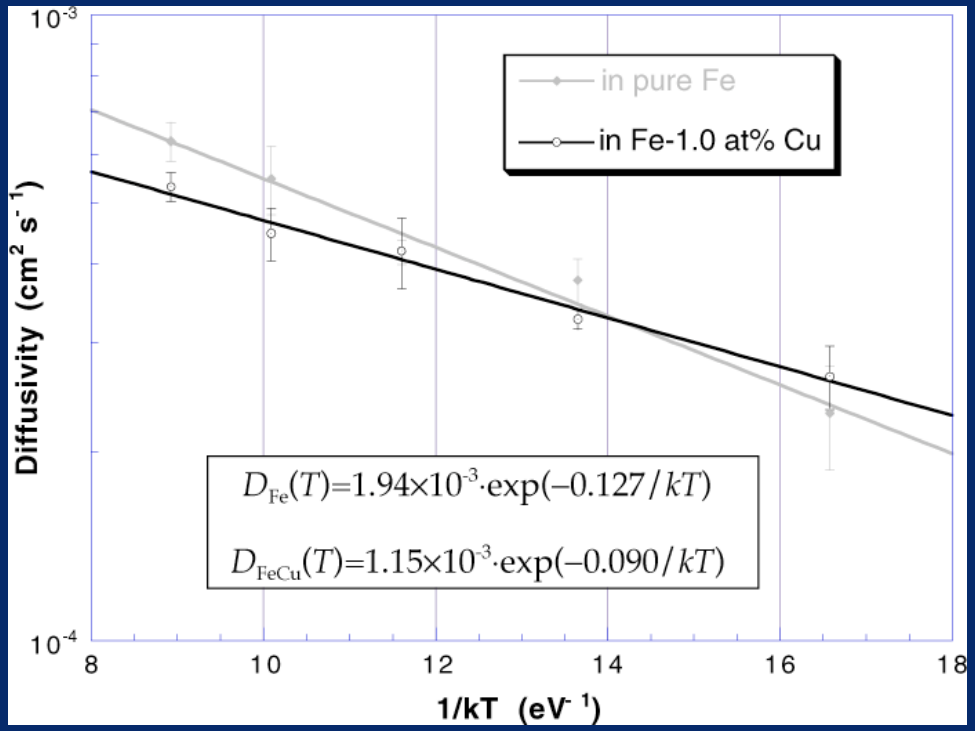

Cu solute atoms have a notable effect on self-interstitial diffusion

Cluster Diffusivities

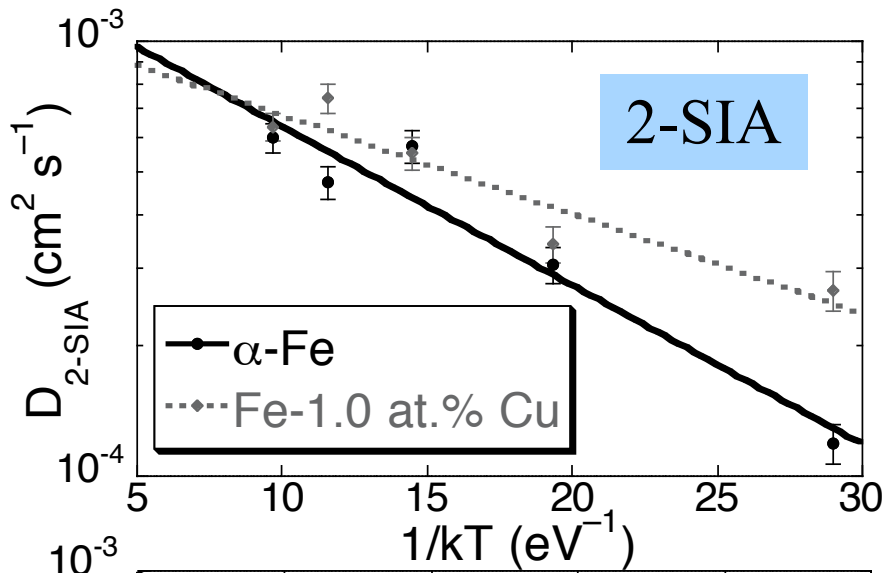

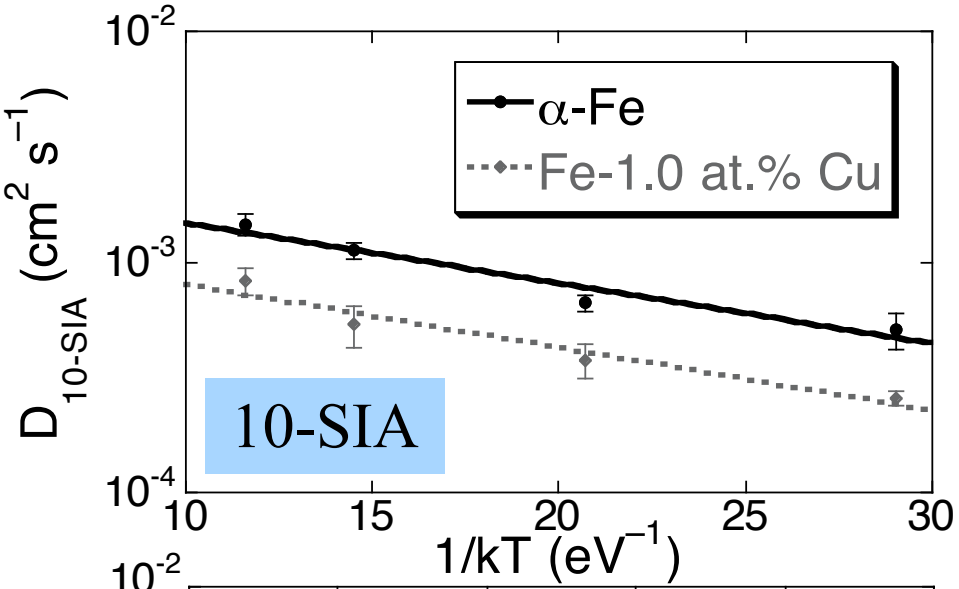

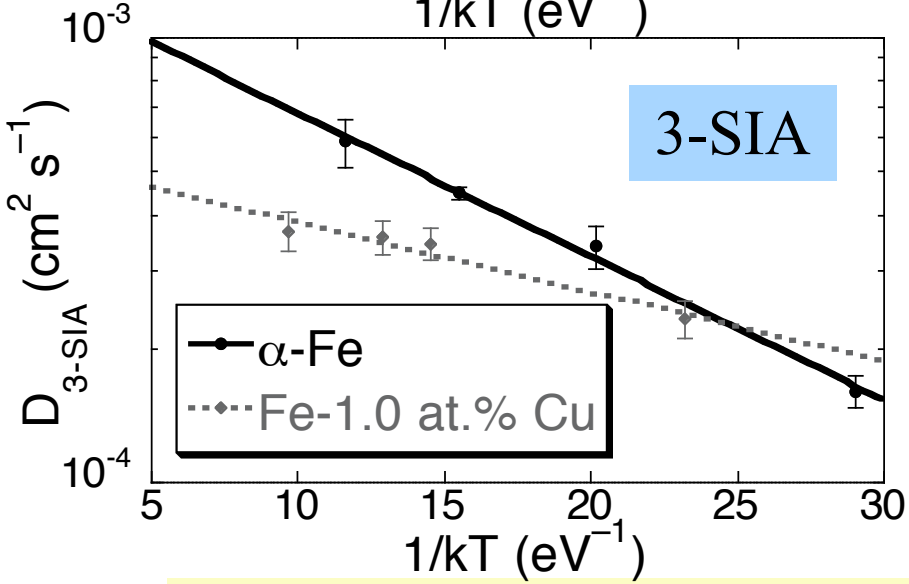

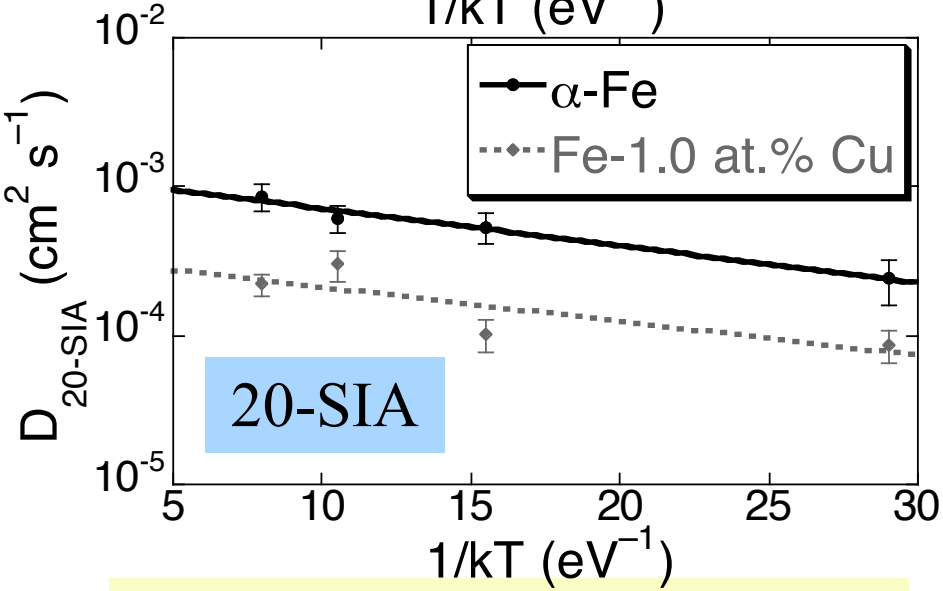

- **Small 3D clusters (n=1,2,3): change in E_m and D_0**
- **Larger 1D clusters (n>3): no change in E_m , decrease in D_0**

Migration energies

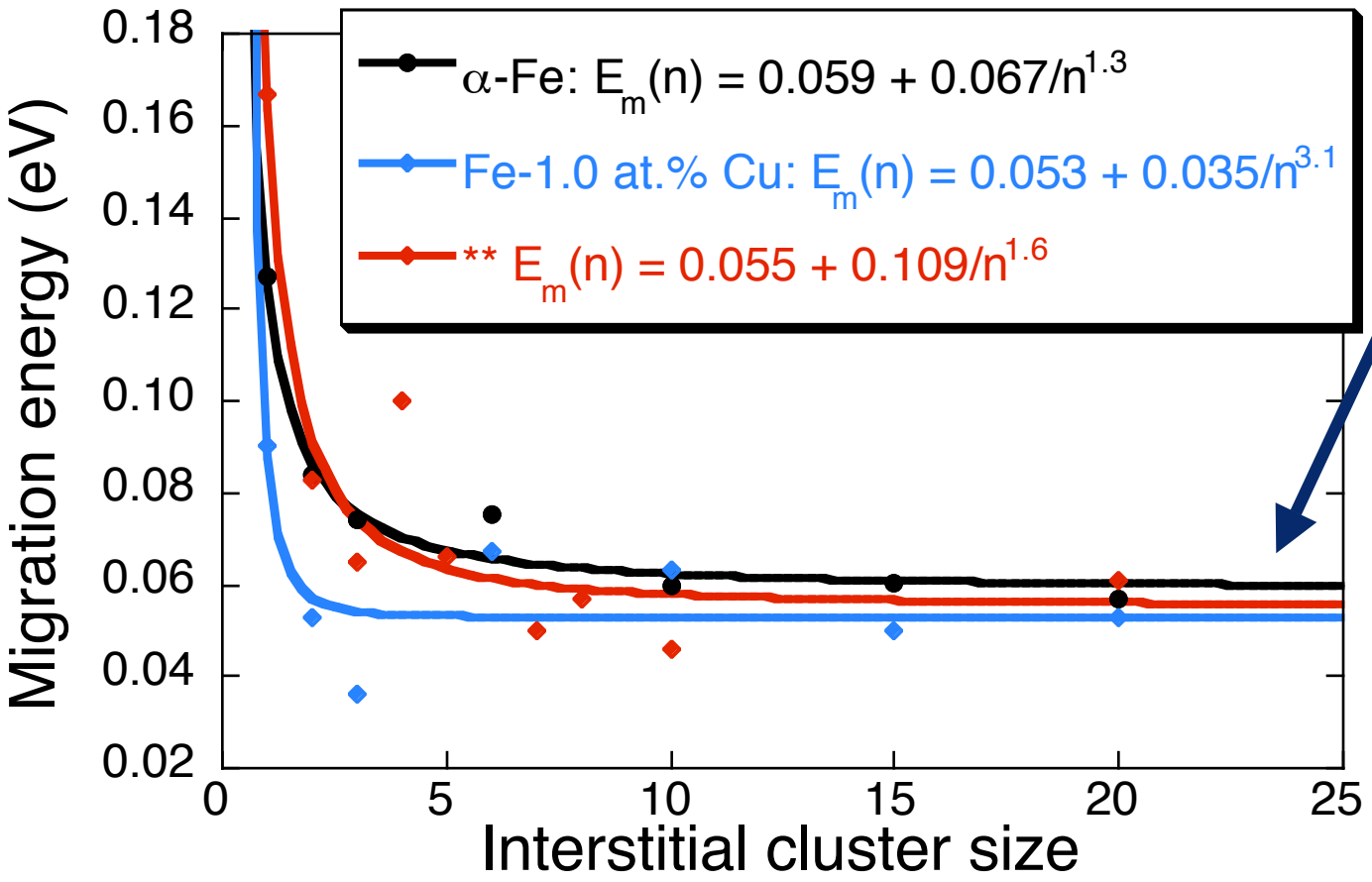

Saturation value related to:

A) activation energy for the ⟨111⟩ step

B) double kink nucleation energy in edge dislocation segments

Migration energies saturate for $n>6$. FeCu shows a smaller dependence on cluster size than pure Fe. The asymptotic value is between 0.05 and 0.06 eV.

** N. Soneda and T. Diaz de la Rubia, *Phil. Mag.* A **81** (2001) 331

Diffusion prefactors

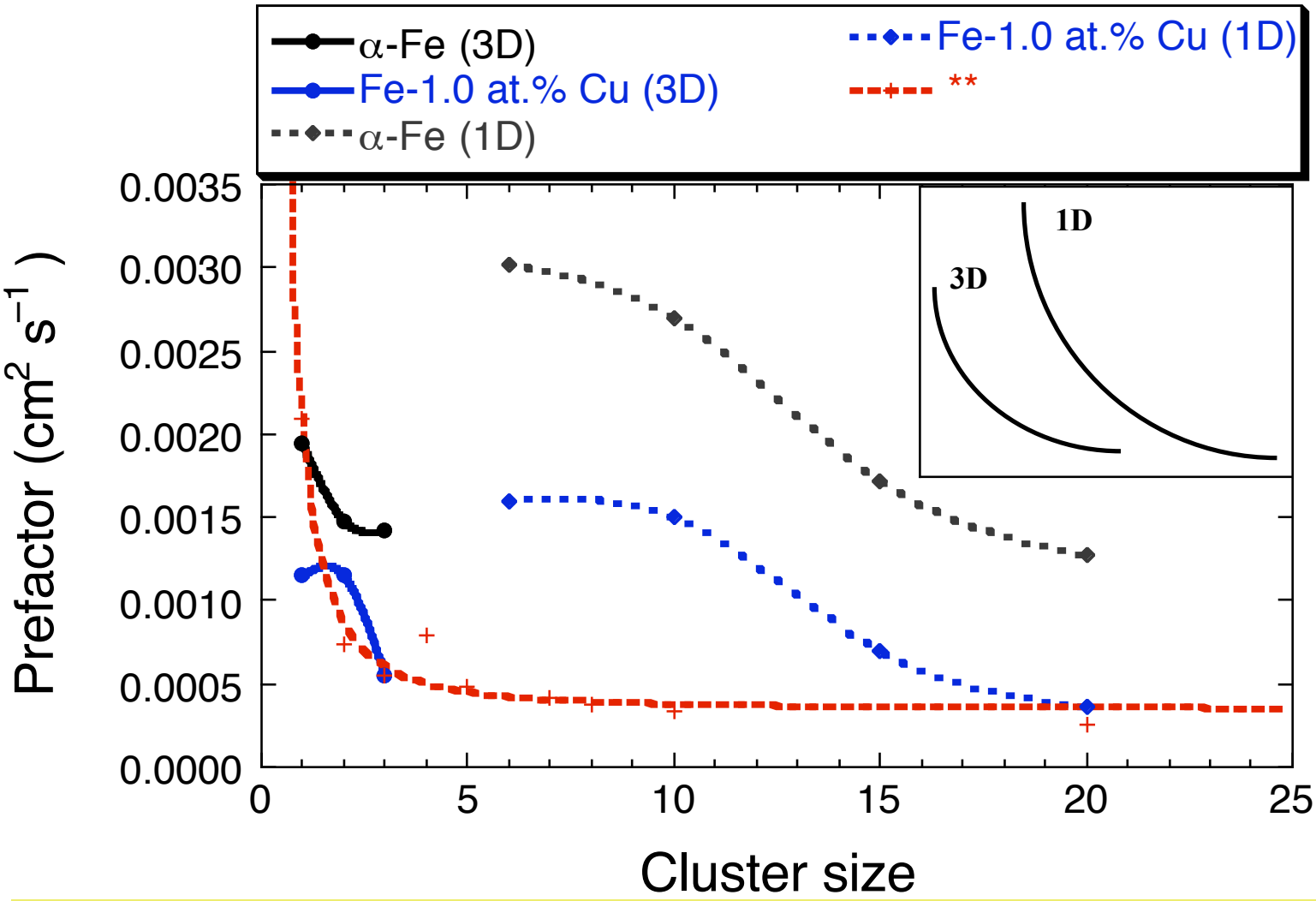

Above n~3, migration dimensionality , n_d, changes from 3 to 1 accounting for the sharp increase observed in the curves. For n>3 (n_d=1), pre-exponential factors decrease monotonically with cluster size.

Extrapolation laws

- Migration energies
  - $E_m(n) = a + b/n^c$, a is the asymptotic value: kink nucleation energy in edge dislocation-type defects (also related to the ⟨111⟩ migration step for SIA clusters in b.c.c. metals)

  Pure Fe: $E_m(n) = 0.06 + 0.07\ n^{-1.3}$

  Fe-1.0 at.% Cu: $E_m(n) = 0.05 + 0.04\ n^{-3.1}$
- Prefactors
  - $D_0(n) = a \cdot n^{-S/2}$, S=2 for a purely random diffusion
    S=1 for a force-biased (mechanical) motion
  - Diffusion prefactors do not saturate with cluster size as the loop grows into a *sessile* network dislocation

  Pure Fe: $D_0(n) = 8.98\times10^{-3}\ \ n^{-0.61}$

  Fe-1.0 at.% Cu: $D_0(n) = 5.07\times10^{-3}\ \ n^{-0.74}$

Dislocation - obstacle interactions in metals

Structural materials in nuclear (irradiation) environments are subject to mechanical property changes

Irradiation produces hardening

- **Irradiation hardening is measured by the yield stress increase**

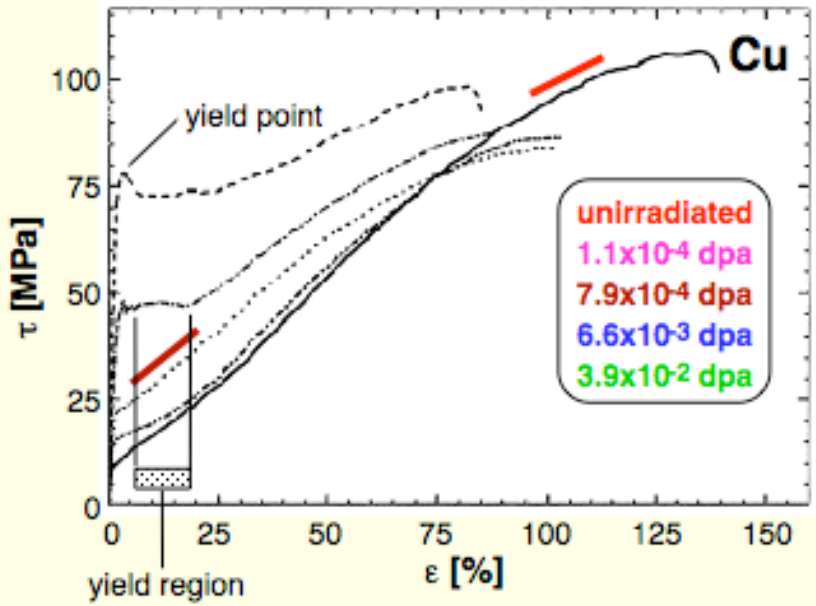

Stress-strain relations of irradiated Cu at 300K (from: M. Victoria et al. 2001)

TEM image of irradiation defects in Cu

- **The yield stress increase is due to the formation of very stable stacking-fault tetrahedra (SFT) which impede dislocation motion**

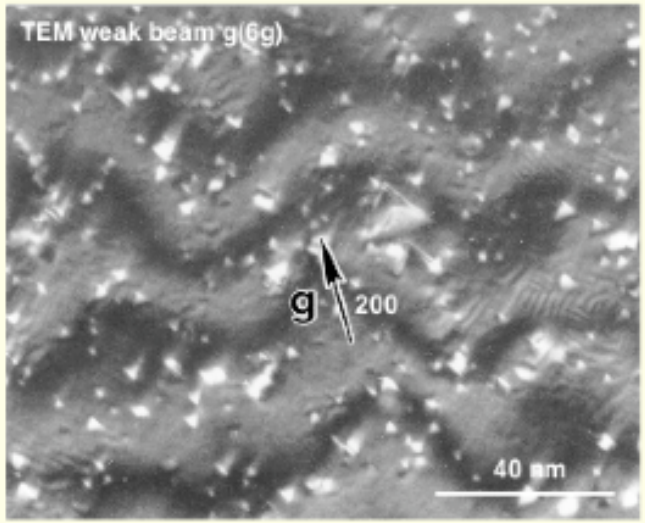

SFTs formed in Cu at 4.3×10-2 dpa (from: Yao et al. 2004)

Plasticity in fcc metals is governed by partial dislocation interactions

Consideration of partials can be done using simple geometrical rules

$$\sum_i \mathbf{b}_i = 0$$

$$\sum_i \gamma\mathbf{n}_i = 0$$

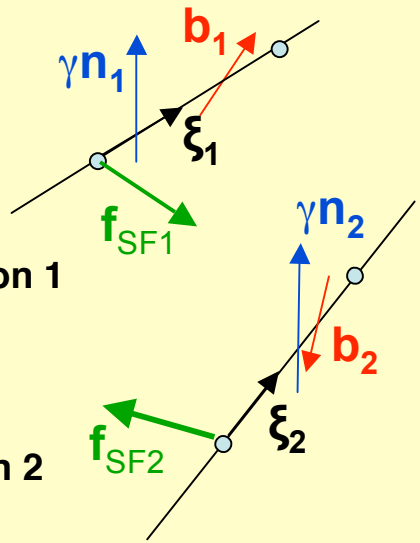

Partial dislocation 1

Partial dislocation 2

Each dislocation segment is now defined by three vectors: γn, b and ξ. This gives the right stacking fault force $\mathbf{f}_{SF}$

To the Peach-Koehler force acting on each segment we now add a new contribution due to the stacking fault

$$\mathbf{f}_{SF} = \xi \times \gamma\mathbf{n}$$

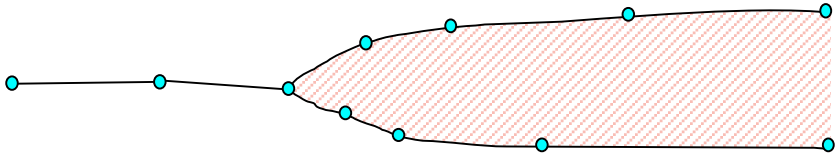

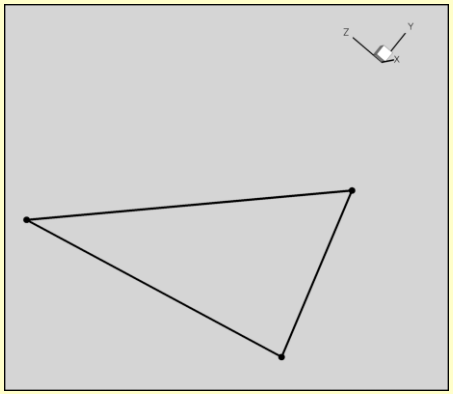

A Frank loop dissociates into partials to give a stacking-fault tetrahedron

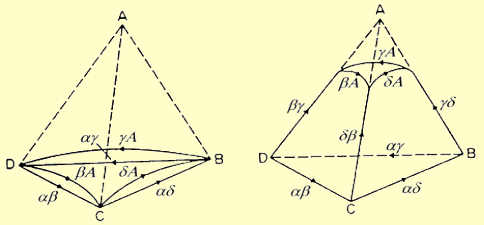

Fitting Procedure

We fit Dislocation Dynamics free parameters with atomistic calculations

- We fit free parameters in DD simulations (μ, ν, a, γ and core energy) to MD simulations of Shockley partial separation distance

Partial dislocation distance as a function of non-glide stress

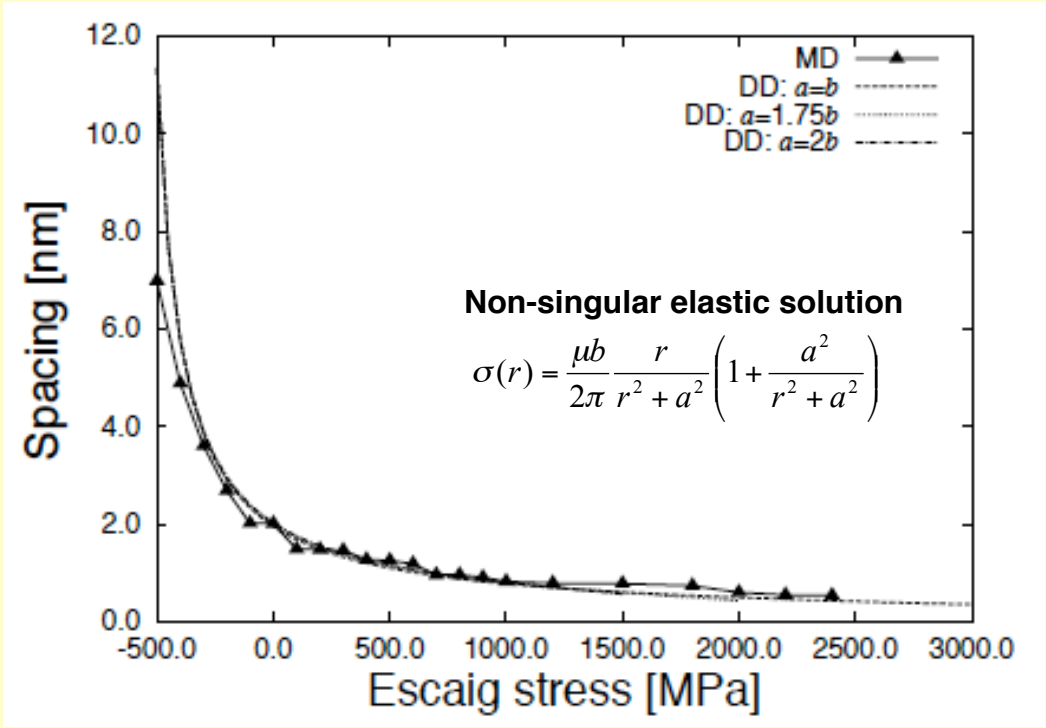

Separation between partials

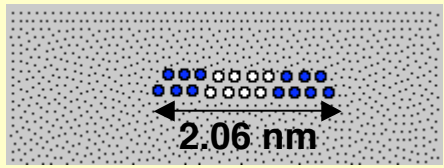

Equilibrium separation at zero stress

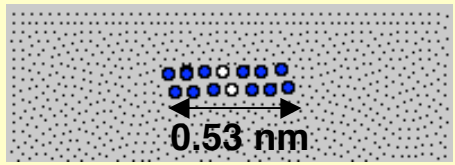

Configuration at 2000 MPa of Escaig stress (constriction)

γ is obtained from the interatomic potential
μ is obtained after rotating the compliance tensor to the particular geometry of fcc slip
ν is obtained from self-consistency with μ and B

At $a=1.75b$ we find the best compromise between matching the equilibrium separation distance and the constriction stress

Comparison with experiments

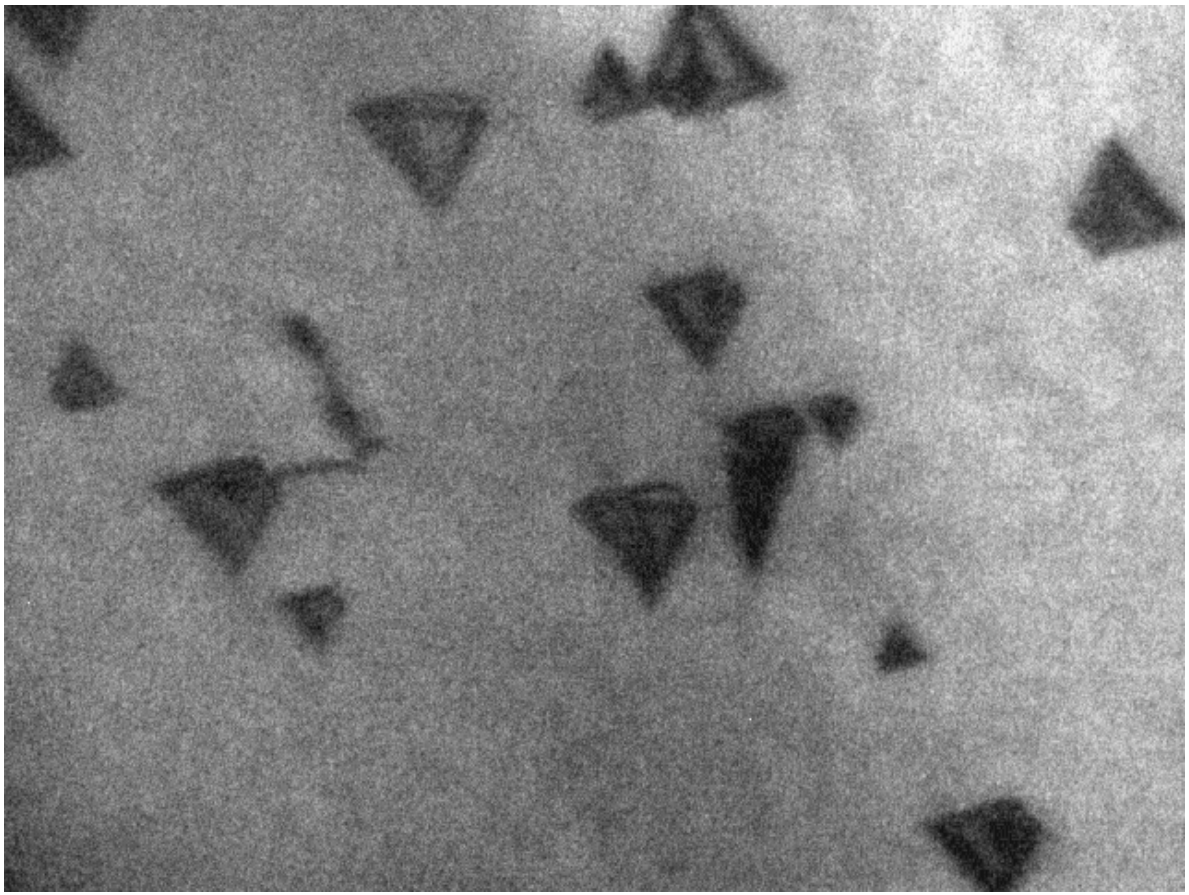

Dislocation moving through a SFT field in Au
(Ian Robertson, UIUC, 2006)

Dislocation-obstacle interactions in FCC

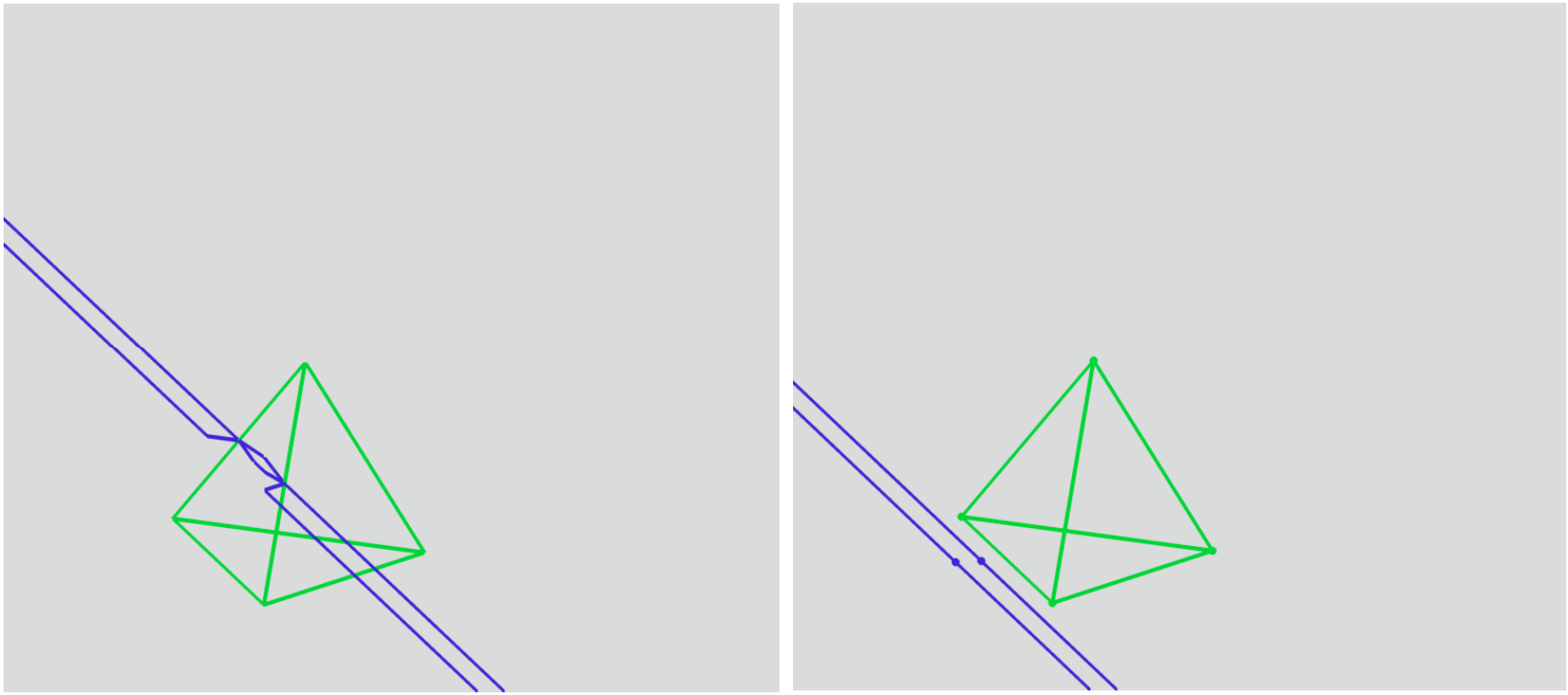

We perform simulations of screw dislocation/SFT interactions as a function of the plane of attack

Large Scale Dislocation Dynamics for Material Strength

Vasily Bulatov

This work was performed under the auspices of the U.S. Department of Energy by University of California Lawrence Livermore National Laboratory under contract No. W-7405-Eng-48.

The method of Dislocation Dynamics

First proposed in mid-80's

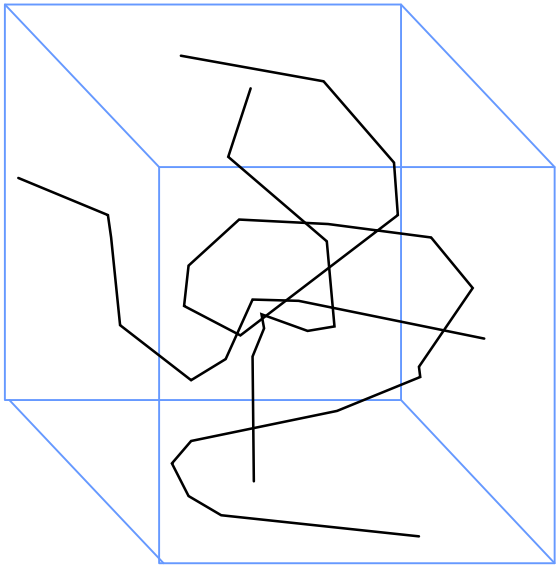

Yield and flow stress computed as functions of T, P, $\dot{\varepsilon}$ with full microstructural complexity

The DD approach

- Represent dislocation line network by a set of nodes connected by piece-wise straight line segments
- Compute forces on the line segments produced by applied loads and all other segments
- Move the segments in response to the forces using mobility functions derived from theory, atomistic simulations or experiment
- Keep track of dislocation collisions and dissociation and evolve the network connectivity as needed

Challenges

Accurate unit mechanisms of dislocation behavior - fidelity

Unit mechanisms of defect behavior in crystals are multiple, complex and difficult to quantify

Ability to simulate very large groups of crystal dislocations – computability

To account for the collective behavior of defects in the microstructure, it is necessary to track simultaneous evolution of very large defect ensembles over great many time steps

ParaDiS project at LLNL

ParaDiS* = *Parallel Dislocation Simulator

The goal: To overcome the computational limits of Dislocation Dynamics by massively-parallel computing

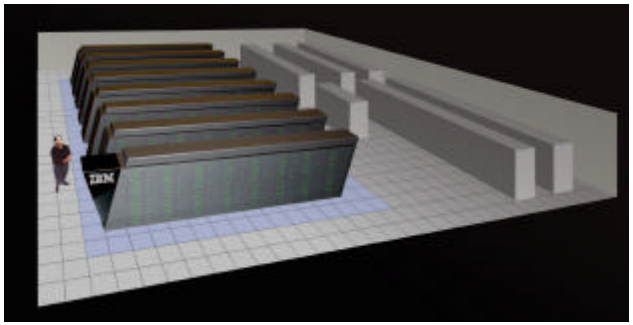

The means: New developments in dislocation physics, mathematical algorithms and computational sciences

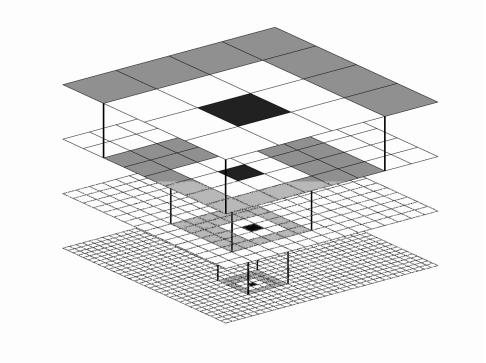

***ParaDiS* team includes physicists, engineers and computer scientists from LLNL and Stanford**

ParaDiS is much more than a code writing project

New developments in dislocation physics

- Mechanisms of dislocation motion
- Mechanisms of dislocation interactions
- Non-singular continuum theory of dislocations

Dislocation interaction in network

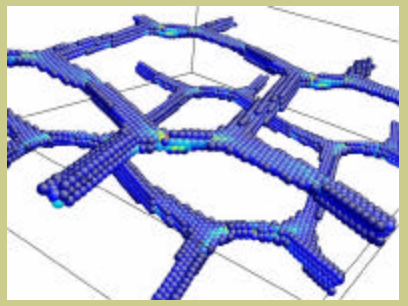

Bulatov and Cai, PRL **89**, 115501 (2002)

Dislocation motion producing point defects

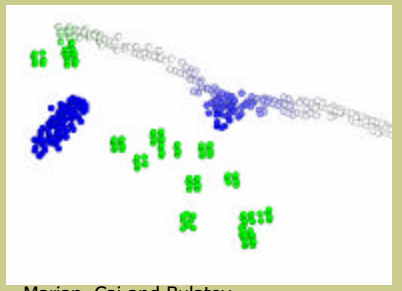

Marian, Cai and Bulatov,
Nature Materials **3**, 158 (2004)

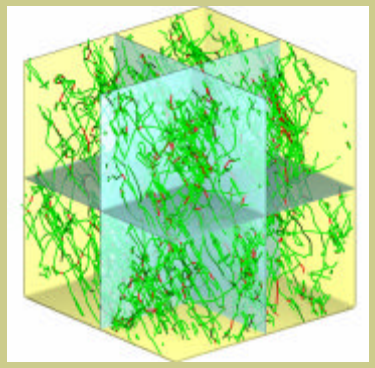

New algorithms

- Reduced set of topological operations
- O(N) fast-multipole algorithm
- Timing-based load balancing

For over 5 years *ParaDiS* served as a development framework

Rough motion mechanism

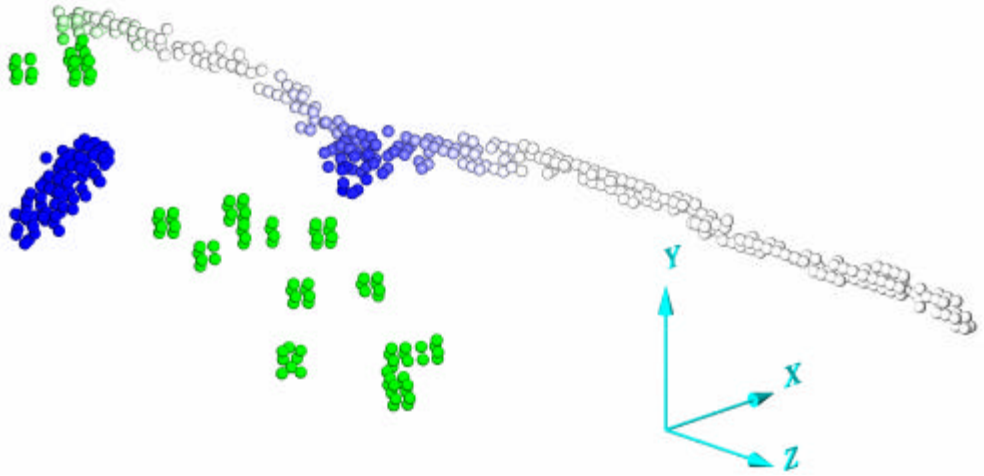

Rough motion mechanism

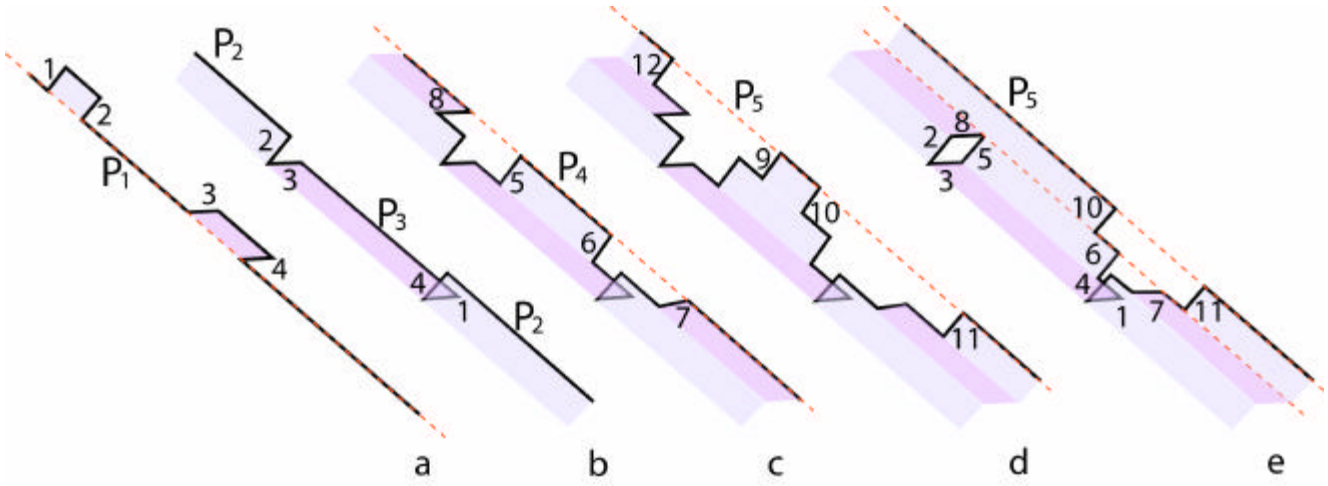

The mechanism is diffusion-less and intrinsic

Dislocation velocity as a function of stress

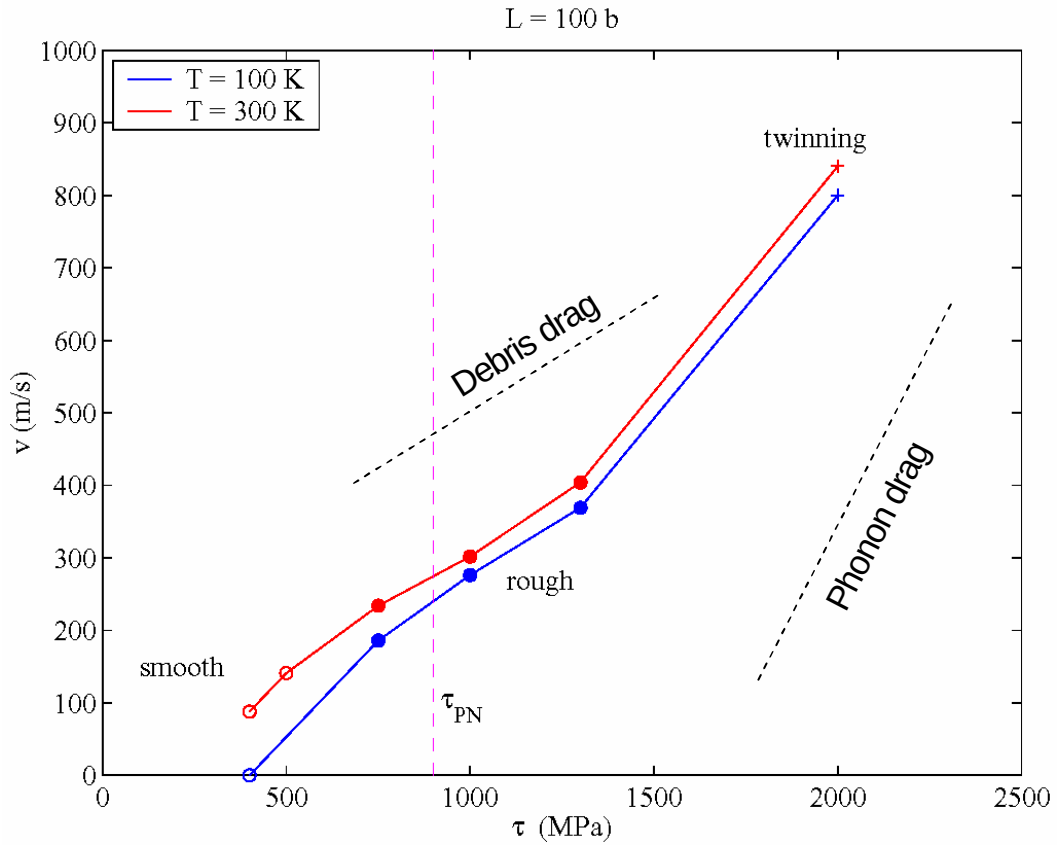

No transition at Peierls stress!

J. Marian, W. Cai and V. Bulatov, *Nature Mater.*, Jan. 2004.

Dislocation-dislocation interaction: the nodal effects

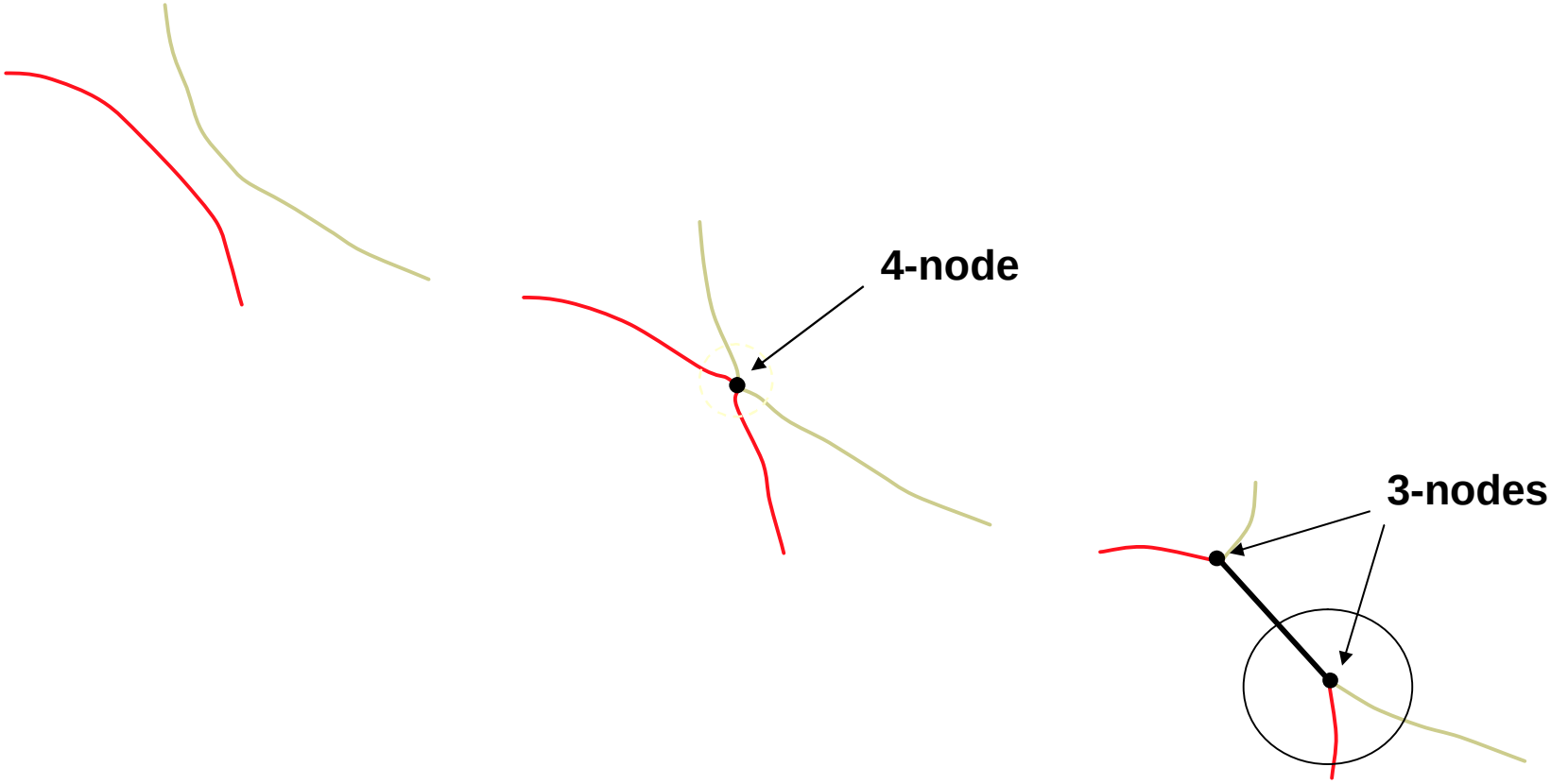

Formation of dislocation junctions and nodes

Peierls stress of a dislocation network

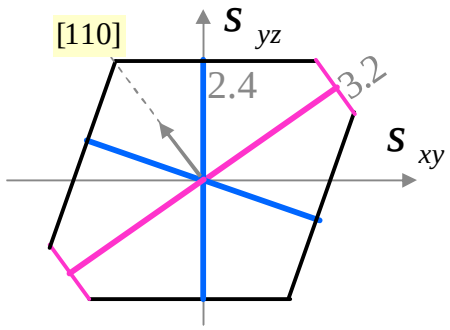

$t_c = 1.2\text{GPa}$

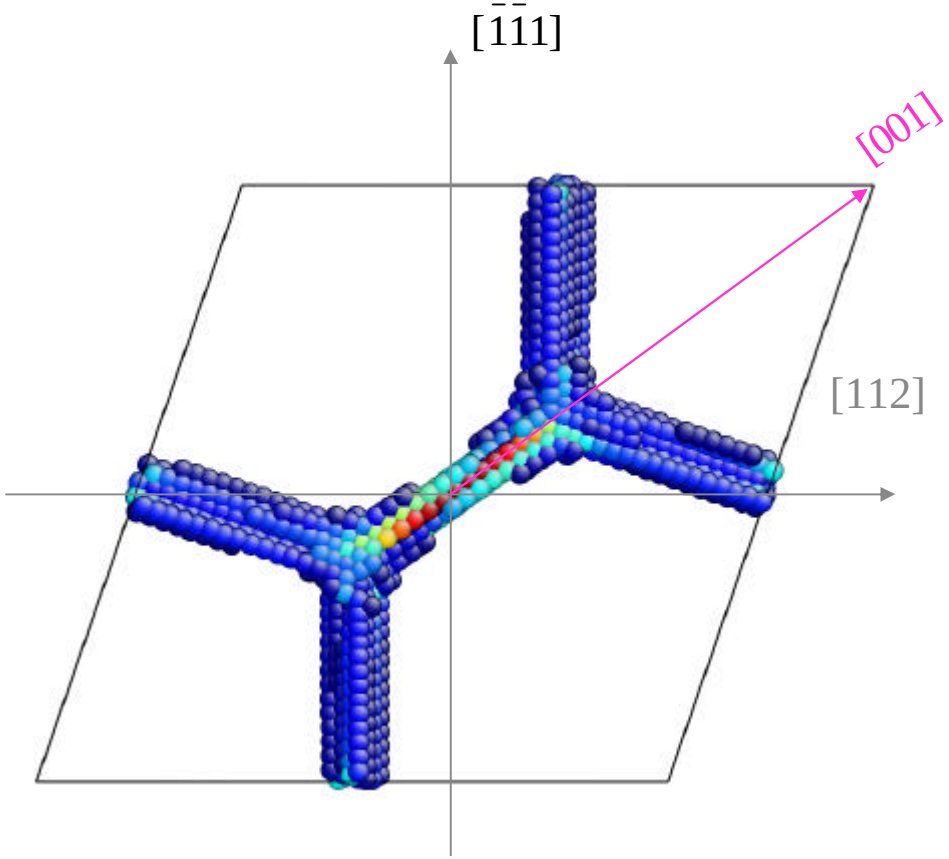

Peierls stress of a dislocation network

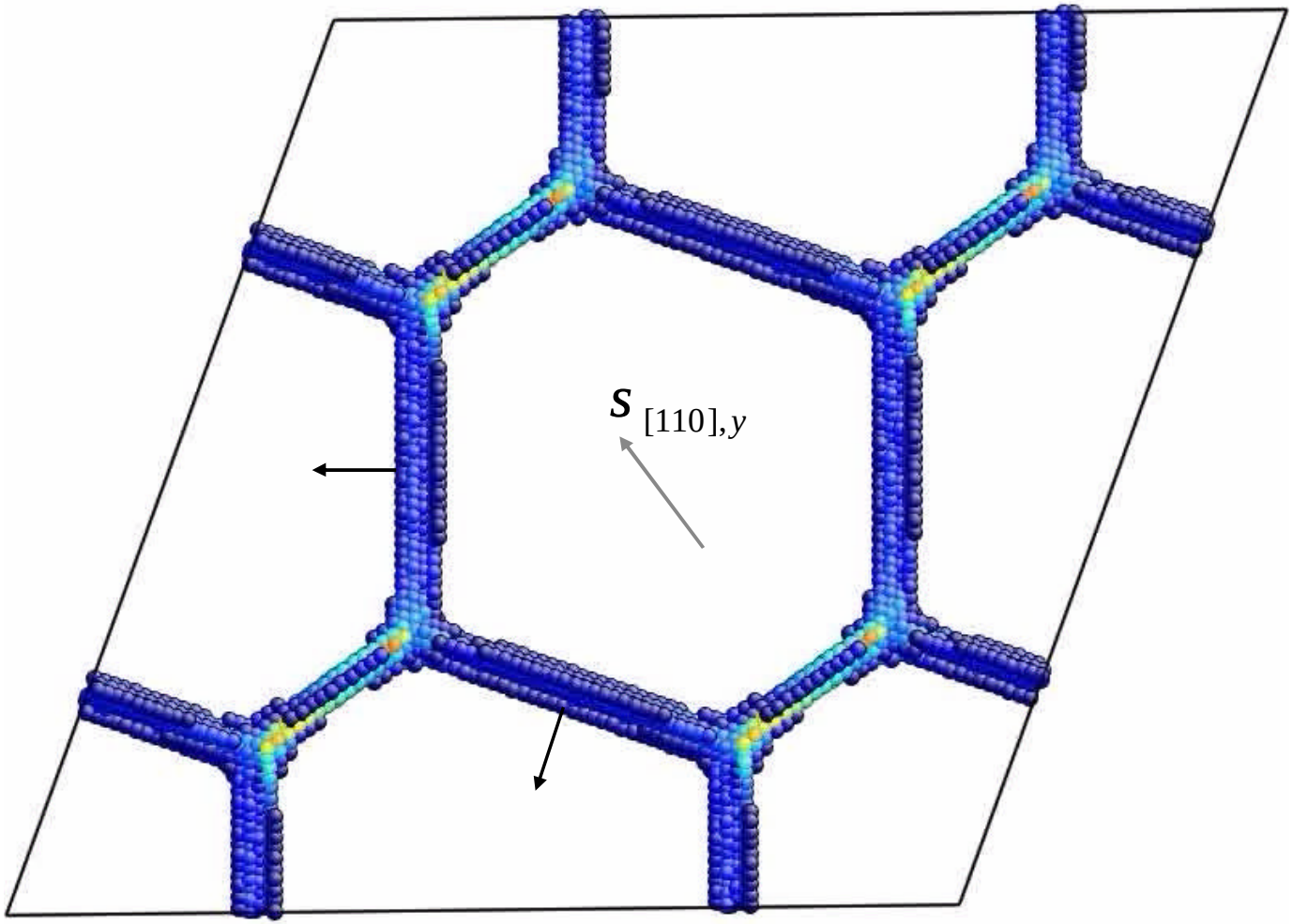

Nodal contribution to dislocation mobility

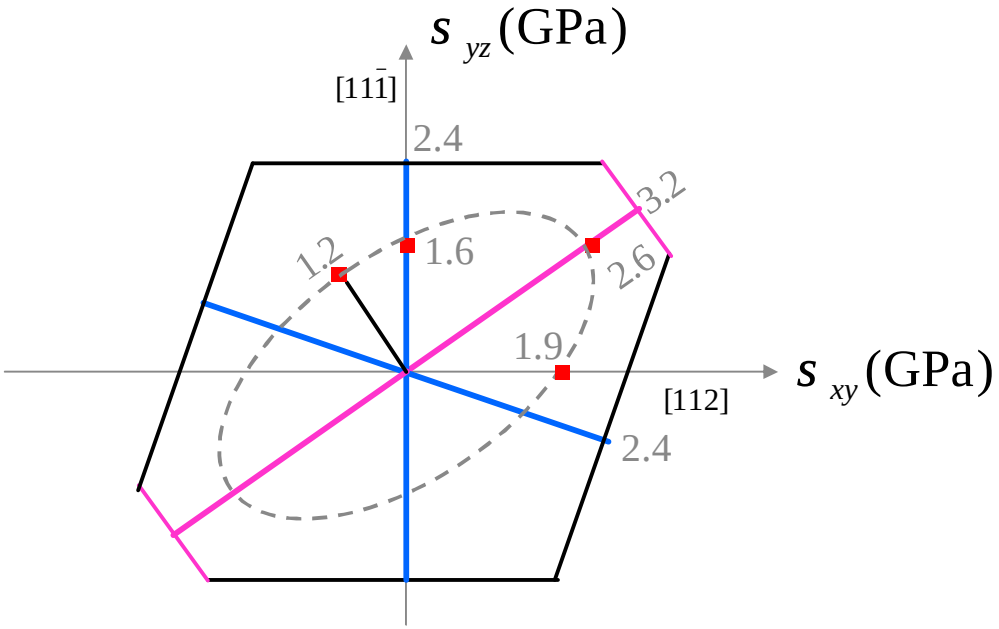

- Junction nodes lower critical stress by ~1/2 .
- Peierls stress by all potentials (Mo) ~ 2GPa
  measured yield stress at 0K ~ 0.75GPa

V. Bulatov and W. Cai, *PRL*, March 2003.

Dislocation multiplication under stress

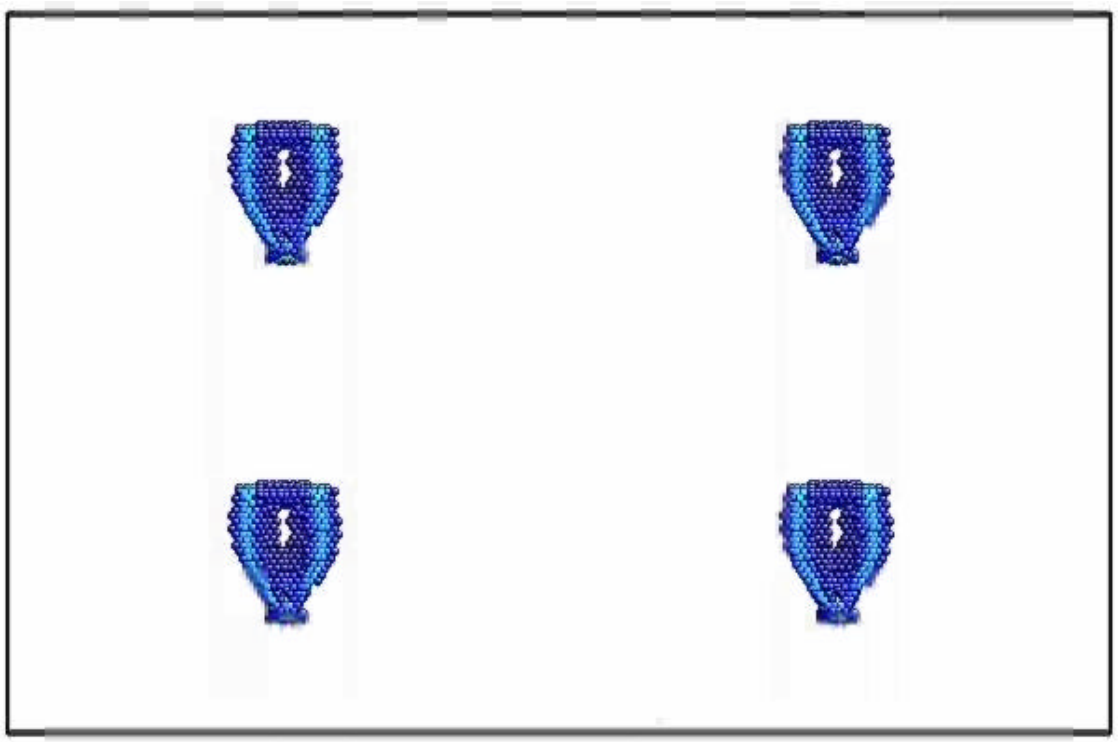

Something poked and cleared the stacking fault

What has actually happened?

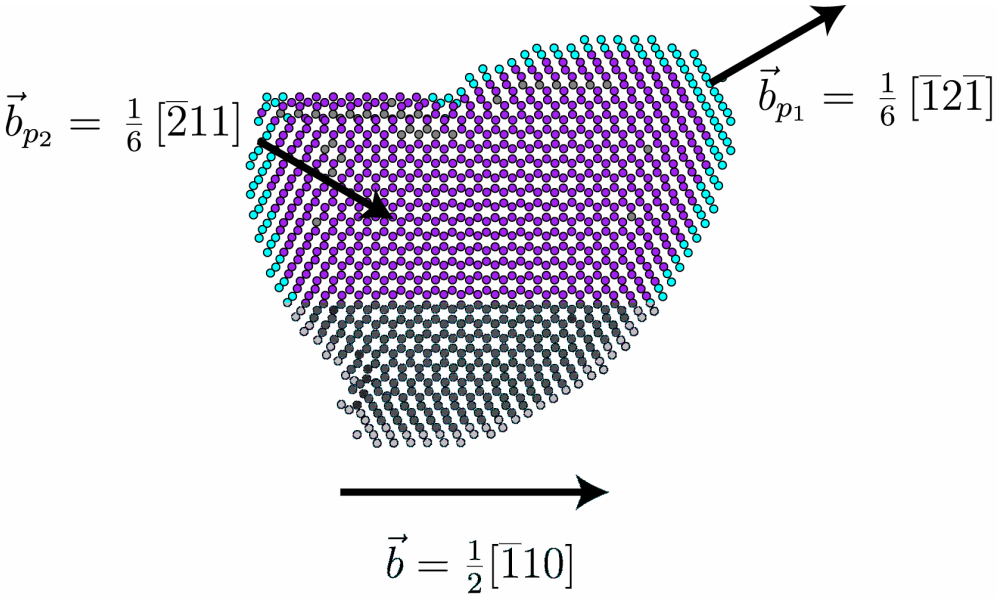

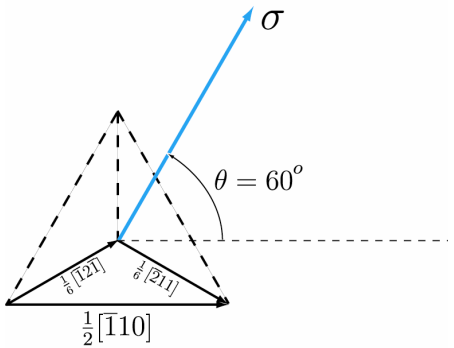

What has actually happened?

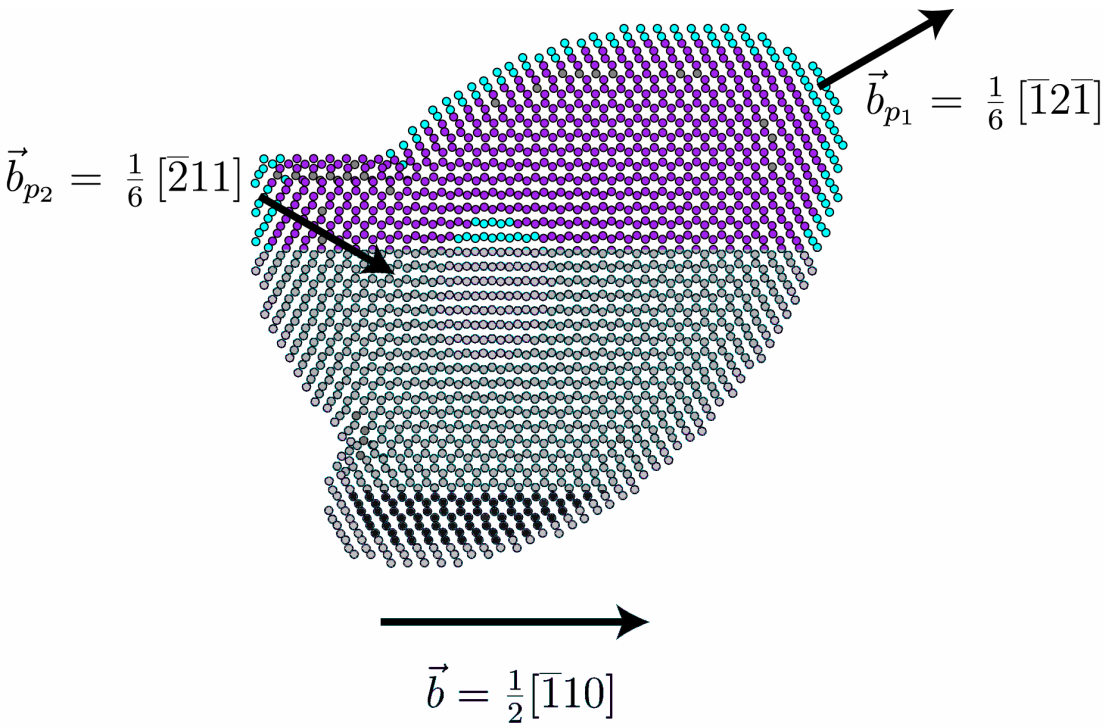

What has actually happened?

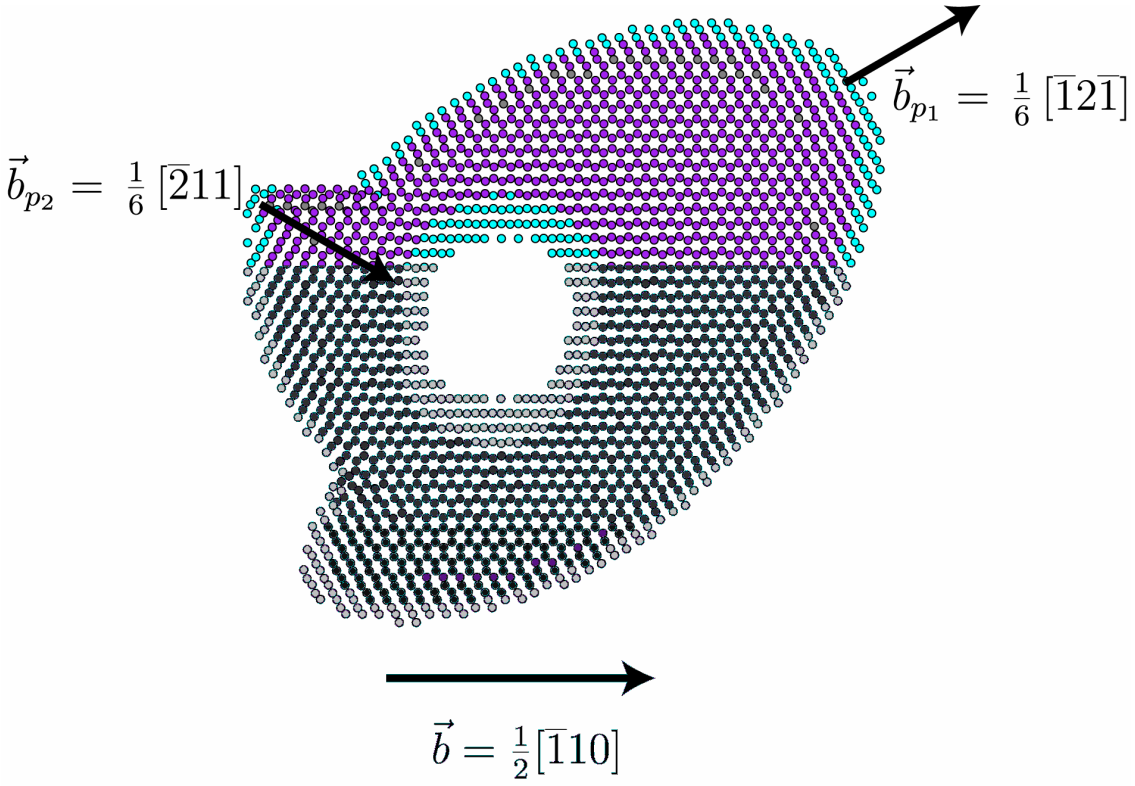

What has actually happened?

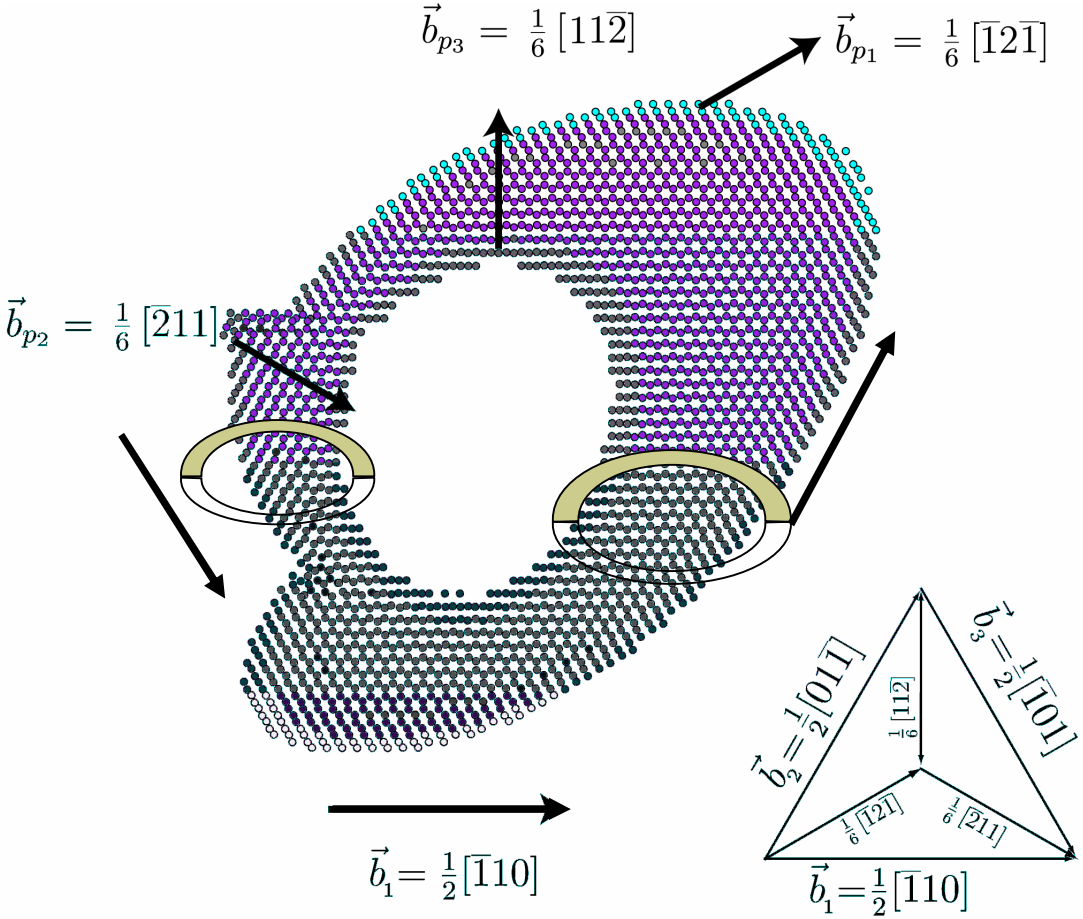

Multiplication of “wrong” dislocations

Dislocation source $\vec{\mathbf{b}}_1$ produces dislocations $\vec{\mathbf{b}}_2$ in a repeating sequence

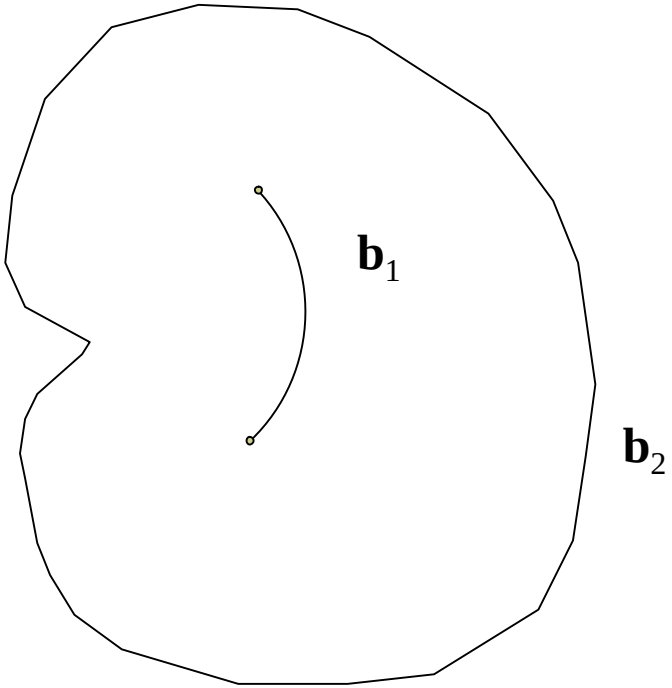

M. De Koning, W. Cai and V. Bulatov, *PRL*, June 2003.

A simpler case of a straight dislocation

b_{p1}= 1/6 [-2 1 1]

b_{p2}= 1/6 [-1 2 -1]

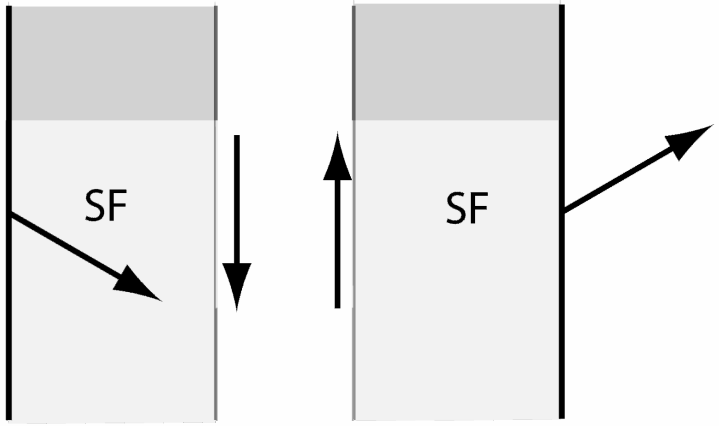

b_{p3}= 1/6 [1 1 -2]

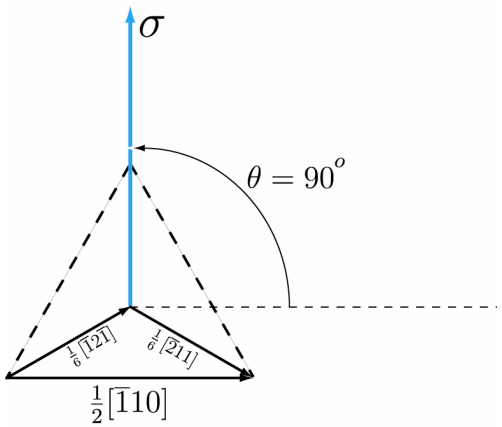

The dislocation is torn apart at a critical stress s = 920 MPa

Fun analogy: quark confinement

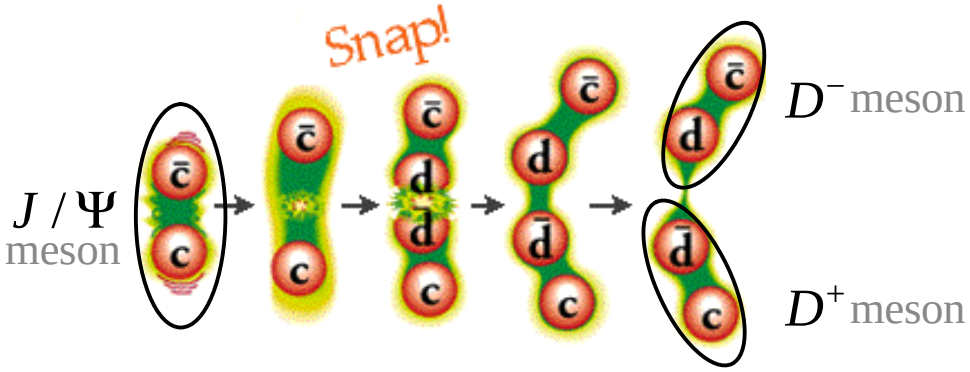

Analogy:

meson – perfect defect
quark – imperfect or *partial* defect
gluon – stacking fault

M. De Koning, W. Cai and V. Bulatov, *PRL*, June 2003.

More on partial defects in crystals

A hexagonal dislocation loop dissociated into two partial loops separated by a fault

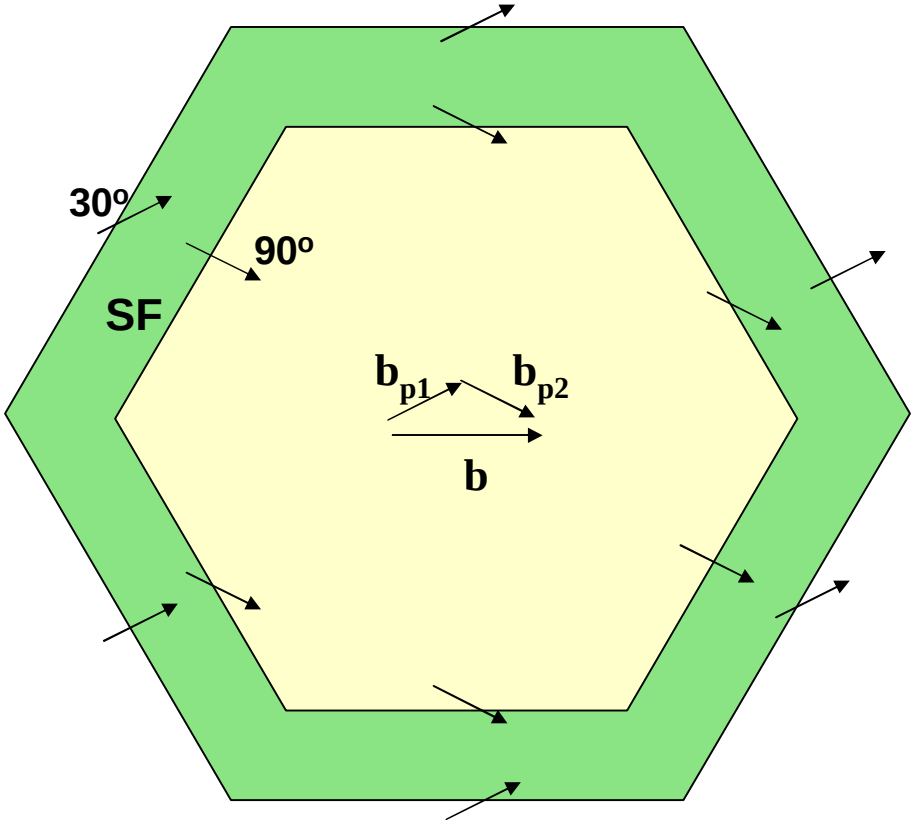

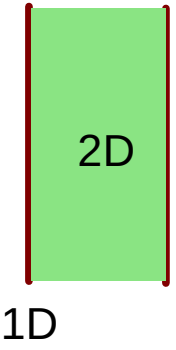

A grain boundary dissociates into two partial boundaries

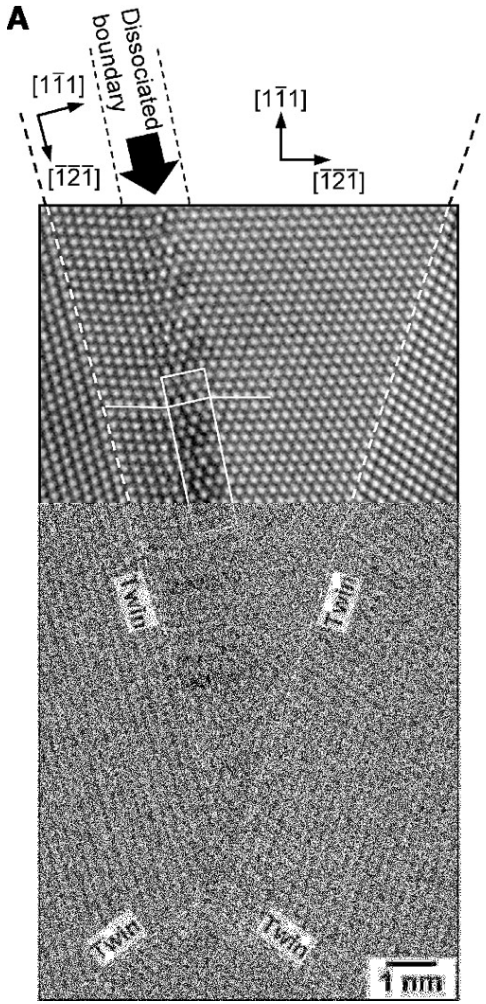

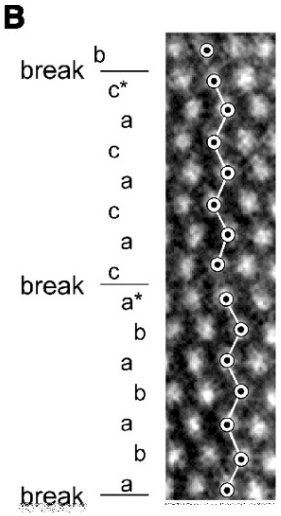

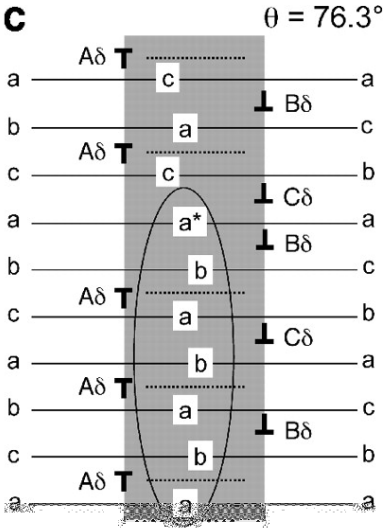

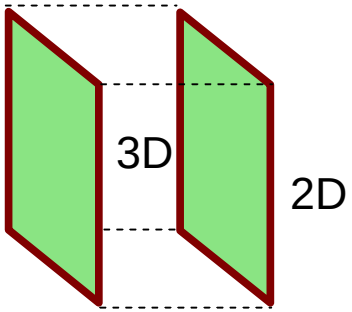

G. Lucadamo and D. L. Medlin
Science, May 2003

Partial kinks on dislocation lines

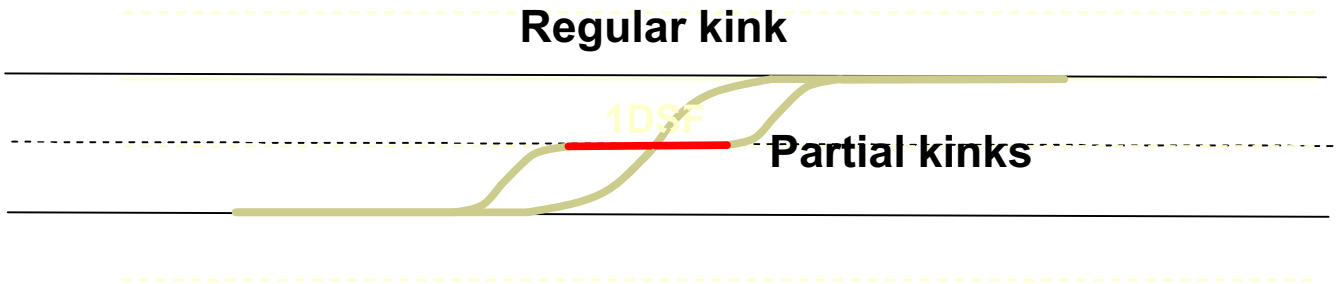

Atomistic mechanisms

… of dislocation behavior are multiple and complex

input to Dislocation Dynamics

Dislocation Dynamics: the challenge

A direct DD simulation of crystal strength involves tracking millions of dislocation lines over millions of integration time steps

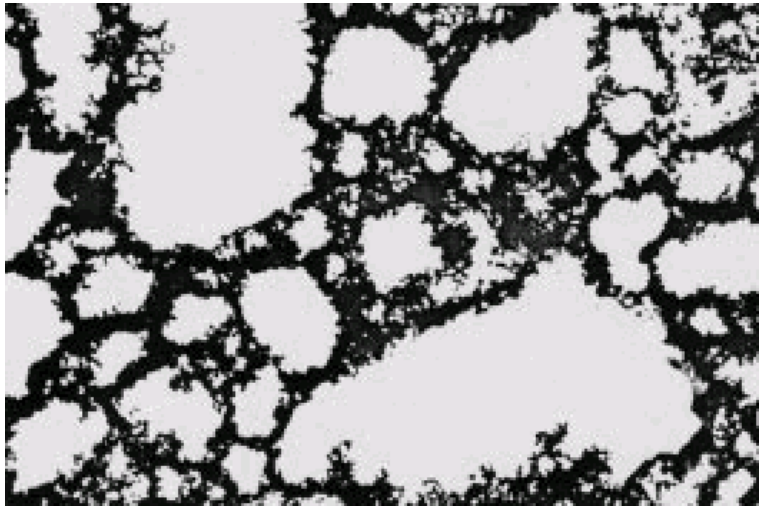

All DD codes developed so far stop short of these performance targets by 2-3 orders of magnitude

Challenge of computability in DD

Necessary to track simultaneous evolution of very large dislocation ensembles over very long time intervals

Massively parallel computing is the only conceivable route to success

Parallel implementation: problem 1

The microstructure is spatially and temporally heterogeneous

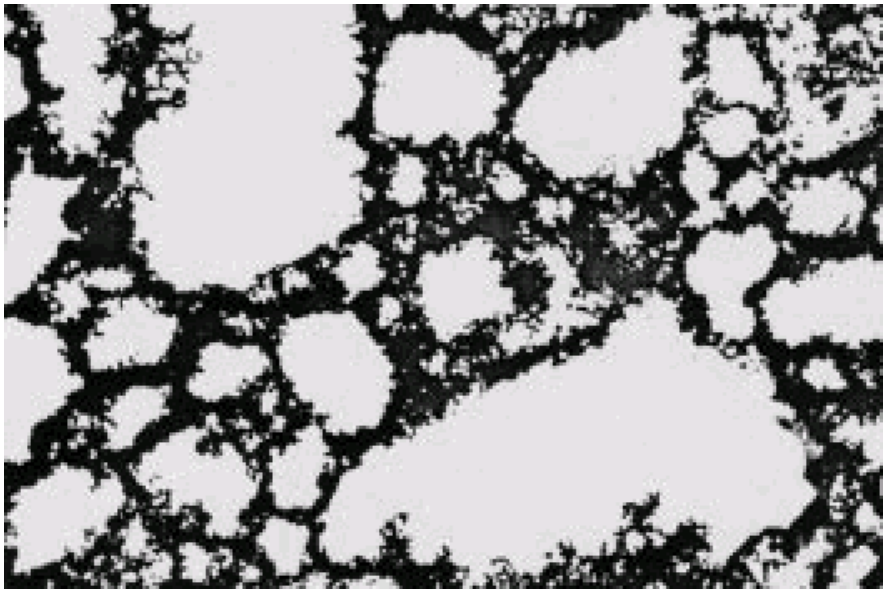

Parallel implementation: solution 1

Non-uniform volume partitioning

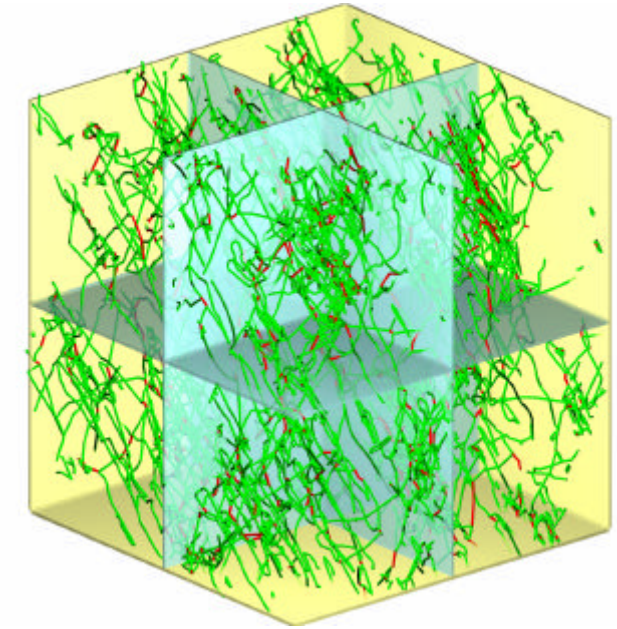

Initial partitioning assigns equal number of lines to the processors

Dynamic load balance

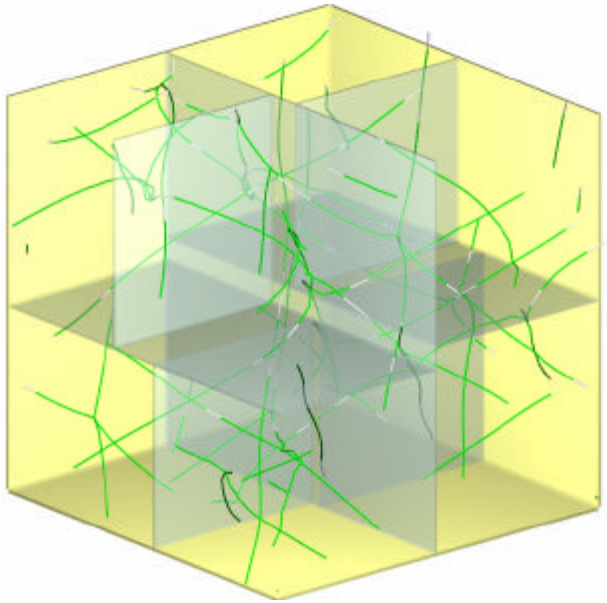

Re-partitioning follows timing history of each processor and adjusts domain boundaries to eliminate load dis-balance

Dynamic load balancing in *ParaDiS*

- **Local computational expense depends on the local density of lines**
- **Tendency of dislocations to cluster requires very careful dynamic space re-partitioning**

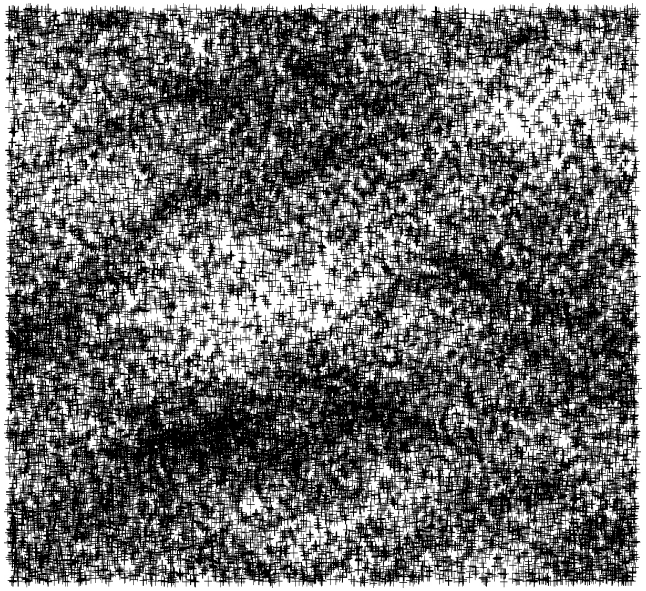

Dislocation cutting plane intersections

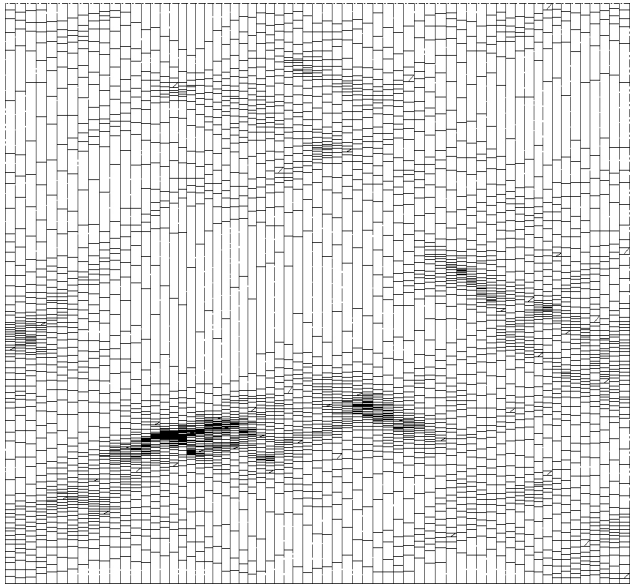

Corresponding space partitioning

Domain volumes span over three (!) orders of magnitude in a balanced simulation

Scaling up: *ParaDiS* on BG/L

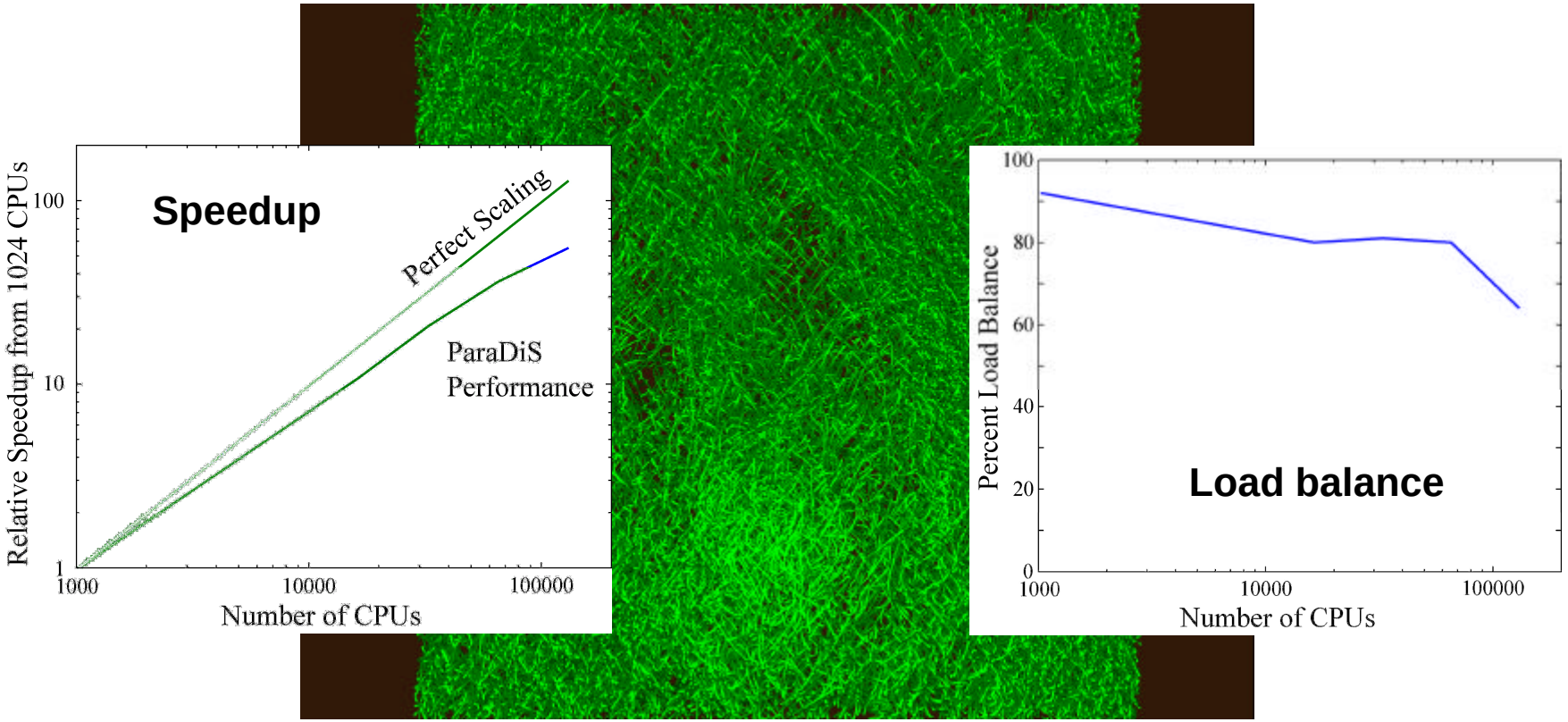

Outstanding parallel performance on BG/L

Parallel implementation: problem 2

Evolving topology of the dislocation microstructure is hard to treat consistently across the domain boundaries

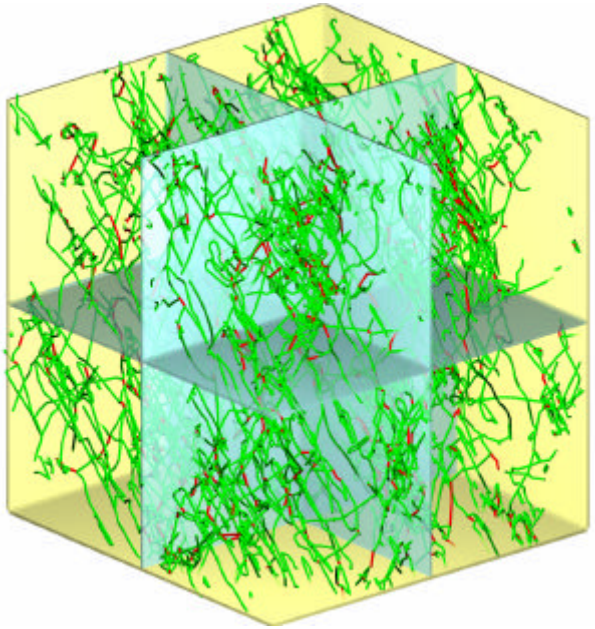

Parallel implementation: solution 2

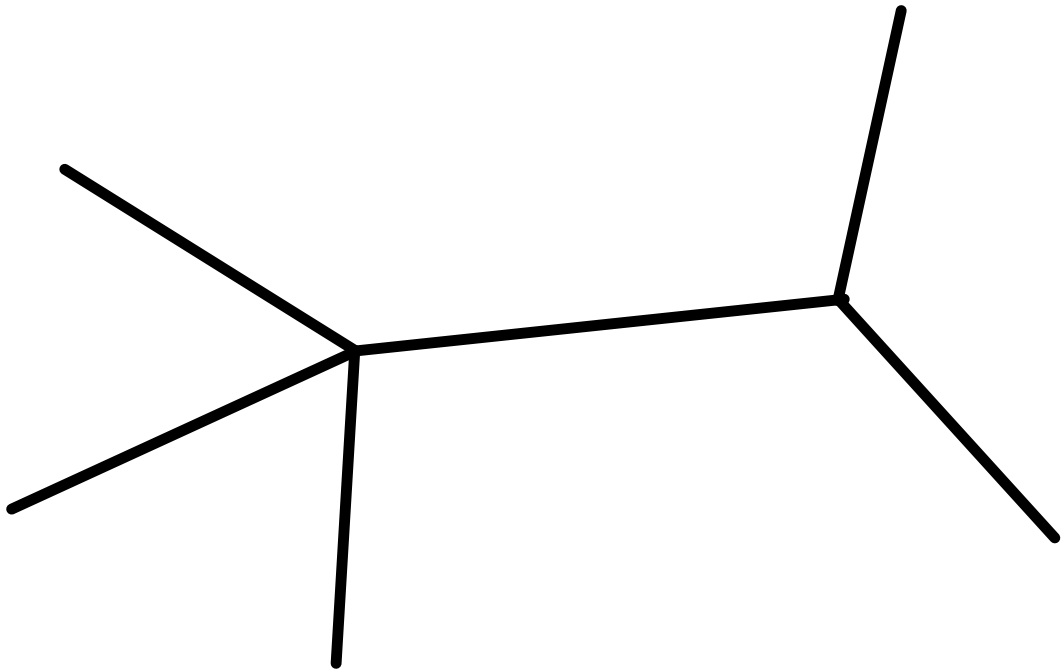

Reduced set of topological operations

Parallel implementation: solution 2

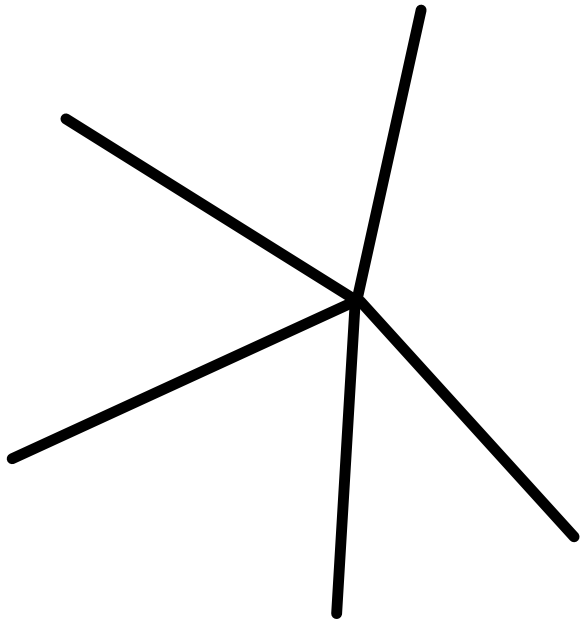

Merge two nodes in one

Parallel implementation: solution 2

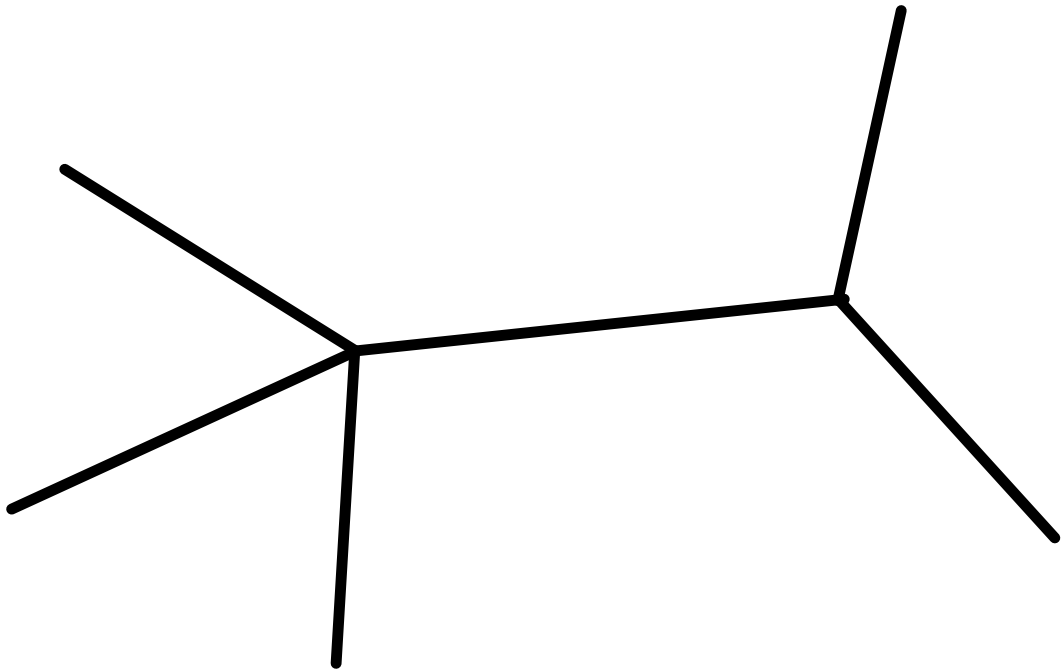

Split one node in two

Parallel implementation: problem 3

Long-range interaction among dislocations

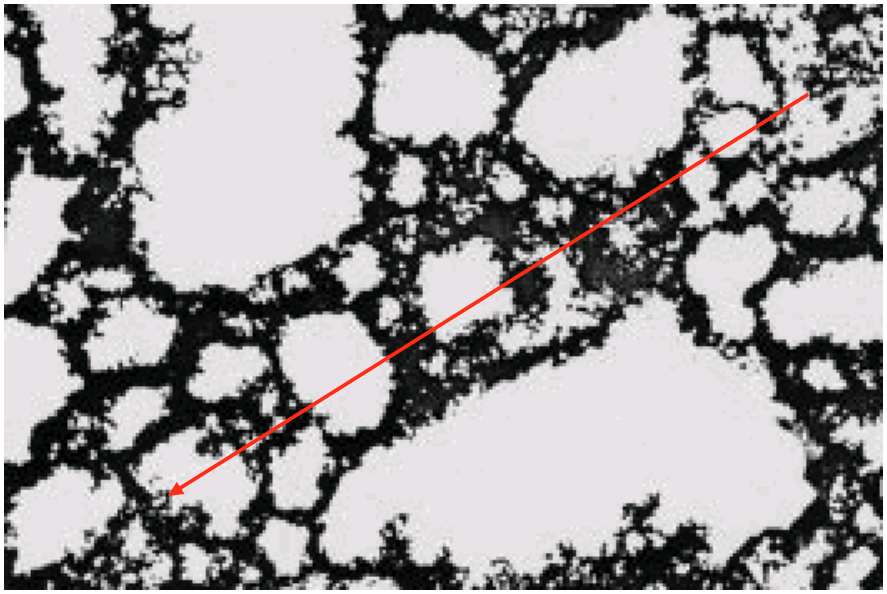

Parallel implementation: solution 3

O(N) Fast Multipole algorithm

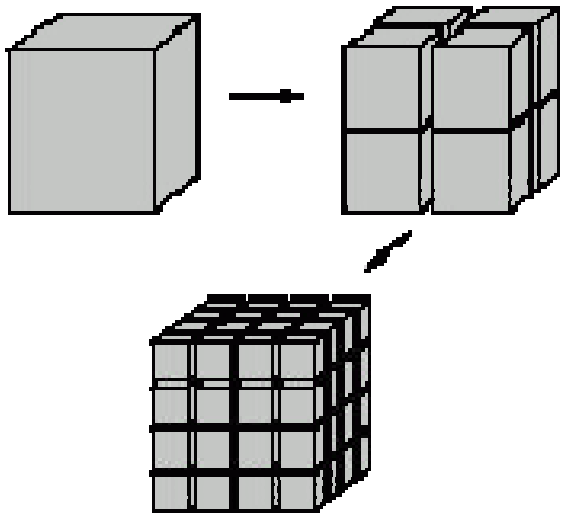

Parallel implementation: problem 4

Stiff equations of dislocation motion

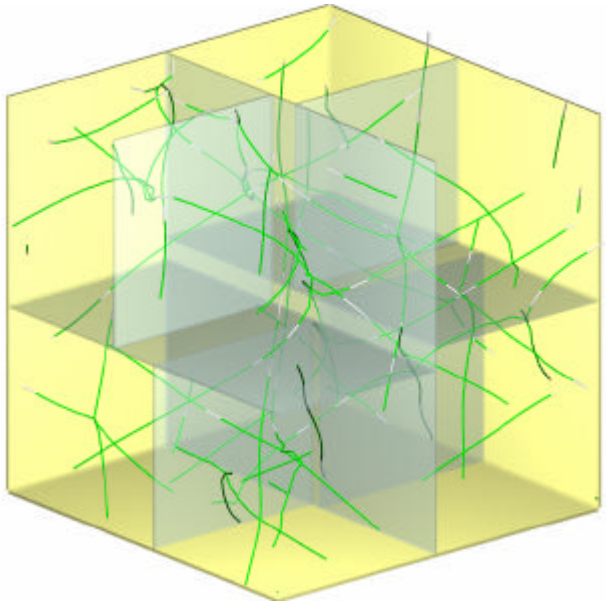

Parallel implementation: partial solution 4

Semi-implicit integrators

Non-singular interactions

New elastic theory of dislocations is developed that removes the singularity and remains analytical

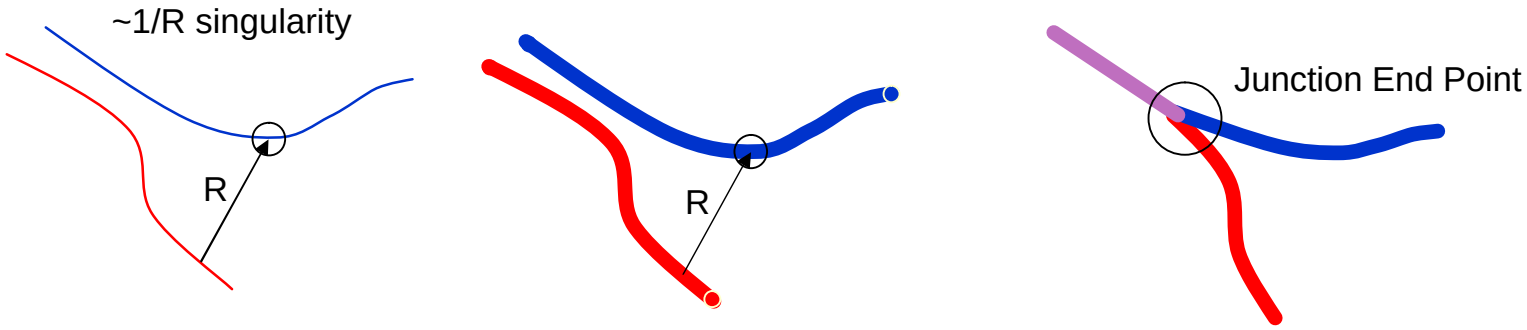

New theory is able to describe the forces at dislocation junction end points where the classical theory failed

ParaDiS code

Fully nodal representation of dislocation network

Generic part of the code is separate from the user-definable material module

The user defines material: crystal symmetry, Burgers vectors, elastic constants, dislocation mobility functions

ParaDiS connects dislocation behavior to crystal plasticity

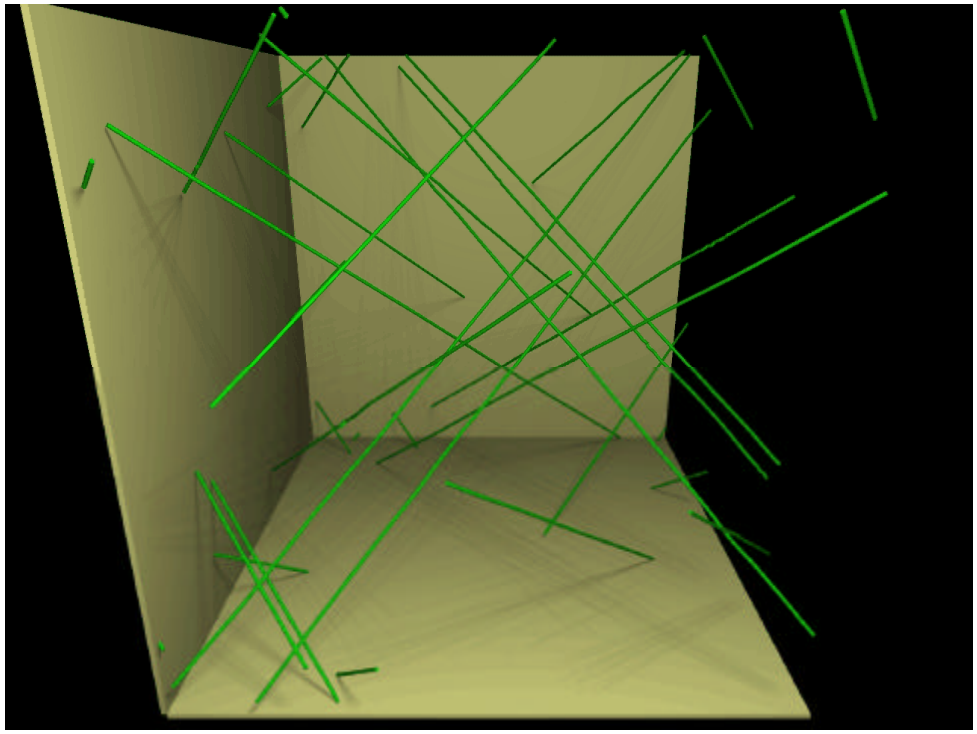

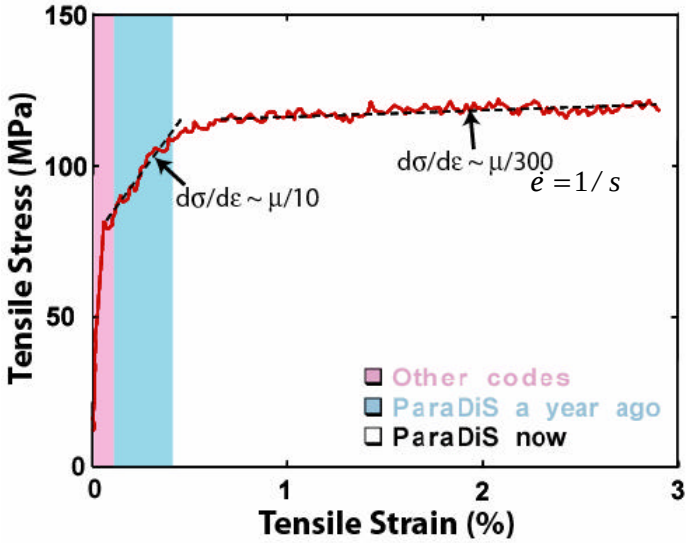

Direct calculations of plastic strength of a single crystal across the stages of strain hardening

ParaDiS: early science insights

ParaDiS simulations reproduce previously unexplained difference in orientation dependence of strain hardening in BCC Mo

Experiments

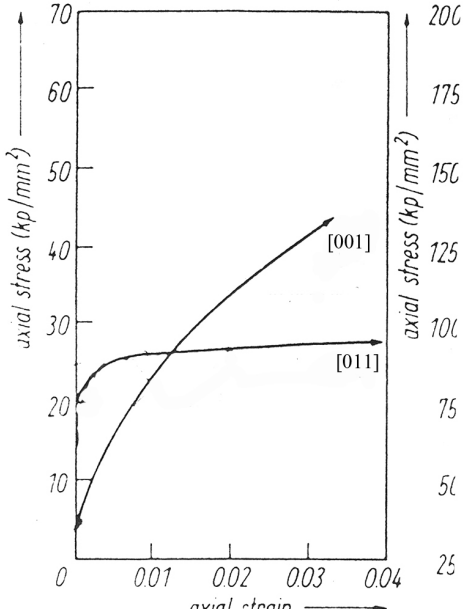

Simulations on Thunder

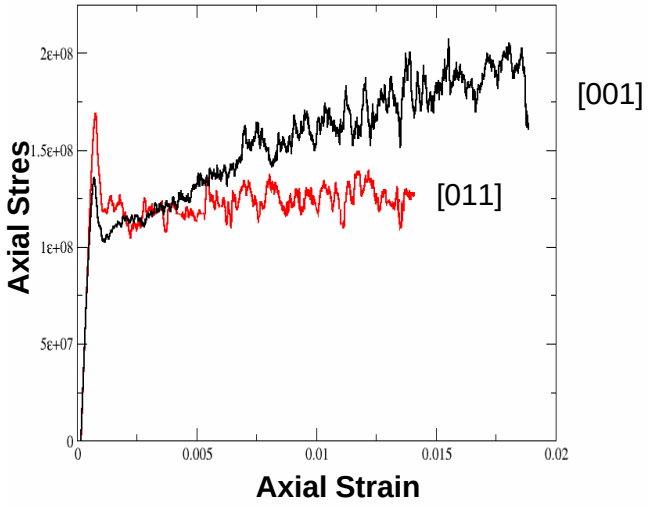

From: G. J. Irwin et al. phys. Stat. Sol. (a) 22, 685 (1974)

With _ParaDiS_ we are able to investigate the microstructural origins of this behavior

Multiple slip causes many-body dislocation reactions (multi-junctions) leading to increased strength

Multijunction-rich microstructures are able to multiply dislocations at a faster rate than multijunction poor microstructures

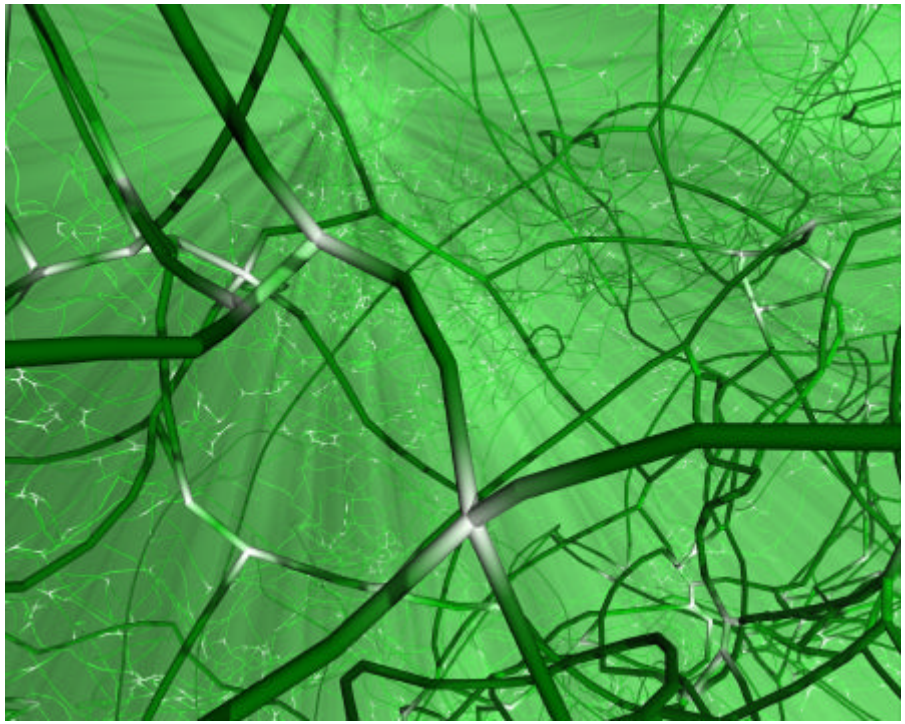

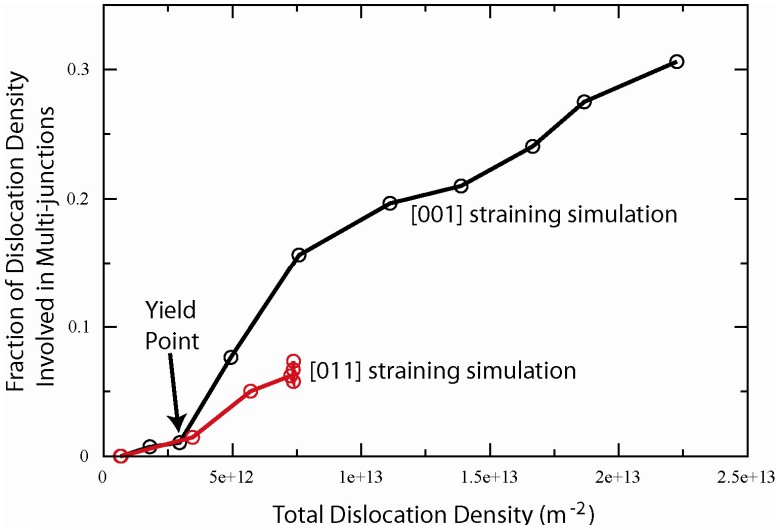

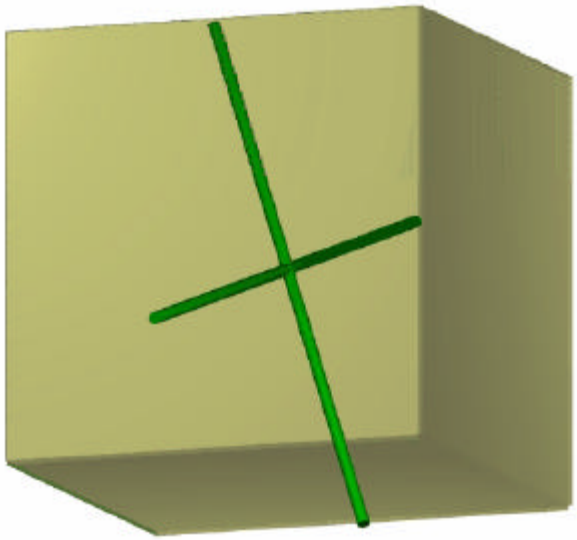

Existence of multi-junctions is verified by TEM investigation

Multi-junctions have a unique TEM signature that allows them to be distinguished from other dislocation arrangements

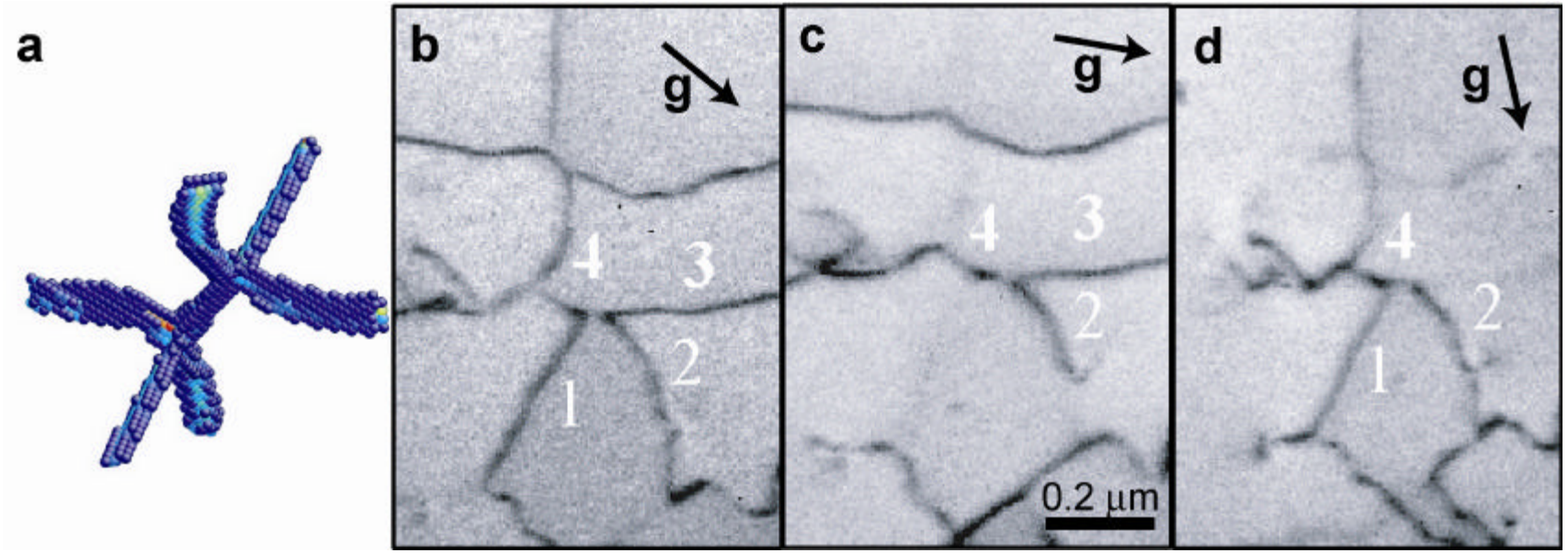

Multi-junctions are not rare but occur frequently under certain plastic processes

Visualizations lead to insights into the role of multi-junctions in microstructure dynamics

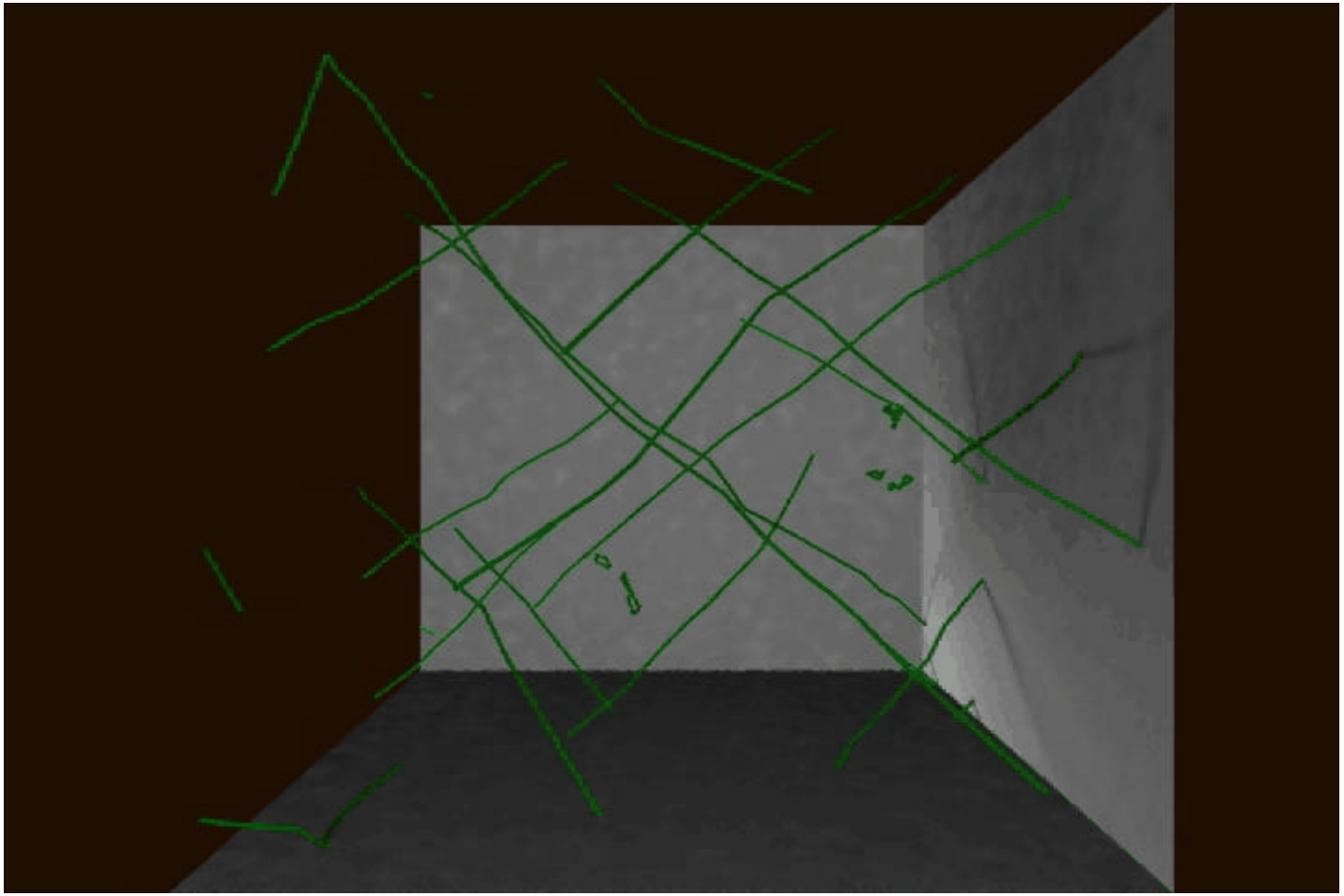

Multi-junctions act as static anchors of the microstructure: once formed they endure for long times and act as regenerative sources

Crystal Level Modeling of Phase Transformations

Nathan Barton
Richard Becker

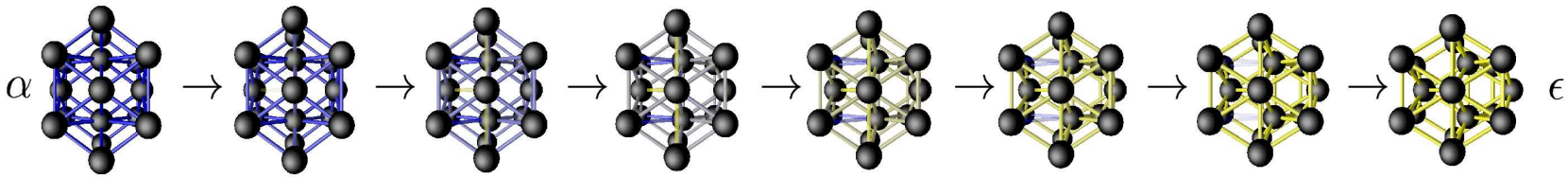

Lawrence Livermore National Laboratory

This work was performed under the auspices of the U.S. Department of Energy by the University of California, Lawrence Livermore National Laboratory under Contract No. W-7405-ENG-48.

UCRL-PRES-??????

Model features

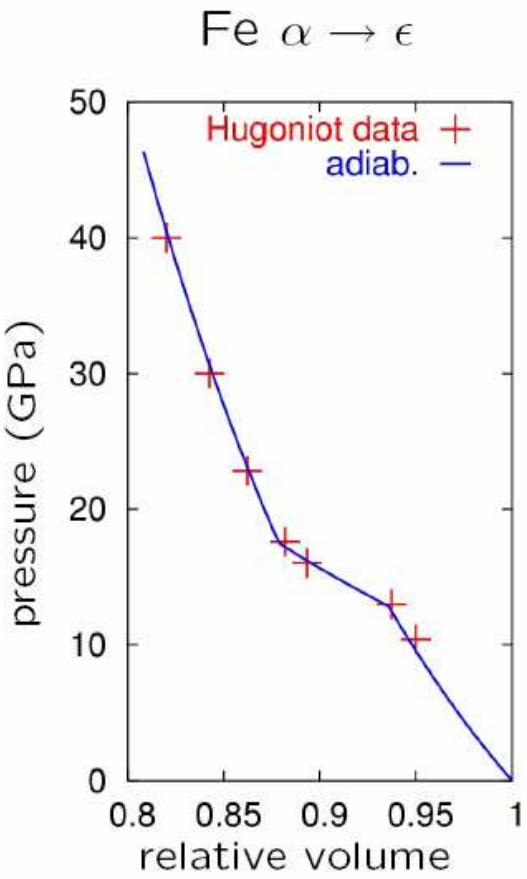

Data from Barker and Hollenbach, *J. Appl. Phys.*, 1974.

Model including structural changes – phase transformation and twinning

Crystal level continuum mechanics approach

Diffusionless transformations

Deformation driven context

Large shape and volume changes

Both elastic and plastic accommodation

Patoor *et al.*, *J. Phys. IV*, 1996.

Crystal elasto-viscoplasticity within constituents

Within a given constituent $\mathbf{F} = \mathbf{V} \cdot \mathbf{R} \cdot \mathbf{F}^{\mathrm{p}}$

- $\mathbf{F}^{\mathrm{p}}$ dislocation glide – does not change lattice
- $\mathbf{V}$ lattice stretch – both thermal and elastic
- $\mathbf{R}$ lattice rotation – same in all constituents

For mode i from ζ to ν:

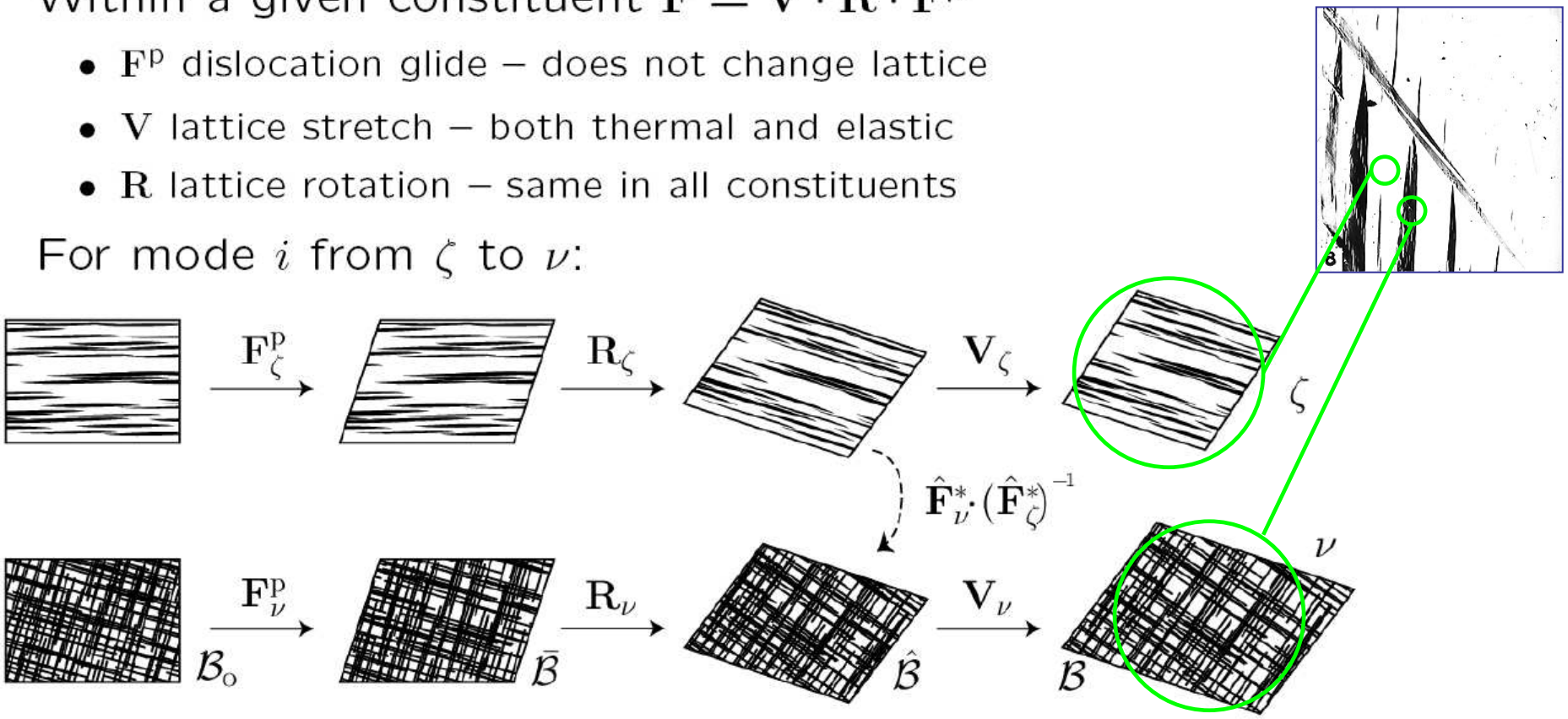

One obtains:

$$\mathbf{L}_{(i)} = \dot{m}_{(i)} \left[\mathbf{V}_{\nu} \cdot \left(\hat{\mathbf{G}}_{(i)}(m_{\eta}) \right) \cdot (\mathbf{V}_{\zeta})^{-1} + \mathbf{V}_{\nu} \cdot (\mathbf{V}_{\zeta})^{-1} - \mathbf{I} \right]$$

Driving force for transformation

$$f_{(i)} = f^{\mathsf{d}}_{(i)} - C_{(i)} \cdot (\theta - \theta^{\circ}_{(i)}) + f^{\mathsf{r}}_{(i)}(m_\eta)$$

$f^{\mathsf{d}}_{(i)}$ – from work of deformation

$f^{\mathsf{r}}_{(i)}$ – from interaction effects among constituents

For deformation part of driving force:

- $f^{\mathsf{d}}_{(i)} = \boldsymbol{\tau}_{\eta_{\mathsf{fr}}(i)} : \mathbf{P}_{(i)}$ with $\boldsymbol{\tau}_{\eta_{\mathsf{fr}}(i)} = \det(\mathbf{V}_{\eta_{\mathsf{fr}}(i)})\boldsymbol{\sigma}$
- Simplest form: $\mathbf{P}_{(i)} = \mathrm{symm}\,(\llbracket \mathbf{F} \rrbracket)$
- From motivated from $f^{\mathsf{d}}_{(i)} = \int_{\chi_i} \boldsymbol{\tau}_{\eta_{\mathsf{fr}}(i)} : \mathbf{D}\, d\chi$

  $\mathbf{P}_{(i)} = \mathrm{symm}\left(\ln(\mathbf{F}_{(i)})\right),\ \mathbf{F}_{(i)} = \mathbf{V}_{\eta_{\mathsf{to}}(i)} \cdot \widehat{\mathbf{F}}^{*}_{\eta_{\mathsf{to}}(i)} \cdot (\widehat{\mathbf{F}}^{*}_{\eta_{\mathsf{fr}}(i)})^{-1} \cdot (\mathbf{V}_{\eta_{\mathsf{fr}}(i)})^{-1}$

Numerics

Forward update of dislocation densities h_ν

R			x		
$\dot{m}_\nu = \sum_{\{(i)\|\eta_{\text{to}}(i)=\nu\}} \dot{m}_{(i)} - \sum_{\{(i)\|\eta_{\text{fr}}(i)=\nu\}} \dot{m}_{(i)}$	$\ldots$	n_{C}	m_η	$\ldots$	n_{C}
$\langle \mathbf{L} \rangle = \mathbf{L}^\chi + \sum_\zeta v_\zeta \mathbf{L}_\zeta$	$\ldots$	9	$\boldsymbol{\sigma}$	$\ldots$	6
			$\boldsymbol{\Omega}^R$	$\ldots$	3

Solution strategy: Trust region subproblem via the subspace method

- Handles bound constraints by an active set approach
- Equality constraint forces $\sum_\zeta m_\zeta = 1$
- With specialization for depletion and flow-through

Energy and temperature

Within a constituent: $e = e^{\mathrm{th}} + e^{\mathrm{c}}$

- $p_{\mathrm{b}}(\mu, e) = p_{\mathrm{g}}(\mu) + \bar{\rho} \cdot (\Gamma_{\mathrm{o}} + a\mu) \cdot e$
- for cold energy, integrate: $\frac{\mathrm{d}e^{\mathrm{c}}}{\mathrm{d}\mu} = \frac{p_{\mathrm{c}}}{(\bar{\rho})(\mu+1)^2}$
- neglecting contributions from non-bulk strains
- typical form in compression:
  $p_{\mathrm{g}}(\mu) = \frac{K_{\mathrm{o}}\mu\left[1+(1-\frac{\Gamma_{\mathrm{o}}}{2})\mu-\frac{a\mu^2}{2}\right]}{[1-(S-1)\mu]^2}$

Total specific internal energy:
$e = e^{\mathrm{th}} + e^{\mathrm{c}} + e^{\mathrm{r}}$

- $e^{\mathrm{th}} = \sum_\zeta (m_\zeta e^{\mathrm{th}}_\zeta) = \theta \sum_\zeta (m_\zeta c^{\mathrm{v}}_\zeta)$
- $e^{\mathrm{c}} = \sum_\zeta (m_\zeta e^{\mathrm{c}}_\zeta)$

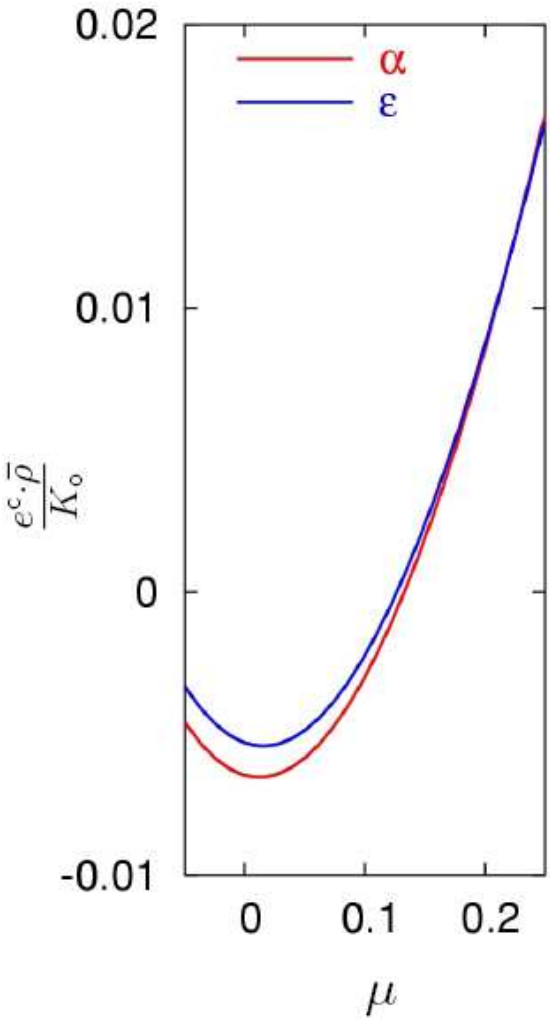

Application: $\alpha \leftrightarrow \varepsilon$ in iron

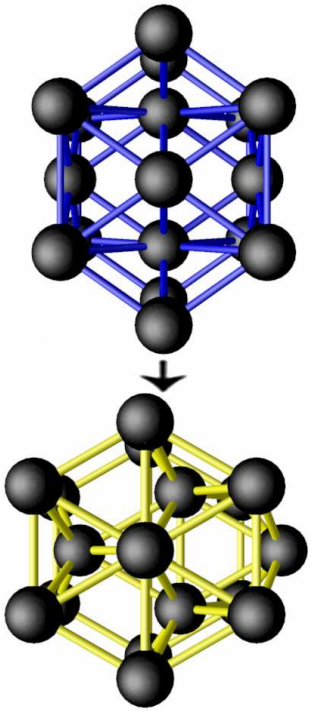

- Model development and testing with $\alpha \leftrightarrow \varepsilon$ transformation in iron
- Pressure driven polymorphic transformation
  - Transformation pressure ≈ 13 GPa
  - α phase plastic flow strength ≈ 0.4 GPa
- Have examined:
  - Single crystal behavior
  - Quasi-static compression of polycrystals
  - Impact loading of single crystals and polycrystals

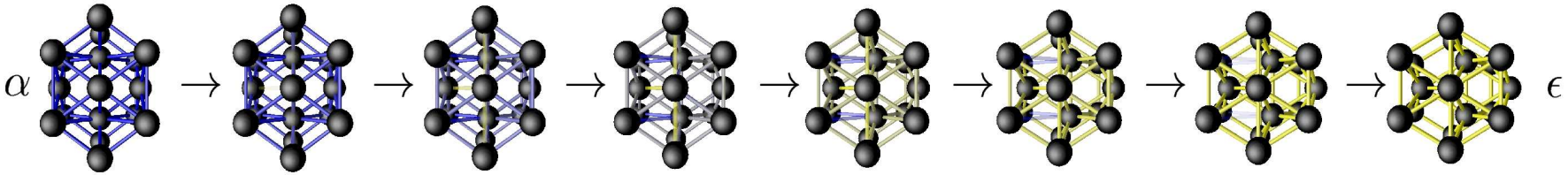

Interaction energy models

Meant to capture additional stored energy

- microstructural elastic strains
- do not contribute to observed deformation
- contribute to stored energy and thus to driving force

Force contribution:

- $f^{\mathsf{r}}_{(i)} = -\dfrac{\bar{\rho}_{\eta_{\mathsf{fr}}(i)}}{\bar{\rho}} \left(\dfrac{\partial E^{\mathsf{r}}}{\partial m_{\eta_{\mathsf{to}}(i)}} - \dfrac{\partial E^{\mathsf{r}}}{\partial m_{\eta_{\mathsf{fr}}(i)}} \right)$

Interaction energy with habit planes (model a):

- $E^{\mathsf{r}} = C^{\mathsf{r}} \sum_{\zeta,\nu} \left(m_\zeta \, A^{\mathsf{r}}(\zeta,\nu) \, m_\nu \right)$ with $A^{\mathsf{r}}(\zeta,\nu) = (1 - |\mathbf{n}_\zeta \cdot \mathbf{n}_\nu|)$

Pair interaction energy (model b):

- $E^{\mathsf{r}} = C^{\mathsf{r}} \sum_{\zeta,\nu} \left(m_\zeta \, m_\nu \right)$

Comparison to experimental impact data

Single crystal simulation data and polycrystal experimental data

Experimental data are from L. M. Barker and R. E. Hollenbach, *J. Appl. Phys.*, 45(11):4872–4887, 1974.

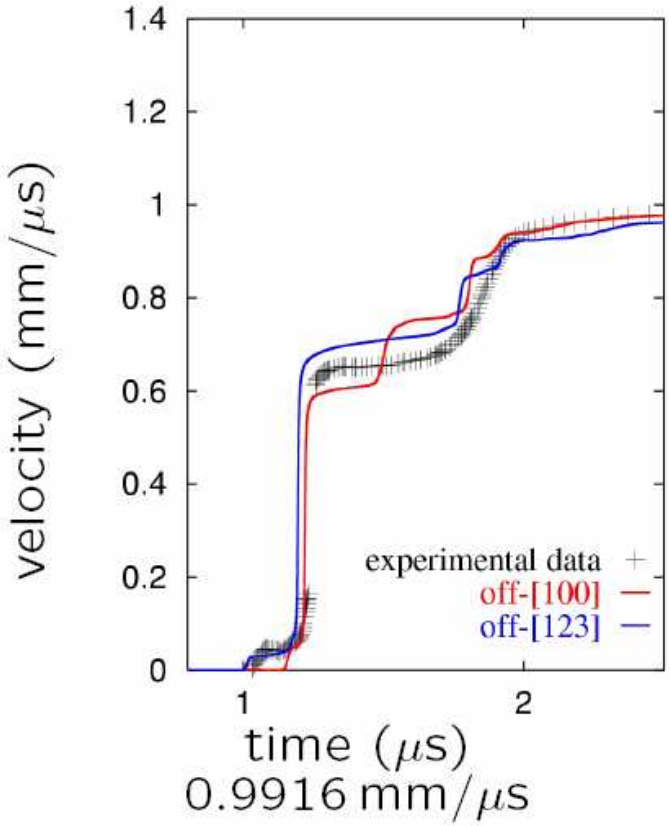

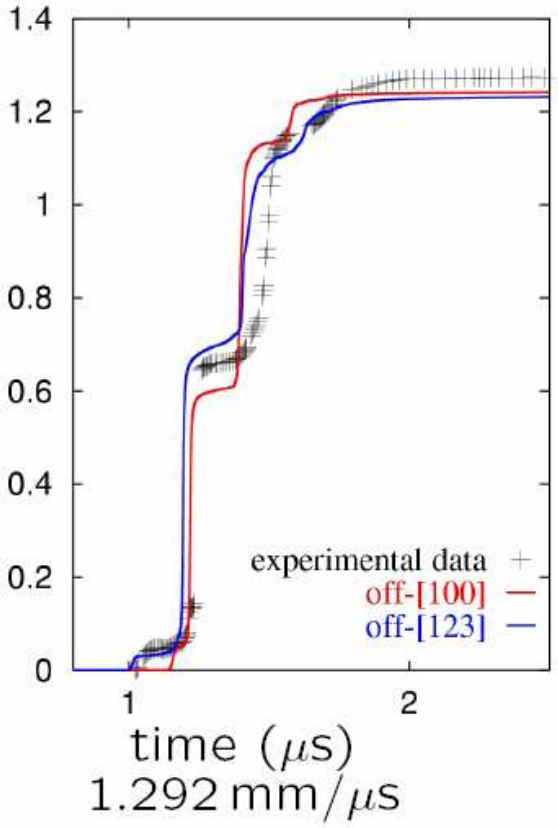

Single crystal responses bracket polycrystal response in some macroscopic observables

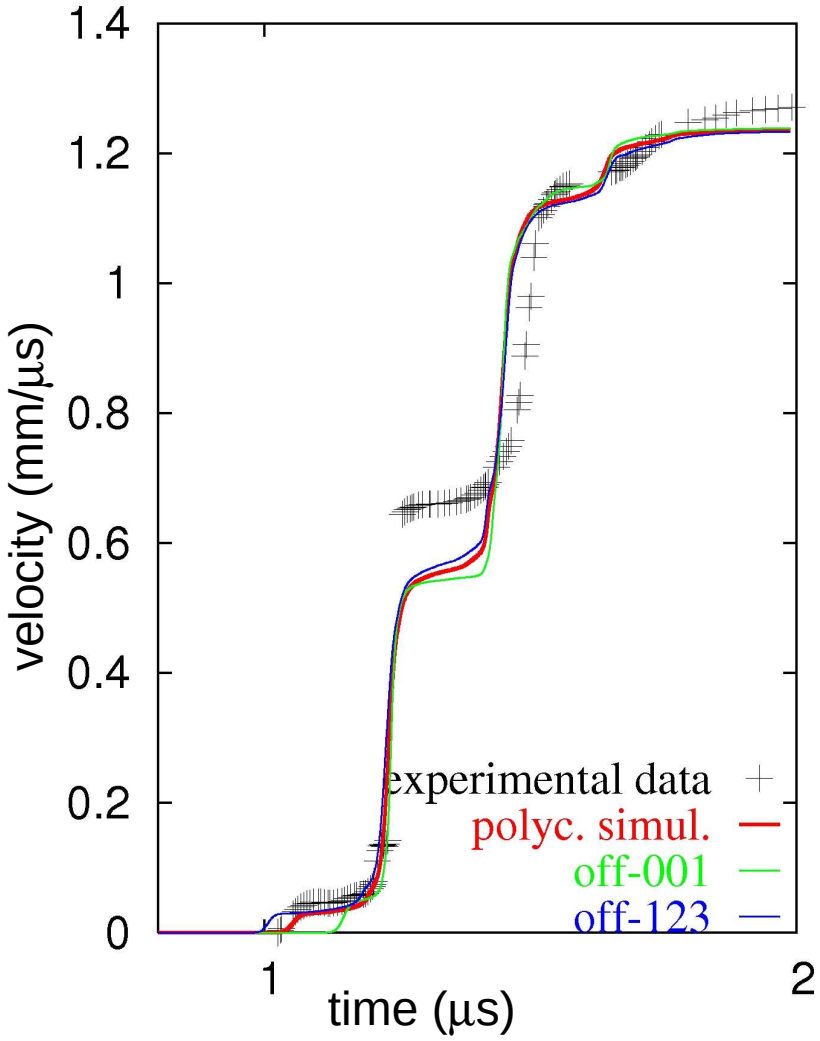

Polycrystal simulations show implications for macroscale kinetics

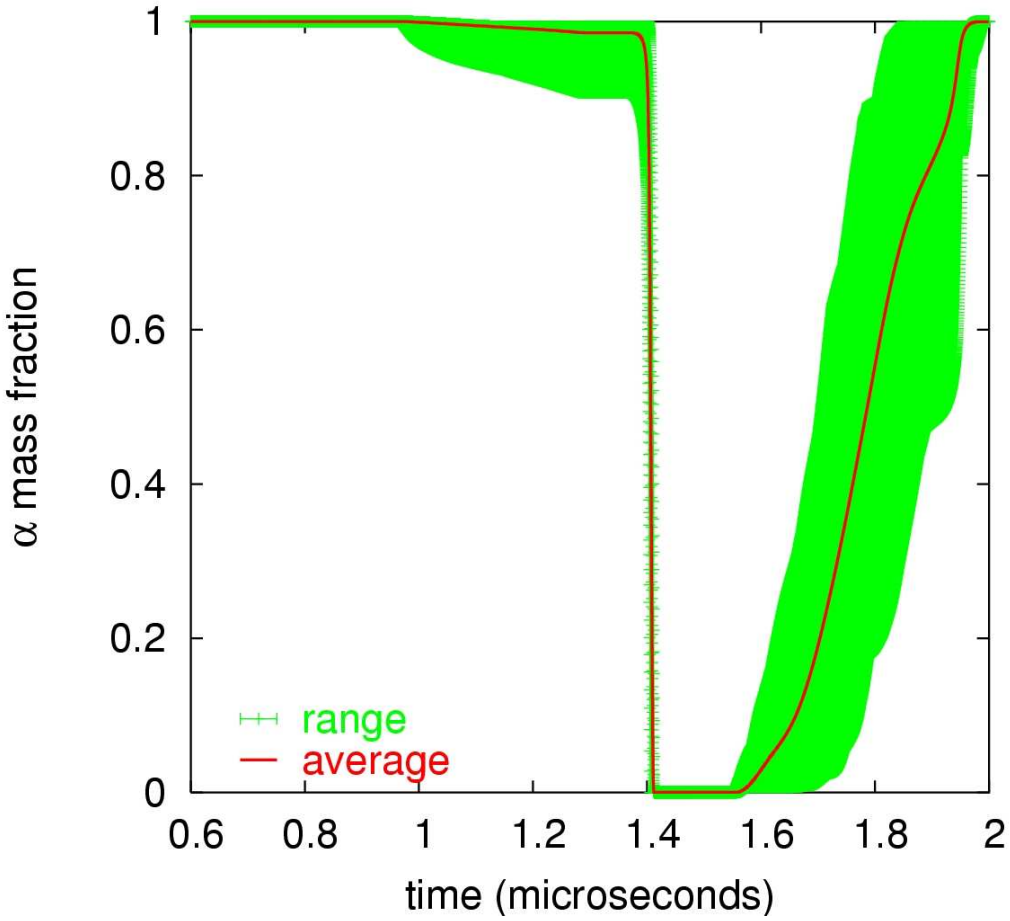

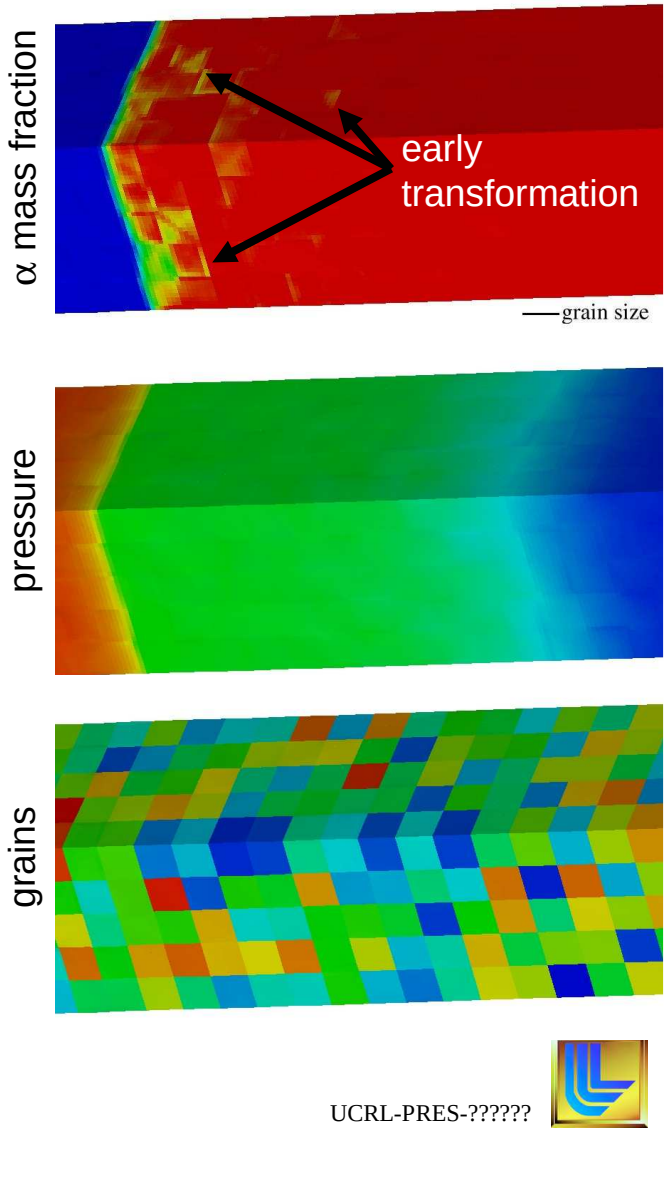

Variations over a cross section are due to averaging over a variety of smooth trajectories, not to noise

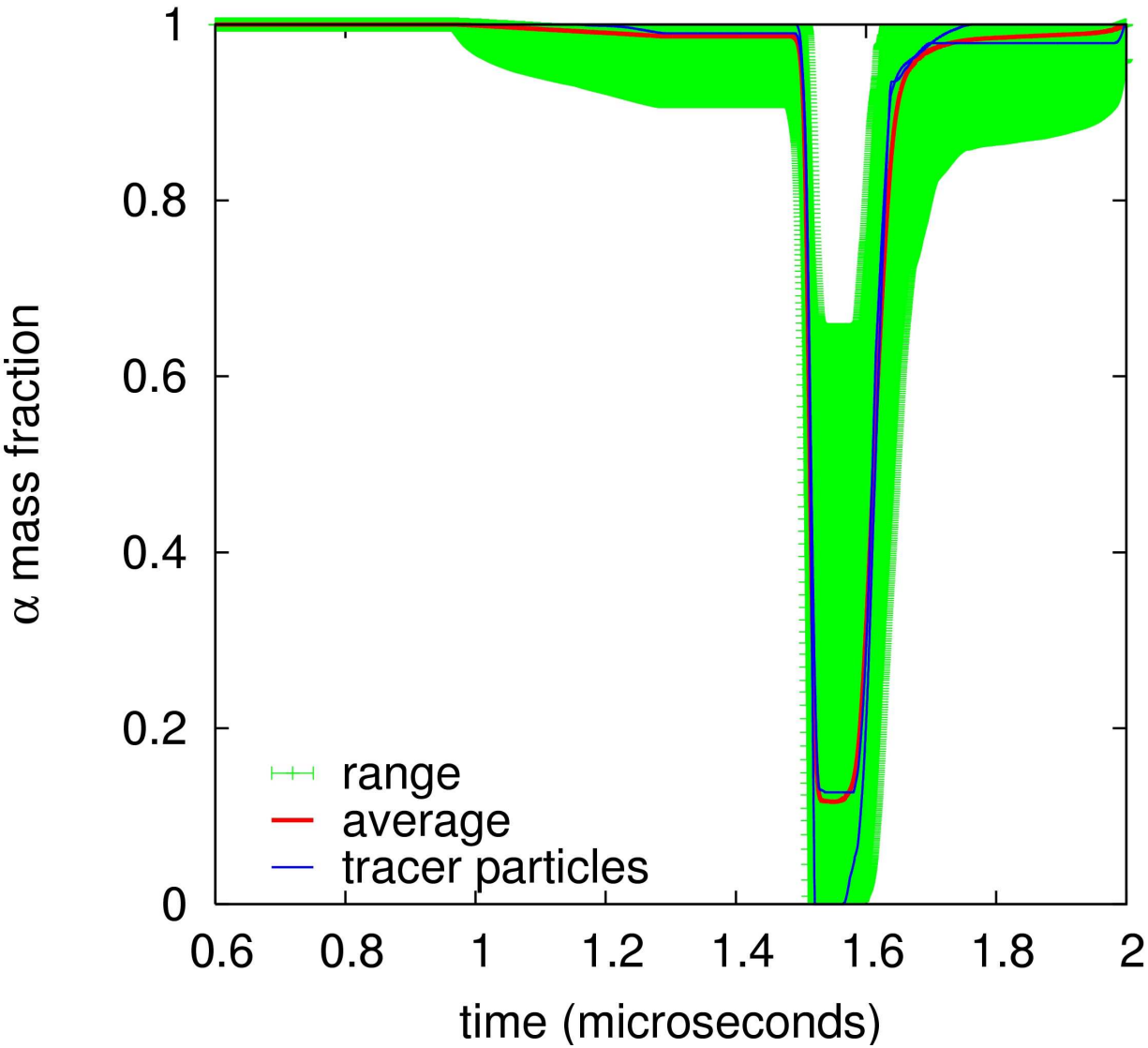

Interaction energy effects both macroscopic pressure and microstructure

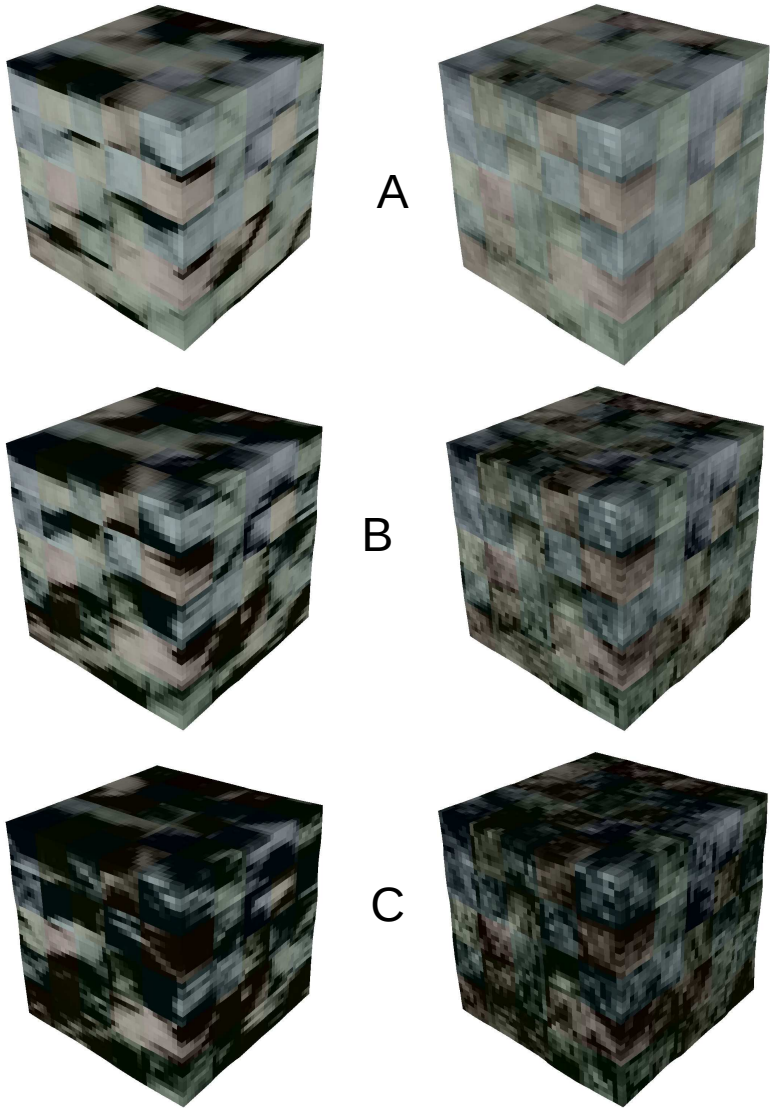

without interaction, $C^r = 0$ MPa

with interaction, $C^r = 200$ MPa

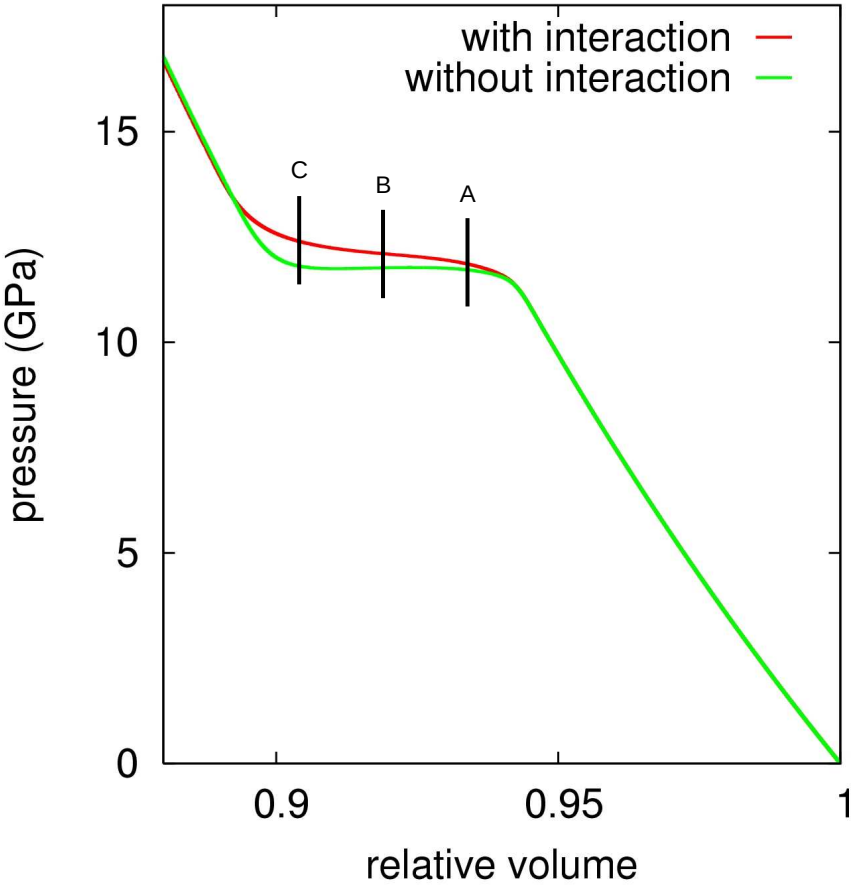

Variant selection is tied to material strength

Deviatoric stress selects phase variants

Stronger material:

- supports higher deviatoric stress
- wider range of driving forces for different variants

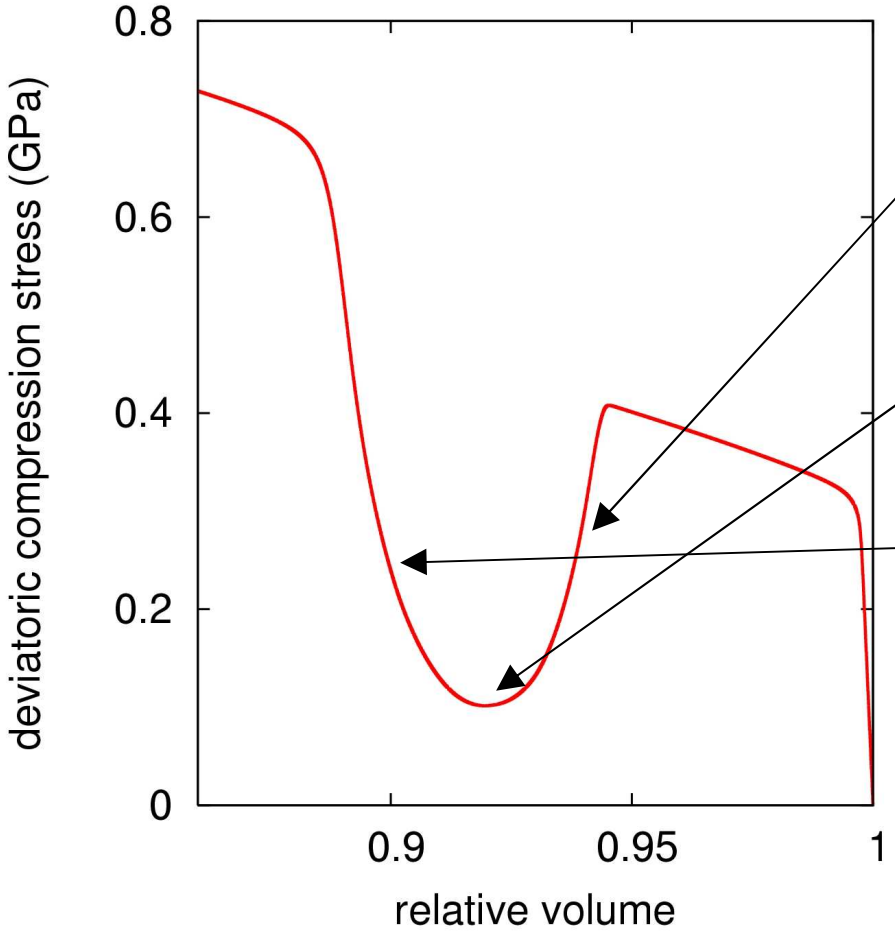

Deviatoric stress drops as material transforms to selected variants

Pressure remains high and continues to drive transformation

Deviatoric stress rises to drive plasticity in the produce phase

Conclusions

Successfully capture several experimentally observed phenomena

Formulation allows for use in high pressure and impact loading scenarios

Need more comparison to experimental results

Results for $\alpha \leftrightarrow \varepsilon$ in iron:

- needed simulation resolution depends on the observable of interest
- interaction energy model may influence post-transformation texture
- transformation mechanism remains unresolved

Possible extensions

- microstructurally motivated linking assumptions
- anisotropic thermal expansion

Strength Model Development for Irradiated Materials

A. Arsenlis

Lawrence Livermore National Laboratory

Collaborators: W.W .Wolfer, B.D. Wirth, M. Rhee, M. Tang, J. Vandersall, S. Schaldach, A.J. Schwartz (LLNL)

This work was performed under the auspices of the U.S. Department of Energy by the University of California, Lawrence Livermore National Laboratory under Contract No. W-7405-Eng-48.

Overview

- Motivation
  - Experimental Observations of Irradiated Polycrystals
  - Strength Estimates when Experiments are Unavailable
  - Multiscale Physics of Deformation
- Case 1: Model for Mechanical Behavior of Irradiated Cu
  - Continuum Model Development
    - Effective incorporation of lower length scale information
  - Comparison of Model Behavior with Experimental Observations
    - Including sample geometry effects
- Case 2: Model for Mechanical Behavior or Aged Pu-Ga alloys
  - Microstuctural Changes in Pu-Ga Alloys due to Self-Irradiation
  - Introduction of the MTS Class of Models
    - Modification of MTS model to include the effects of self irradiation
  - Model Predictions
- Conclusions

Experimental Observations of Irradiated Polycrystals - Copper

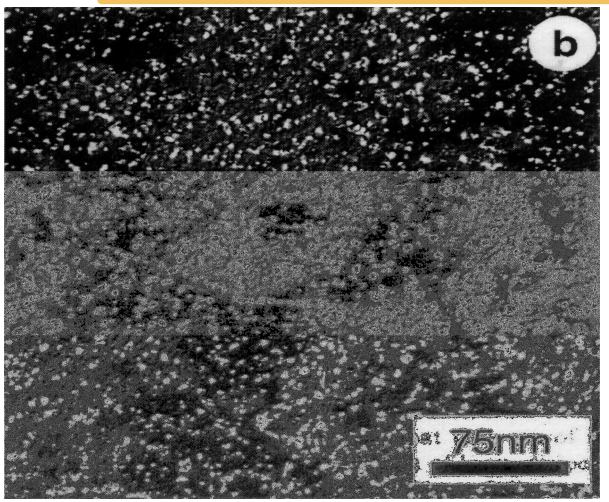

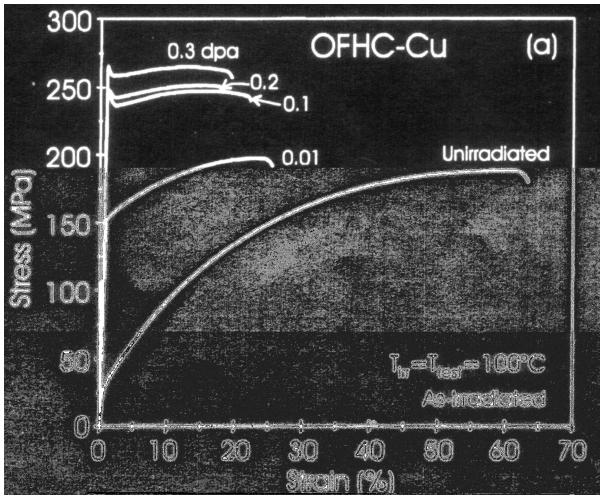

B. Singh et al., (2001), *J. Nucl. Mat.*, 299, 205

- Irradiated Microstructure Contains Nanometer-Sized Defects – Stacking Fault Tetrahedra, Prismatic Loops, Vacancy Clusters
- Defect Density Increases with Dose
- Increased Initial Yield Strength with Increasing Dose
- Decreasing Initial Strain Hardening with Increasing Dose
- Decreasing Strain to Failure with Increasing Dose
- Initial Strain Softening at Higher Doses
- Mechanical Characteristics are Common for a Wide Range of Irradiated Materials

Provide Estimates for Science Based Stockpile Stewardship

- Need to assess the safety and reliability of an aging nuclear stockpile within the context of science based stockpile stewardship
- Pu alloys self irradiate at a dose rate of 0.1dpa / year leading to a considerable total irradiation dose as the alloy “ages” over decades of time
- Need to estimate the mechanical behavior of theses alloys at “ages” that have not been reached and validate models with data from the accelerated aging program

Multiscale Physics of Deformation in Irradiated Polycrystals

- Irradiation-Induced Defect Size: $< 5 \times 10^{-9}$ m
- Irradiation-Induced Defect Spacing: $> 1 \times 10^{-8}$ m
- Initial Dislocation Spacing: $> 1 \times 10^{-6}$ m
- Final Dislocation Spacing: $< 1 \times 10^{-8}$ m
- Grain Size: $> 1 \times 10^{-5}$ m
- Tensile Test Specimen Geometry: $> 1 \times 10^{-2}$ m

- An Information-Passing Multi-Scale Materials Methodology Will Be Utilized to Develop a Coarse-Grained Constitutive Model Applicable at Macroscopic Length Scales

Case 1: MD Simulations of Copper Dislocation – SFT Interaction

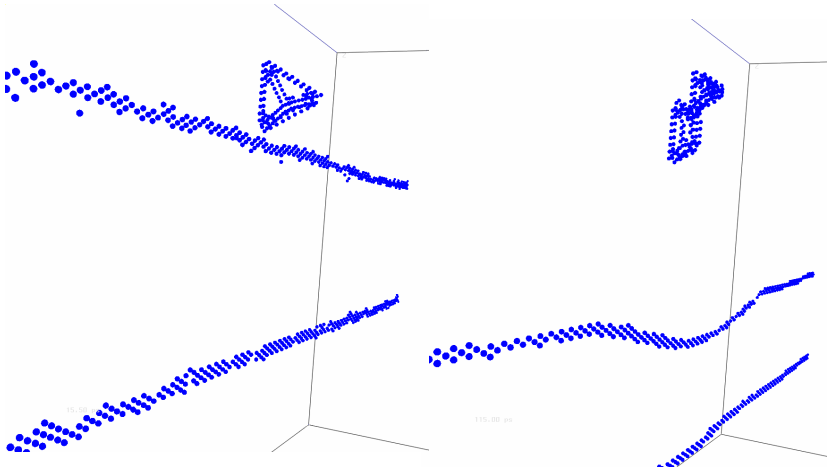

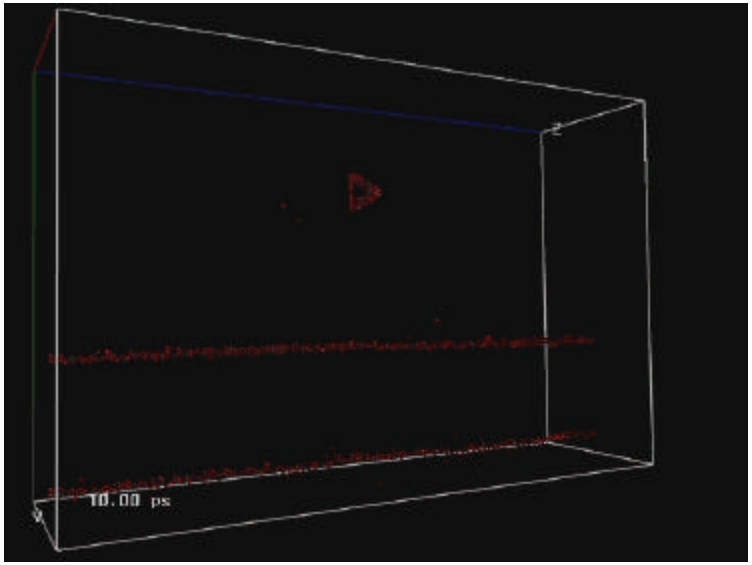

- Molecular Dynamics is used to capture irradiation induced defect evolution and the dislocation-irradiation induced defect interaction mechanisms

Defect Cutting with Plastic Deformation:

$$\frac{d\left(N_v d\right)}{dt} = N_v d\dot{\bar{e}}^{\mathrm{p}}$$

Conservation of vacancies:

$$\frac{d\left(N_v d^3\right)}{dt} = 0$$

Irradiation Induced Defect Strength:

$$b = \frac{1}{N_v d}\left(\frac{t}{mb}\right)^2$$

Dislocation Dynamics Simulations of Generic Microscale Behavior

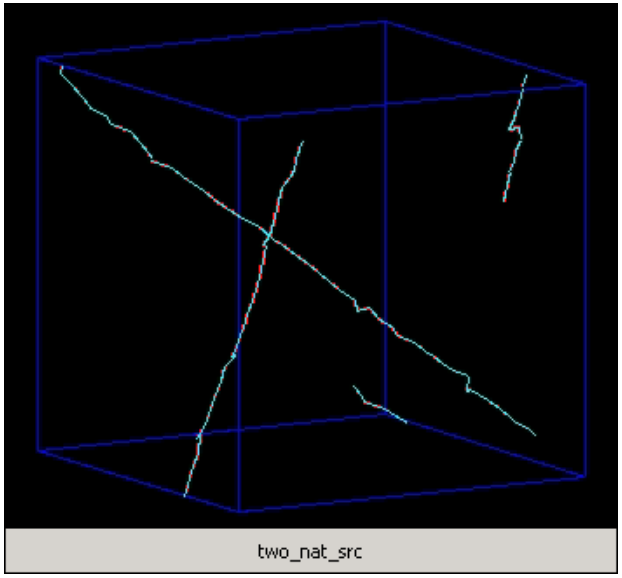

- Dislocation Dynamics is used to capture the dislocation density growth and dislocation-dislocation interaction mechanisms

Orowan's Relation for plastic flow:

$$\dot{\bar{e}}^{p} = r b \bar{v}$$

Dislocation Density Evolution:

$$\dot{r} = \left(\frac{2}{b\bar{l}} - r \frac{R_c}{2b} \right) \dot{\bar{e}}^{p}$$

Dislocation Segment Length Evolution:

$$\dot{\bar{l}} = \left(\frac{\bar{l}}{r} - d\bar{l}^{3} \right) \dot{r}$$

A. Arsenlis & M. Tang, (2003),
***Modelling Sim. Mat. Sci. Engrg*., 11**

Filling in the "Voids"

- MD and DD simulations do not provide all of the information needed for the macroscopic model so the system is closed with a limited set of assumptions
  - Material Isotropy

$$\bar{s} = \sqrt{\tfrac{3}{2}\left(\overline{\mathbf{T}} - \tfrac{1}{3}\mathrm{tr}\left(\overline{\mathbf{T}}\right)\mathbf{I}\right) : \left(\overline{\mathbf{T}} - \tfrac{1}{3}\mathrm{tr}\left(\overline{\mathbf{T}}\right)\mathbf{I}\right)}$$

  - Normality Flow Rule

$$\mathbf{L}^{\mathrm{p}} = \sqrt{\tfrac{3}{2}}\dot{\bar{e}}^{\mathrm{p}}\,\frac{\overline{\mathbf{T}} - \tfrac{1}{3}\mathrm{tr}\left(\overline{\mathbf{T}}\right)\mathbf{I}}{\bar{s}}$$

  - Size Dependence of Defect Resistance

$$b = 1 - \exp\left[-\left(\frac{d}{d_{ref}}\right)^{n}\right]$$

  - Dislocation Mobility Law

$$\bar{v} = v_o\left(\frac{\bar{s}}{mb\sqrt{ar + bN_v d}}\right)^{1/m}$$

Initial Conditions

- Physically Observable Initial Conditions Must be Set at the Outset
  - Initial Dislocation Density – Line Length/Volume

$$r = 1\times10^{12}\, m^{-2}$$

  - Initial Average Dislocation Segment Length – Length

$$\bar{l} = 1\times10^{-6}\, m$$

  - Initial Irradiation Induced Defect Density – Number/Volume

$$N_v = 1\times10^{23}\, m^{-3}$$

  - Initial Irradiation Induced Defect Size – Length

$$d = 2.5\times10^{-9}\, m$$

Single Material Point Behavior of Irradiated Copper

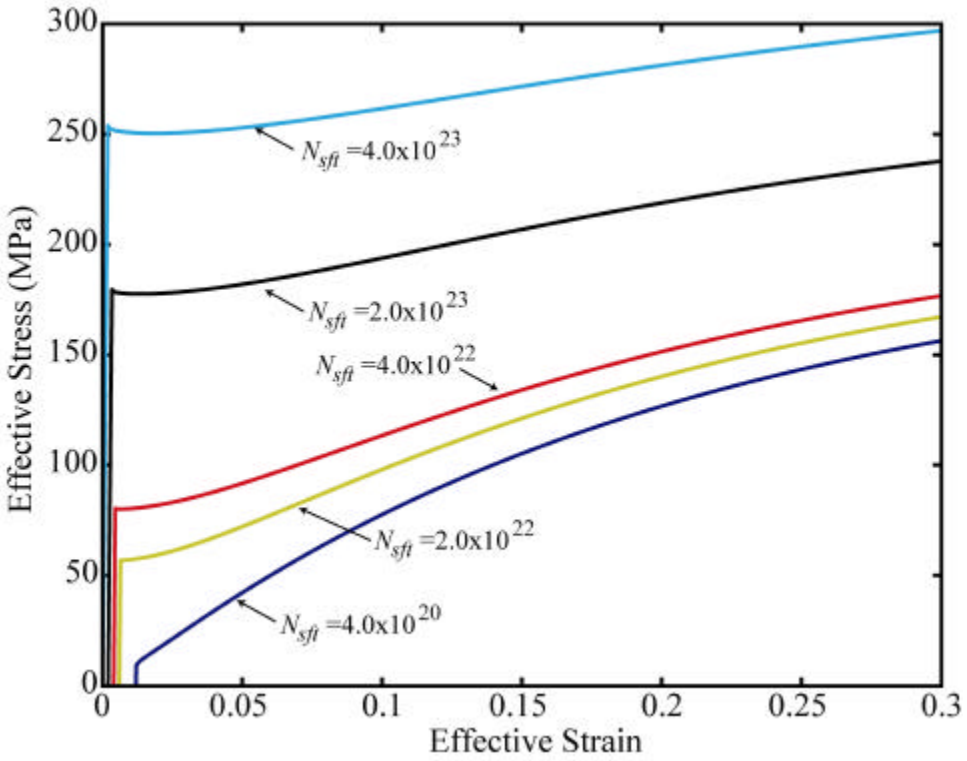

- The coarse grained macroscopic model is able to capture many of the features of the experimentally observed mechanical response

Yield Point Characteristics

$$s_y = mb\sqrt{ar + bN_v d}\left(\frac{\dot{\bar{e}}^p}{rbv_0}\right)^m$$

Hardening/Softening Characteristics

$$\frac{d\bar{s}}{d\bar{e}^p} = \left[\left(\frac{a}{2(a?_d + ßN_v d)} - \frac{m}{?_d}\right)\left(\frac{2}{bd_d} - ?_d\frac{R_c}{2b}\right) + \frac{N_v d}{2(a?_d + ßN_v d)}\left(ß + \frac{n}{2}(1-ß)\ln(1-ß)\right)\right]\bar{s}$$

Case 1: Full Tensile Specimen Simulation of Irradiated Copper

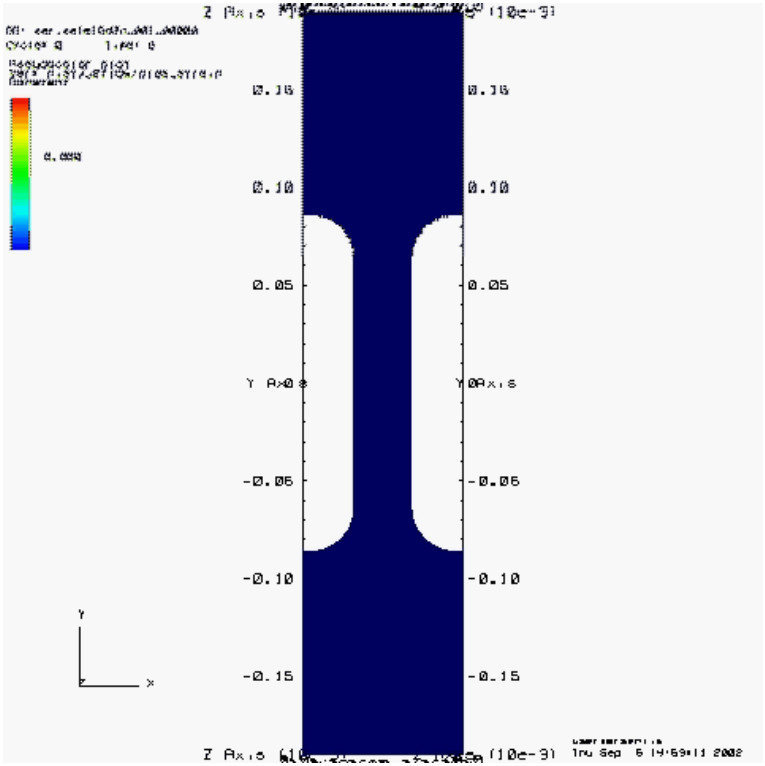

- Deformation behavior of highly irradiated materials is macroscopically heterogeneous
- Nominal Stress-Strain response of the model closely parallels the experimentally observed mechanical behavior for this test geometry

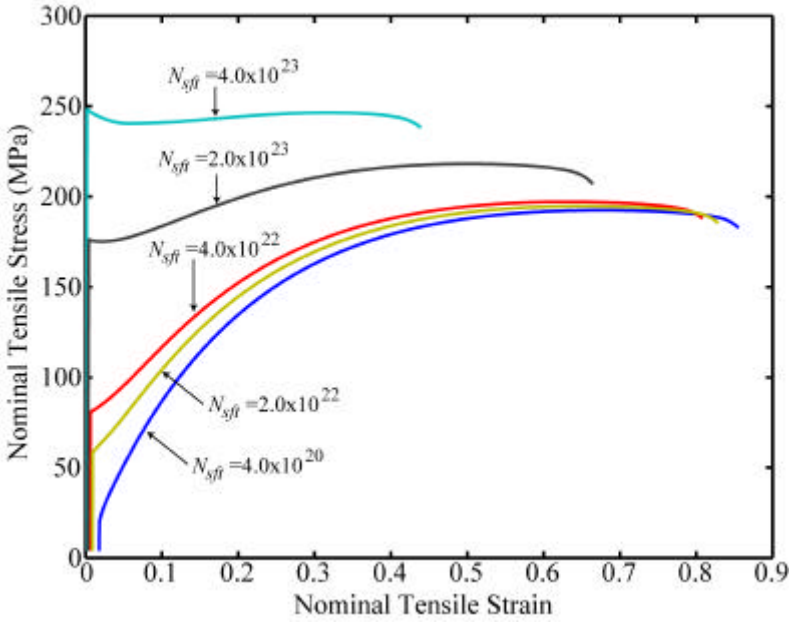

Predictive Model Development for Aged Pu-Ga Alloys: Microstructural Evolution

chemistry & materials science CMS

Kinetic rate model is developed to predict the helium bubble evolution as a function of material age and compared to known data (Schaldach & Wolfer)

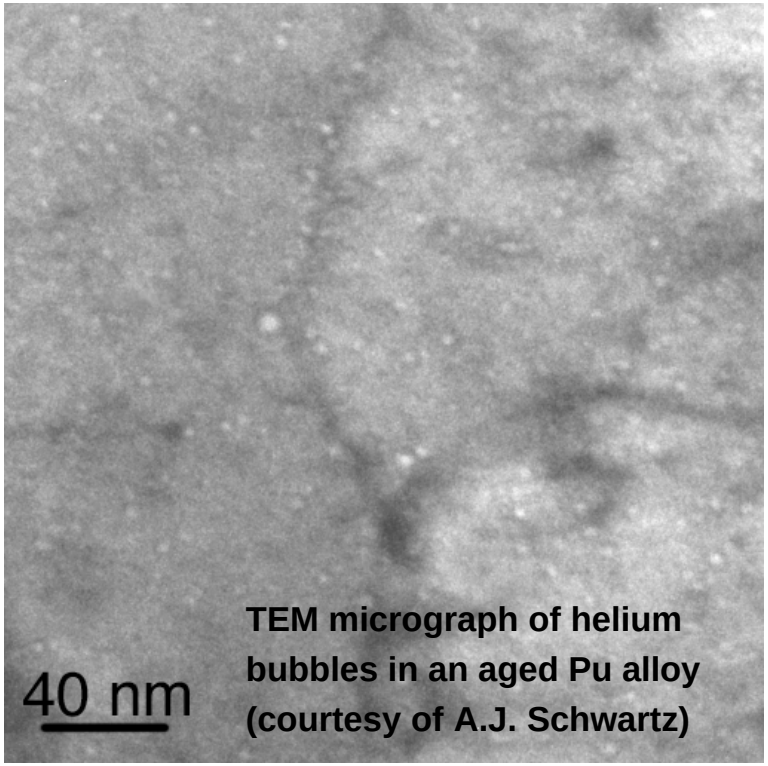

TEM micrograph of helium bubbles in an aged Pu alloy (courtesy of A.J. Schwartz)

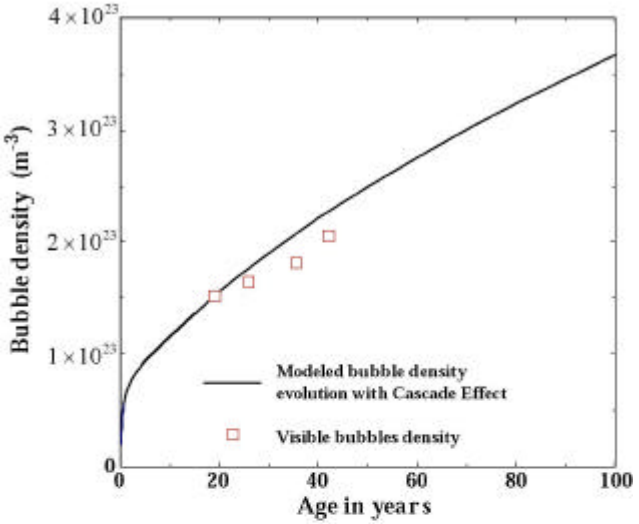

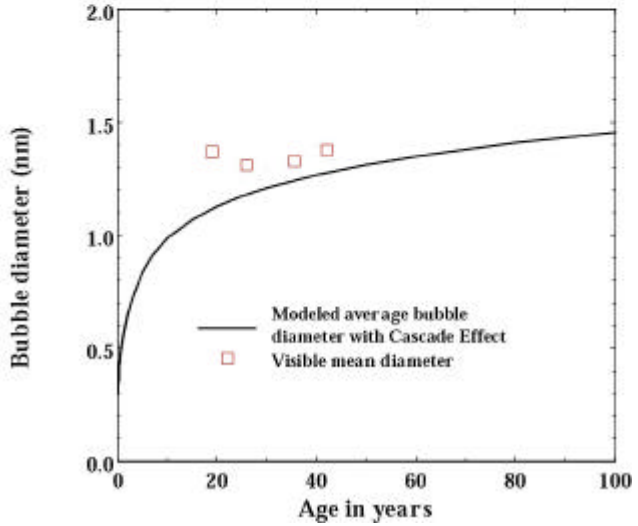

MD Simulations of Dislocation – He Bubble Interactions

chemistry & materials science CMS

2 nm He Bubble in Al

0.5 nm He Bubble in Al

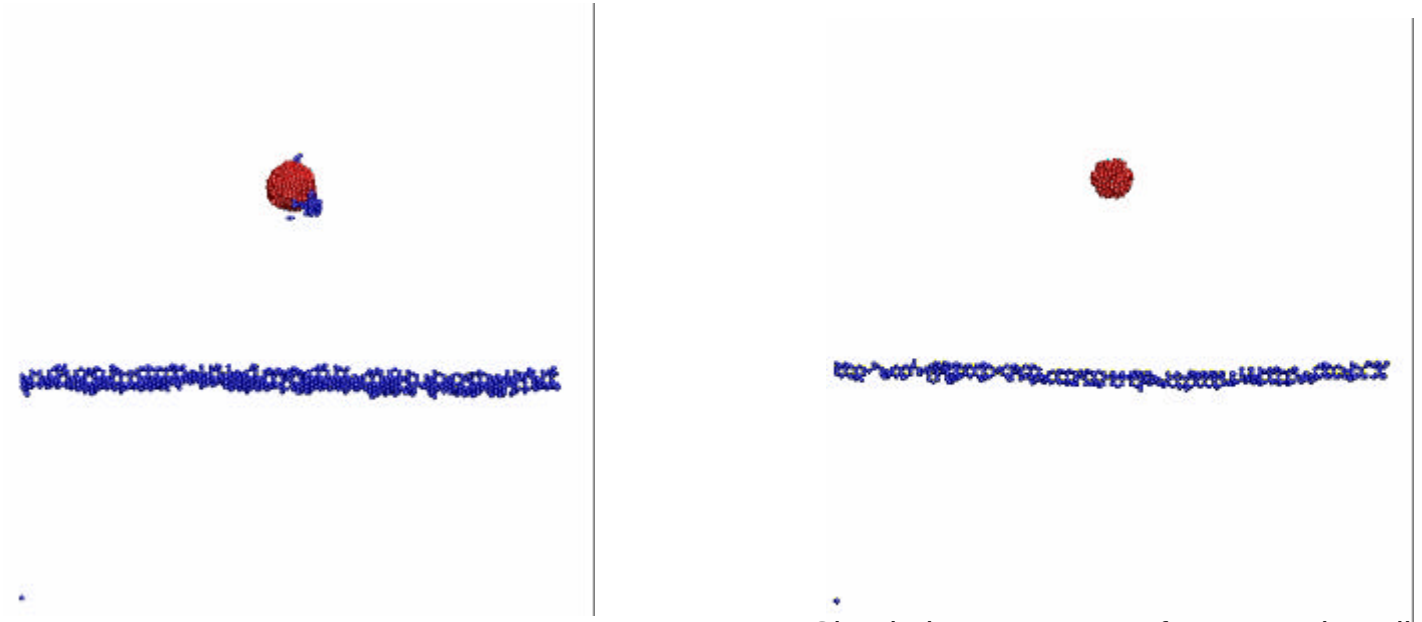

MD Simulations courtesy of J.A. Vandersall & B.D. Wirth

Barrier Strength of the He bubbles depend on bubble size

Bubbles may restructure their surface to remove step edges

Additional simulations show that the barrier strength is also strong function of He bubble pressure

Mechanical Threshold Strength (MTS) Model Basics

- Class of models first developed by U.F Kocks (LANL) and co-workers
- Plastic deformation occurs once the stress has surpassed a threshold strength
- The deformation rate is thermally activated at stresses above the threshold

- Plastic Strain Rate Constitutive Law

$$\dot{\bar{e}}^{\,p} = \dot{e}_0 \exp\left\{\frac{-\Delta F}{kT}\left[1-\left(\frac{\bar{s}-s_{ath}}{s_{th}}\right)^{p}\right]^{q}\right\}$$

For Simple FCC Metals

$$\dot{s}_{th} = f\left(s_{th}, T, \dot{\bar{e}}^{\,p}\right)$$

$$\dot{s}_{ath} = 0$$

For Simple BCC Metals

$$\dot{s}_{th} = 0$$

$$\dot{s}_{ath} = g\left(s_{ath}, T, \dot{\bar{e}}^{\,p}\right)$$

For Simple HCP Metals

$$\dot{s}_{th} = f\left(s_{th}, T, \dot{\bar{e}}^{\,p}\right)$$

$$\dot{s}_{ath} = g\left(s_{ath}, T, \dot{\bar{e}}^{\,p}\right)$$

- Pu-Ga alloys are FCC metals that behave like simple BCC metals in their strength characteristics

MTS Model Modifications for Capturing the Behavior of Irradiated Materials

- Replace the constant reference strain rate with a variable reference strain rate based on Orowan's relation

$$\dot{\bar{e}}^{\,p} = rbv_0 \exp\left\{\frac{-\Delta F}{kT}\left[1-\left(\frac{\bar{s}-s_{ath}}{s_{th}}\right)^{p}\right]^{q}\right\}$$

- Replace the hardening expressions with a strength-defect state relationship and defect evolution equations

$$s_{th} = 0$$

$$s_{ath} = g\left(r, N_b, d_b, P_b, N_{loop}, d_{loop}, T\right)$$

$$\dot{N}_b = \dot{d}_b = \dot{P}_b = \dot{N}_{loop} = \dot{d}_{loop} = 0$$

$$\dot{r} = \left(\frac{2}{b\bar{l}} - r\frac{R_c}{2b}\right)\dot{\bar{e}}^{\,p}$$

$$\dot{\bar{l}} = \left(\frac{\bar{l}}{r} - d\bar{l}^{\,3}\right)\dot{r}$$

- Match the unirradiated strain-hardening characteristics of the new model to the original MTS and extrapolate the behavior for aged alloy

Microstructural Strength Contributions

Total Strength is a cumulative quantity of many contributions

$$s_y = \sqrt{(s_d)^2 + (s_l)^2 + (s_b)^2} + s_P + s_m + s_{th}\left\{1 - \left[\frac{kT}{\Delta F}\ln\left(\frac{rbv_o}{\dot{\bar{e}}^p}\right)\right]^{1/q}\right\}^{1/p}$$

Dislocation forest resistance

Prismatic loop cutting resistance

Helium bubble cutting resistance

Helium bubble pressure misfit resistance

Helium bubble modulus misfit resistance

Strain rate and temperature dependence

The contributing strengths are either added linearly or in a root-mean-squared sense depending on their locality

Model Predictions of Aged Pu-Ga Alloys

Explore the effect of He bubble pressure on the aging characteristics of the alloy

Mechanical behavior is anticipated to have similar characteristics to other metals

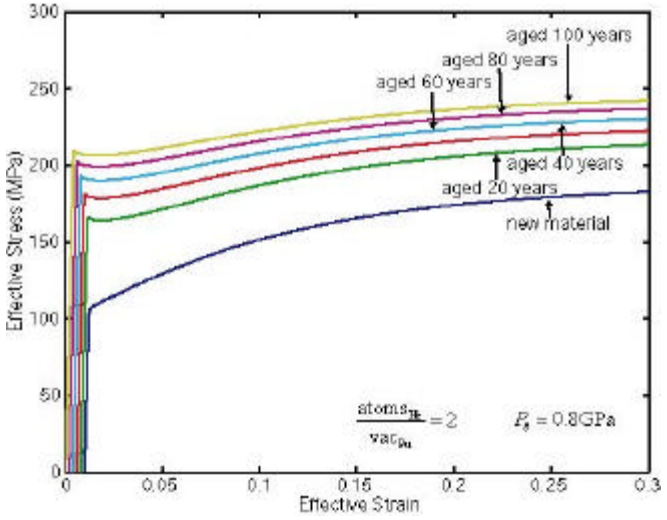

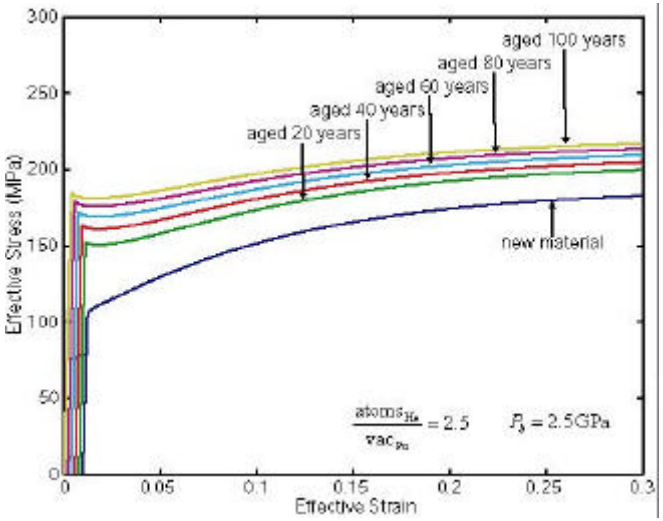

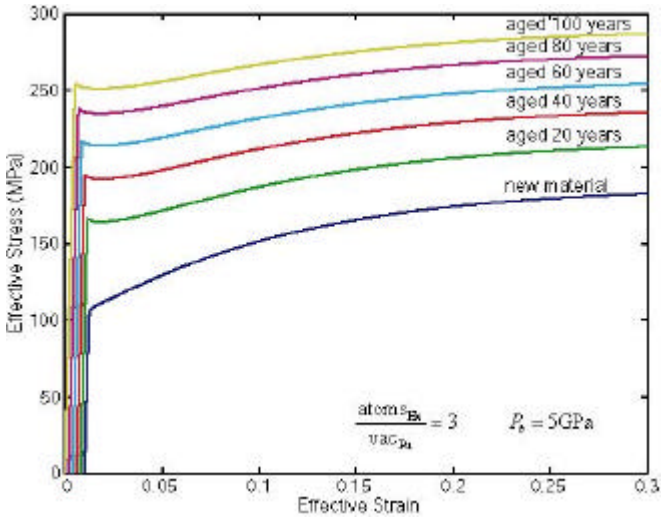

Conclusions

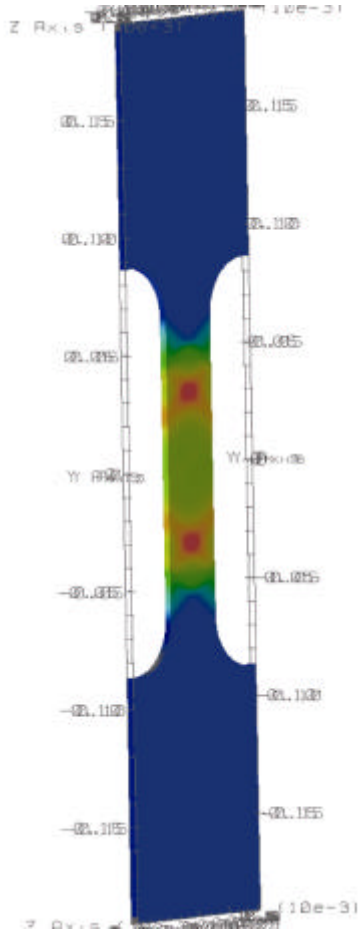

- Developed a coarse-grained macroscopic model for the irradiated metals
- Model development is inspired and informed from lower length scale simulations and experimental observations
- Model internal state variables are experimentally measurable quantities
- Simple model is able to reproduce the gross features of mechanical response of irradiated metals
- Developed a method for modifying MTS class of models to include the effects of irradiation damage
- Coupled a strength model with a kinetic rate theory of irradiation defect evolution to construct a complete process model